Stockholm University

Master Thesis

Degree Project in
Marine Geology, 60 hp

Evaluating VNIR–SWIR Hyperspectral Imaging Techniques for Mineral Identification in Arctic Marine Sediments

Mehdi Hosseini

Stockholm 2026

Department of Geological Sciences
Stockholm University
SE-106 91 Stockholm

With gratitude to Ahura Mazda, the Lord of Wisdom, for granting me the strength, the knowledge, and the insight to complete this work.
May Light forever prevail over Darkness.

Contents

Abstract

Mineral composition in Arctic marine sediments informs about past changes in sediment supply, ocean circulation and sea-ice dynamics. However, conventional mineralogical analyses are time-intensive, which limits the resolution of sedimentary reconstructions. This thesis evaluates visible–near-infrared and short-wave infrared (VNIR–SWIR) hyperspectral imaging (HSi) as a high-resolution tool for mineral identification in Arctic marine sediments. The study focuses on sediment core LRG07-PC04, recovered from the Greenland-side sector of the Lomonosov Ridge in the central Arctic Ocean, for which a high-resolution clay-mineral X-ray diffraction (XRD) dataset was available. VNIR–SWIR hyperspectral scanning was performed using the newly acquired GeoTek hyperspectral core scanner (HSi) at the Department of Geological Sciences at Stockholm University.

The aim of the thesis was to evaluate different approaches for predicting mineral composition from VNIR–SWIR hyperspectral data. This included testing a proprietary unmixing algorithm implemented in GeoTek's MINSPEC software, empirical single-band spectral proxies, diagnostic reflectance feature depths, partial least squares regression (PLSR) calibrated against clay-mineral abundances, and principal component and varimax-rotated principal component analyses (PCA/VPCA). These approaches were applied to the VNIR and SWIR hyperspectral data in their original reflectance form and after continuum removal (hull quotient), first-derivative and second-derivative processing.

The approaches differed markedly in their ability to predict mineral composition. Kaolinite was the most consistently identified mineral and was recovered reliably using empirical spectral proxies and PLSR, while PCA/VPCA also identified the spectral variability associated with kaolinite-rich intervals. Illite and chlorite were identified with moderate success, whereas none of the evaluated approaches provided a robust prediction of smectite. Empirical derivative-based proxies and PLSR generally performed better than the MINSPEC unmixing algorithm and the reflectance feature-depth approach, while PCA/VPCA provided an alternative, unsupervised route to the same mineral-related structure. Spectral proxies for carbonate and Fe also agreed well with XRF-derived geochemical trends, showing that HSi can provide continuous geochemical information alongside mineralogical estimates.

Overall, the results show that supervised calibration, and PLSR in particular, offers the clearest path to predicting mineral composition from VNIR–SWIR hyperspectral data when a reference dataset is available. Empirical spectral proxies remain useful mineralogical and geochemical indicators. The main limitation of this study is the narrow spread of clay-mineral abundances within the analyzed core. A priority for future work is therefore a broader Arctic training dataset with greater compositional variability, on which a more advanced supervised or machine-learning model could be built. The prediction results obtained here indicate that VNIR–SWIR HSi has clear potential to extend discrete mineralogical and geochemical measurements into continuous, high-resolution downcore records in Arctic marine sediments.

1. Introduction

Marine sediment cores from the Arctic Ocean record past changes in sea-ice and iceberg transport and in ocean circulation. Much of that information is carried by the mineralogical and geochemical composition of the sediment, which reflects both the geology of the source regions and the processes that erode, transport, sort and deposit the material (Wahsner et al., 1999; Viscosi-Shirley et al., 2003). Core LRG07-PC04, from the Greenland-side sector of the southern Lomonosov Ridge, is one such archive. Its position north of Greenland, between the Lincoln Sea, the Morris Jesup Rise and the Amundsen Basin, places it within a sediment-routing system with local influences from Greenland, as well as far field-transport from the Beaufort Gyre and Transpolar Drift (Jakobsson et al., 2008; Hanslik et al., 2013; Cronin et al., 2014).

Mineralogical composition is widely used to trace sediment provenance in Arctic Ocean sediments. Glacial marine sediments contain mixtures of fine terrigenous mud, coarser ice-rafted debris and biogenic components transported by sea ice, icebergs and currents. Carbonate, clay and Fe-bearing components are particularly informative. For example, dolomite and other carbonate detritus in Arctic sediments have been linked to carbonate-rich source areas in northern Canada and Greenland (Hanslik et al., 2013; Swärd et al., 2022). Clay-mineral assemblages are also widely used as provenance and transport indicators. The circum-Arctic compilation of Myers and Darby (2022) shows that illite is generally the most abundant and widespread clay mineral, with chlorite also broadly distributed, whereas smectite and kaolinite exhibit stronger regional gradients (Figure 1.1). However, because smectite and kaolinite occur on both the Eurasian and North American shelves, neither should be treated as a unique provenance indicator. Their distributions are therefore most informative when interpreted as part of a mineral assemblage and in combination with complementary tracers such as carbonate minerals and Fe-oxide fingerprints.

Conventional mineralogical analysis resolves these signals only at limited depth resolution. X-ray diffraction (XRD) gives robust clay-mineral identification but is destructive and is applied to discrete samples at centimeter to decimeter-scale spacing, so it can miss thin event layers and rapid compositional changes in slowly accumulating Arctic cores (Wahsner et al., 1999). X-ray fluorescence (XRF) core scanning provides continuous, non-destructive elemental records (Croudace et al., 2006; Croudace et al., 2019; Hanslik et al., 2013), but it measures elemental intensity rather than mineralogy, and converting intensities to quantitative composition itself requires careful calibration (Weltje and Tjallingii, 2008). There is therefore a need for rapid, non-destructive methods that generate continuous, high-resolution information on mineral composition.

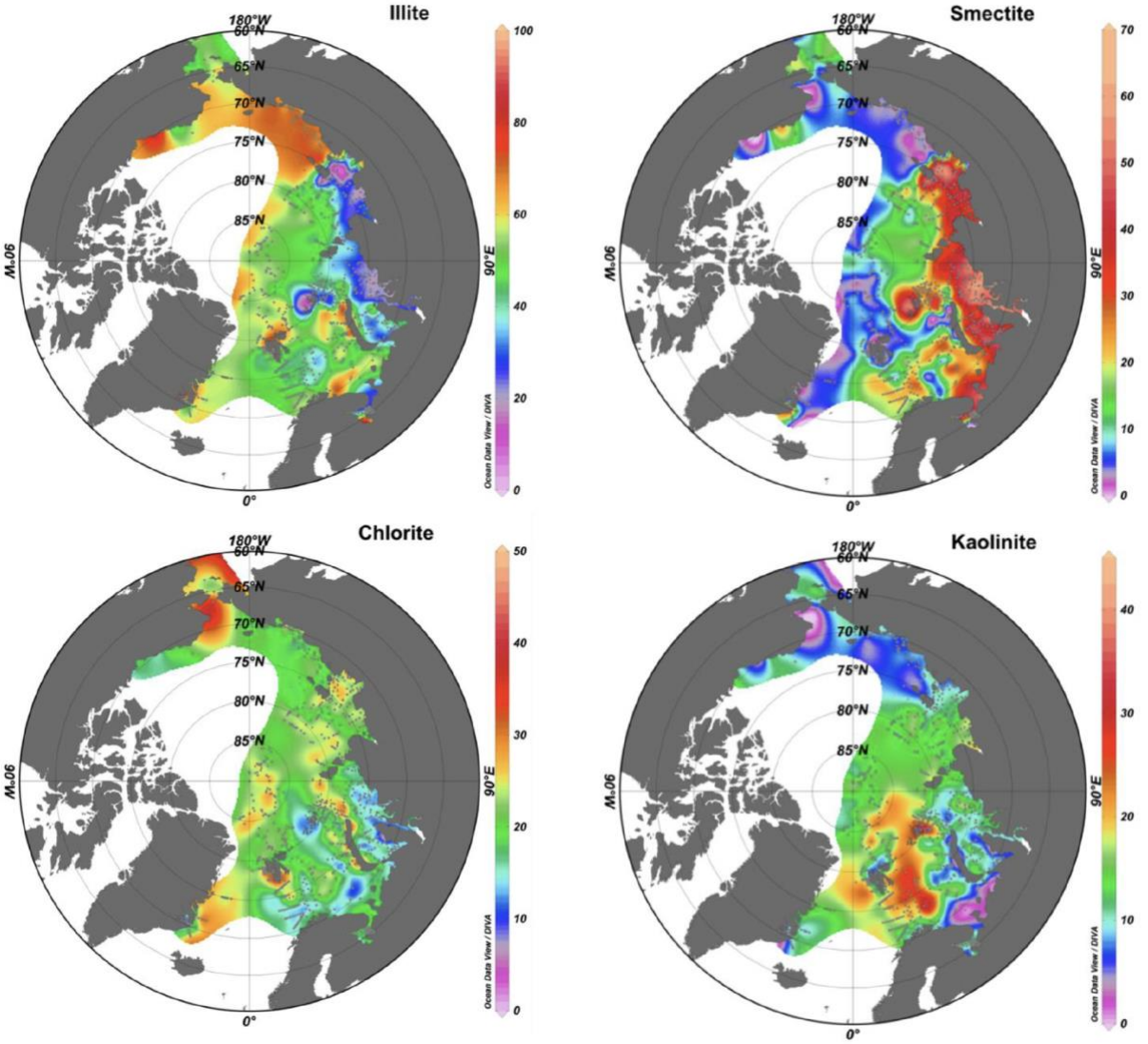

Figure 1.1. *Circum-Arctic distributions of the relative abundances (%) of the principal clay-mineral groups in the <45 µm fraction of coastal and shelf surface sediments: illite (upper left), smectite (upper right), chlorite (lower left) and kaolinite (lower right). The interpolated maps combine published circum-Arctic observations with additional data from the North American Arctic. Note that the colour-scale ranges differ among minerals. Adapted from Myers and Darby (2022).*

1.1 Hyperspectral imaging of marine sediments

Hyperspectral imaging records reflected light across many narrow, contiguous wavelength bands, typically spanning the visible, near-infrared and short-wave infrared regions (about 400–2500 nm). A hyperspectral core scanner acquires a spatially resolved reflectance spectrum at every pixel of a split-core surface, producing a three-dimensional cube with two spatial dimensions and one spectral dimension (Goetz et al., 1985; Zander et al., 2022). Minerals and sedimentary components can be distinguished because they absorb light at diagnostic wavelengths. In the VNIR, absorption is dominated by electronic transitions in Fe-bearing minerals and Fe^{3+} oxides or oxyhydroxides, whereas in the SWIR it arises from vibrational overtones and combination bands involving OH, H_2O and CO_3

groups, which makes the SWIR especially informative for clay minerals, hydrated phases and carbonates (Hunt, 1977; van der Meer et al., 2012) (Figure 1.2). By comparing measured spectra with reference libraries, diagnostic absorption features and independent laboratory data, HSi can map mineralogical variability continuously and non-destructively across the core surface (Jacq et al., 2022).

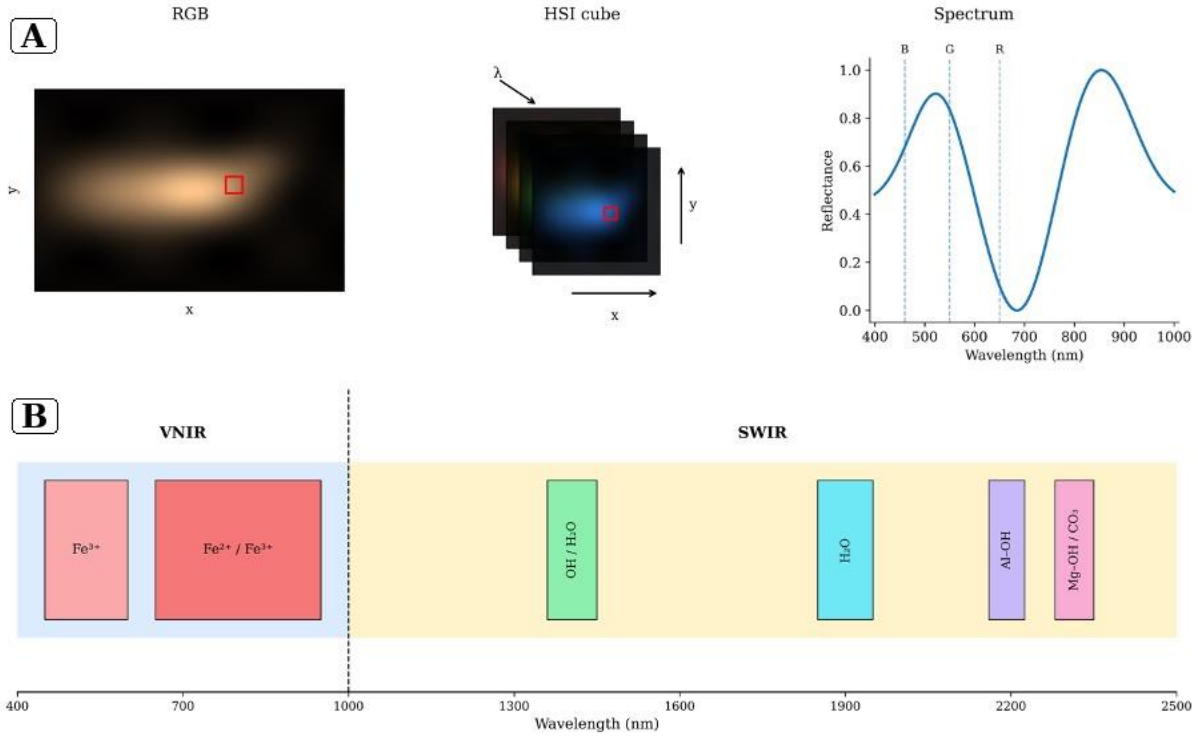

Figure 1.2. *Conceptual overview of hyperspectral imaging and the spectral regions used for mineral-sensitive analysis. (A) An RGB image contains three colour channels, whereas an HSI cube stores a full reflectance spectrum at each pixel. (B) Simplified VNIR–SWIR framework: VNIR wavelengths are mainly sensitive to electronic absorptions in Fe-bearing phases, whereas SWIR wavelengths contain vibrational absorptions associated with OH/H_2O, Al–OH, Mg–OH and CO_3-bearing groups.*

The choice of spectral range matters because different mineral groups are expressed with different diagnostic strength in the VNIR and SWIR (Table 1.1). Clay minerals and other phyllosilicates are generally poorly diagnostic in the VNIR but well expressed in the SWIR, whereas Fe-bearing oxides such as hematite are better expressed in the VNIR. Carbonates are only moderately expressed in the SWIR, but their diagnostic carbonate absorption features still fall within the wavelength range of the GeoTek scanner used in this study.

HSi has been used in the geosciences since the 1990s, but its applications are unevenly developed across settings. In remote sensing and hard-rock applications it is a mature scientific field. For example, hyperspectral drill-core logging is routinely used for mineral mapping, vein detection and alteration zonation in mining and petroleum exploration, where target minerals are abundant, crystalline and spectrally distinctive (Rodger et al., 2021; Jacq et al., 2022). Applied to sediment cores, HSi remains comparatively new. Recent reviews describe it as an emerging tool and document most applications using VNIR on lake sediments, where it has been used for pigments, organic matter, grain size and minerogenic components (Jacq et al., 2022; Zander et al., 2022). Methodological development in lake cores has been rapid, including inference of particle size by partial least squares, machine-learning and

deep-learning models (Ghanbari et al., 2020; Ghanbari and Antoniades, 2022; Kury et al., 2026) and tephra-layer detection by spectral clustering (Aymerich et al., 2016).

Applications of HSi on marine and lacustrine sediment cores faces two major challenges. First, fine-grained sediments are almost always a mixed mineral assemblage at the pixel scale, so a single spectrum superimposes the overlapping absorptions of several clay minerals, organic constituents, carbonate and Fe-bearing phases rather than isolating one endmember. Second, the split-core surface is wet, and water absorbs strongly in the same SWIR region used to identify clays and hydrated phases, which suppresses and distorts the diagnostic features. Because of these two effects, simple identification of specific absorption bands is rarely sufficient, and more sophisticated processing, including spectral unmixing, derivative treatment or supervised calibration, is generally needed to separate the mineral signal from the mixture and the water background.

Quantitative reflectance spectroscopy of marine sediment has a strong but geographically narrow precedent in carbonate- and opal-rich equatorial settings, where local ground-truth calibration of spectral features to mineral % ages works well for a small number of distinctive minerals, provided the cores are dry (Jarrard and Vanden Berg, 2006). In the Arctic, the most commonly applied spectral approach has been VNIR derivative reflectance combined with varimax-rotated principal component analysis (VPCA) to extract provenance-related modes, rather than direct clay-mineral calibration (Ortiz, 2011). To date, the potential of VNIR–SWIR HSi to predict clay-mineral and geochemical composition of Arctic marine sediments has not been investigated.

Domain	Structure	Mineral group	Example	VNIR (0.4–1.0 µm)	SWIR (1.0–2.5 µm)
Silicates	Inosilicates	Amphibole	Actinolite	Non-diagnostic	Good
	Inosilicates	Pyroxene	Diopside	Good	Moderate
	Cyclosilicates	Tourmaline	Elbaite	Non-diagnostic	Good
	Nesosilicates	Garnet	Grossular	Moderate	Non-diagnostic
	Nesosilicates	Olivine	Forsterite	Good	Non-diagnostic
	Sorosilicates	Epidote	Epidote	Non-diagnostic	Good
	Phyllosilicates	Mica	Muscovite	Non-diagnostic	Good
	Phyllosilicates	Chlorite	Clinochlore	Non-diagnostic	Good
	Phyllosilicates	Clay minerals	Illite	Non-diagnostic	Good
	Phyllosilicates	Clay minerals	Kaolinite	Non-diagnostic	Good
	Tectosilicates	Feldspar	Orthoclase	Non-diagnostic	Non-diagnostic
	Tectosilicates	Feldspar	Albite	Non-diagnostic	Non-diagnostic
	Tectosilicates	Silica	Quartz	Non-diagnostic	Non-diagnostic
Non-silicates	Carbonates	Calcite	Calcite	Non-diagnostic	Moderate
	Carbonates	Dolomite	Dolomite	Non-diagnostic	Moderate
	Hydroxides	Hydroxides	Gibbsite	Non-diagnostic	Good
	Sulphates	Alunite	Alunite	Moderate	Good
	Sulphates	Sulphates	Gypsum	Non-diagnostic	Good
	Borates	Borates	Borax	Non-diagnostic	Moderate
	Halides	Chlorides	Halite	Non-diagnostic	Uncertain
	Phosphates	Apatite	Apatite	Moderate	Non-diagnostic
	Hydrocarbons	Hydrocarbons	Bitumen	Uncertain	Moderate
	Oxides	Hematite	Hematite	Good	Non-diagnostic
	Oxides	Spinel	Chromite	Non-diagnostic	Non-diagnostic
	Sulphides	Sulphides	Pyrite	Non-diagnostic	Non-diagnostic

Good	Moderate	Non-diagnostic	Uncertain

Table 1.1. *Simplified VNIR–SWIR mineral-response summary for selected mineral groups relevant to reflectance mineralogy. Response classes indicate whether minerals are generally well characterised, moderately identifiable, non-diagnostic or uncertain in each spectral region. The table was modified from the TerraCore mineral-response summary reproduced by Mandende et al. (2023), with the LWIR column removed to focus on the VNIR–SWIR range used in this thesis.*

1.2 Hypothesis and research questions

The overall aim of this thesis is to evaluate approaches to predicting downcore mineral and geochemical composition using VNIR–SWIR hyperspectral core scanning of Arctic marine sediment core LRG07-PC04, benchmarked against XRD and XRF.

The central hypothesis is that spectral unmixing of VNIR–SWIR HSi can accurately predict downcore clay-mineral and geochemical variability in marine sediment cores. Testing this hypothesis is organised around three research questions:

1. What clay-mineral, carbonate/Ca and Fe-bearing targets can be recovered from VNIR-SWIR HSi data in marine sediments, and with what confidence?
2. Is there a single data reduction and analysis approach for the HSi data (i.e spectral unmixing, specific absorption band statistics, PLSR or PCA/VPCA) that consistently produces the best mineral and geochemical predictions? Or is the best approach target-dependent rather than universal?
3. What are the main challenges for developing HSi into a tool for mineral predictions in Arctic marine sediments?

2. Study area and sediment context

2.1 Core site and physiographic setting

Core LOMROG07-PC-004, here PC-04, was recovered on 24 August 2007 by the Swedish icebreaker Oden during the first Lomonosov Ridge off Greenland (LOMROG) expedition (Jakobsson et al., 2008). The site lies at 86.70117° N, 53.7672° W in 811 m water depth, on the southern Lomonosov Ridge between the Lincoln Sea, the Morris Jesup Rise and the Amundsen Basin (Figure 2.1).The Lomonosov Ridge is an elongated fragment of continental crust that separates the Amerasian and Eurasian basins. It was rifted from the Barents–Kara margin during the early Cenozoic opening of the Eurasian Basin and subsequently subsided as it moved toward the central Arctic (Cochran et al., 2006). The local bathymetry (Figure 2.2) shows that PC-04 was recovered from an elevated ridge setting adjacent to the deeper Amundsen Basin (Jakobsson et al., 2008). Sediments deposited on the ridge record open Arctic Ocean processes including sea-ice and iceberg transport, intermediate-water circulation and current-modified deposition.

This region o the Arctic records extensive Pleistocene marine glaciation. Repeated grounding of large ice masses extended into the central Arctic Ocean, leaving glaciogenic bedforms at water depths reaching about 1000 m, with the clearest imprint on the southern Lomonosov Ridge attributed to a marine ice-sheet or ice-shelf configuration during MIS 6 (Jakobsson et al., 2008; Jakobsson et al., 2010). The evidence does not support a single, uniformly thick ice

shelf grounding across all central Arctic highs, because several shallower highs lack comparable erosion, implying spatially variable grounding (Jakobsson et al., 2010).

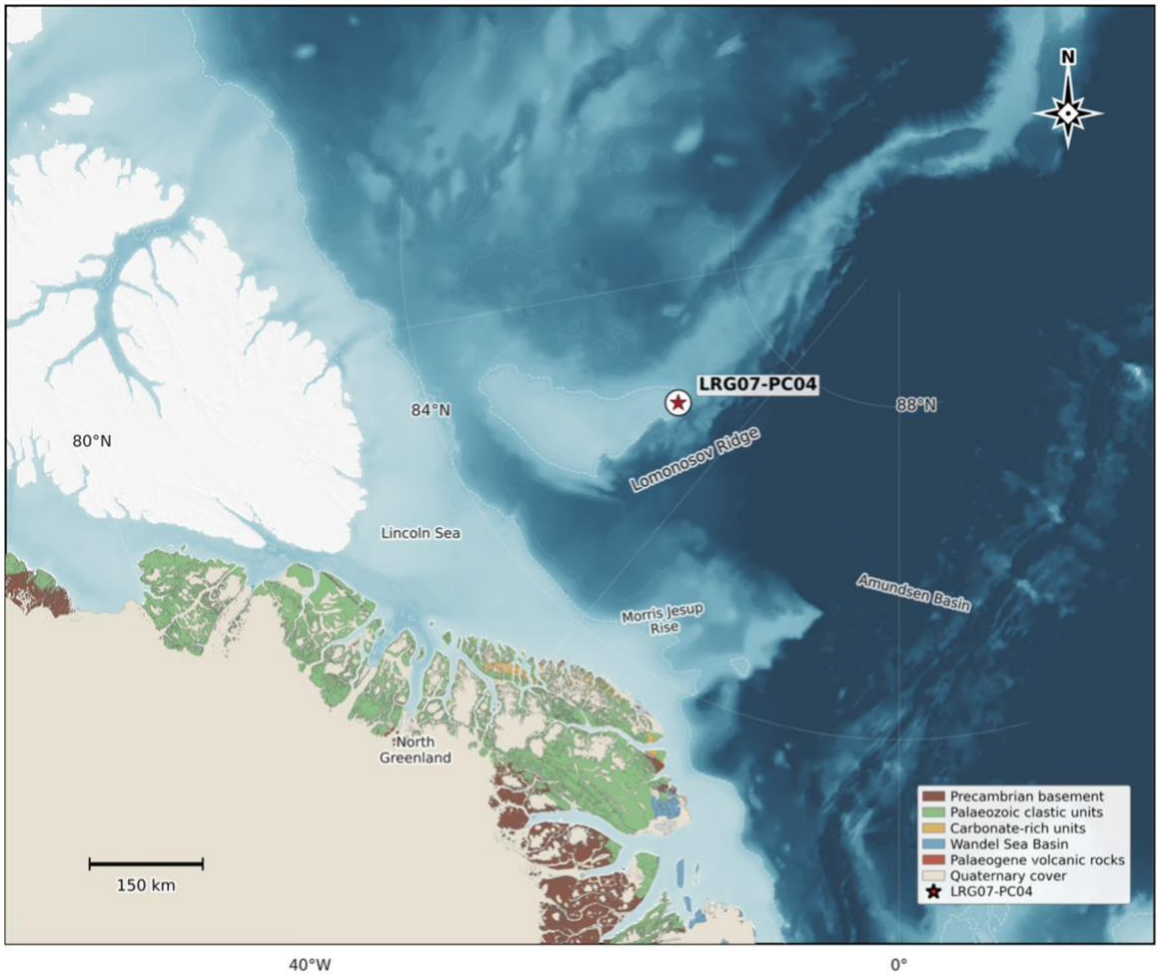

Figure 2.1. *Regional geological and bathymetric setting of core LRG07-PC04, showing its position on the southern Greenland-side sector of the Lomonosov Ridge relative to the Lincoln Sea, Morris Jesup Rise and Amundsen Basin. Exposed onshore geological units in northern Greenland are shown as regional source-area context, not as a complete provenance reconstruction.*

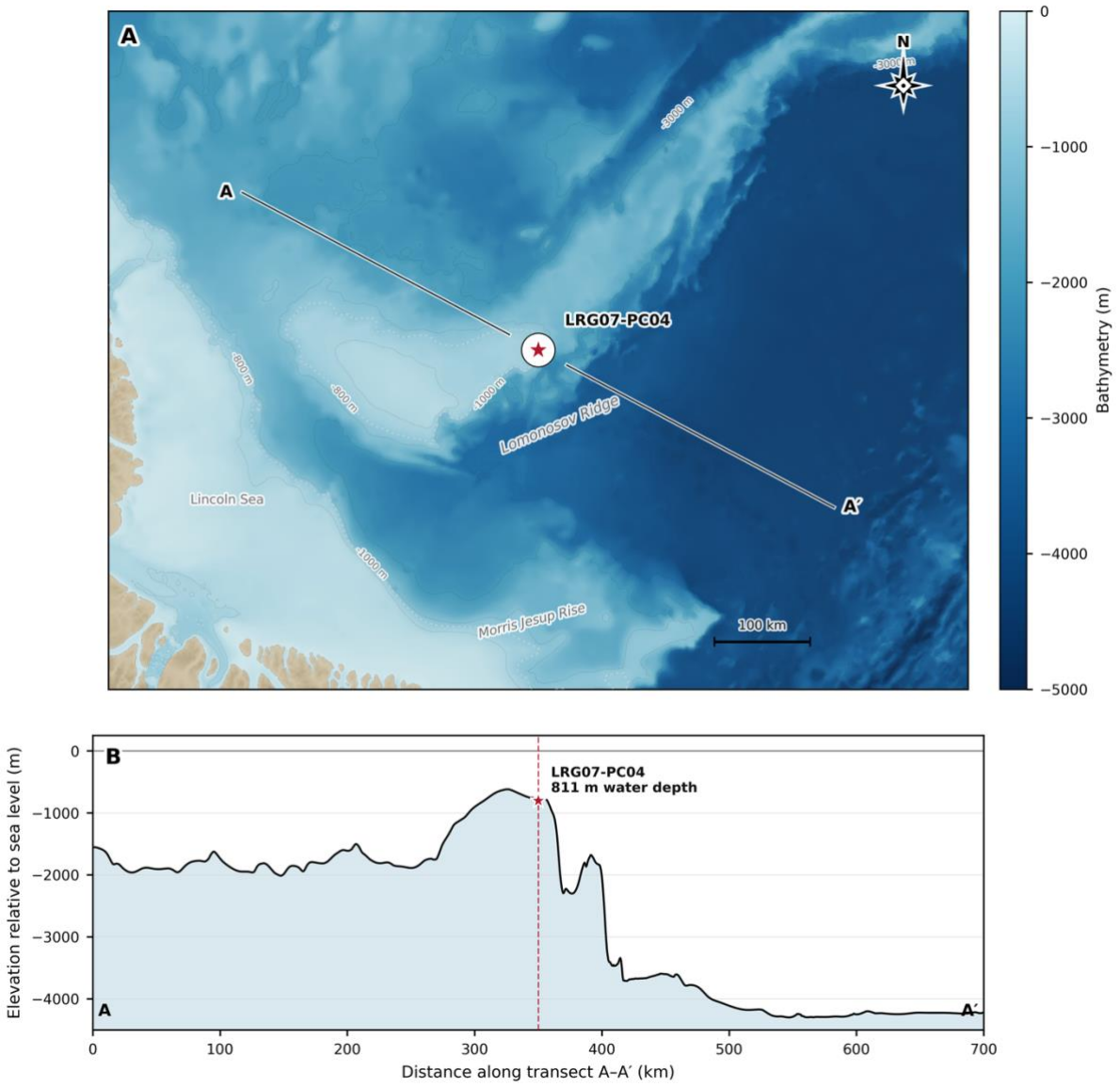

Figure 2.2. *Local bathymetric setting of core LRG07-PC04. (A) Bathymetric map of the southern Lomonosov Ridge showing the position of PC-04 and the A–A' transect. (B) Bathymetric profile along A–A', showing recovery at 811 m water depth from an elevated ridge setting adjacent to the deeper Amundsen Basin.*

2.2 Lithology and sediment provenance

Shipboard descriptions show that PC-04 is dominated by fine-grained marine sediment, mainly silty mud, but it is not lithologically uniform. Much of the sequence is slightly to strongly mottled, locally bioturbated silty mud, interrupted by sandy mud, sandy laminae, sand lenses, ice-rafted debris and isolated dropstones (Jakobsson et al., 2008). The coarser intervals indicate episodic iceberg or sea-ice rafting, glacially derived input or current-sorted sand superimposed on background fine-grained deposition (Polyak et al., 2009; Hanslik et al., 2013) (Figure 2.3).

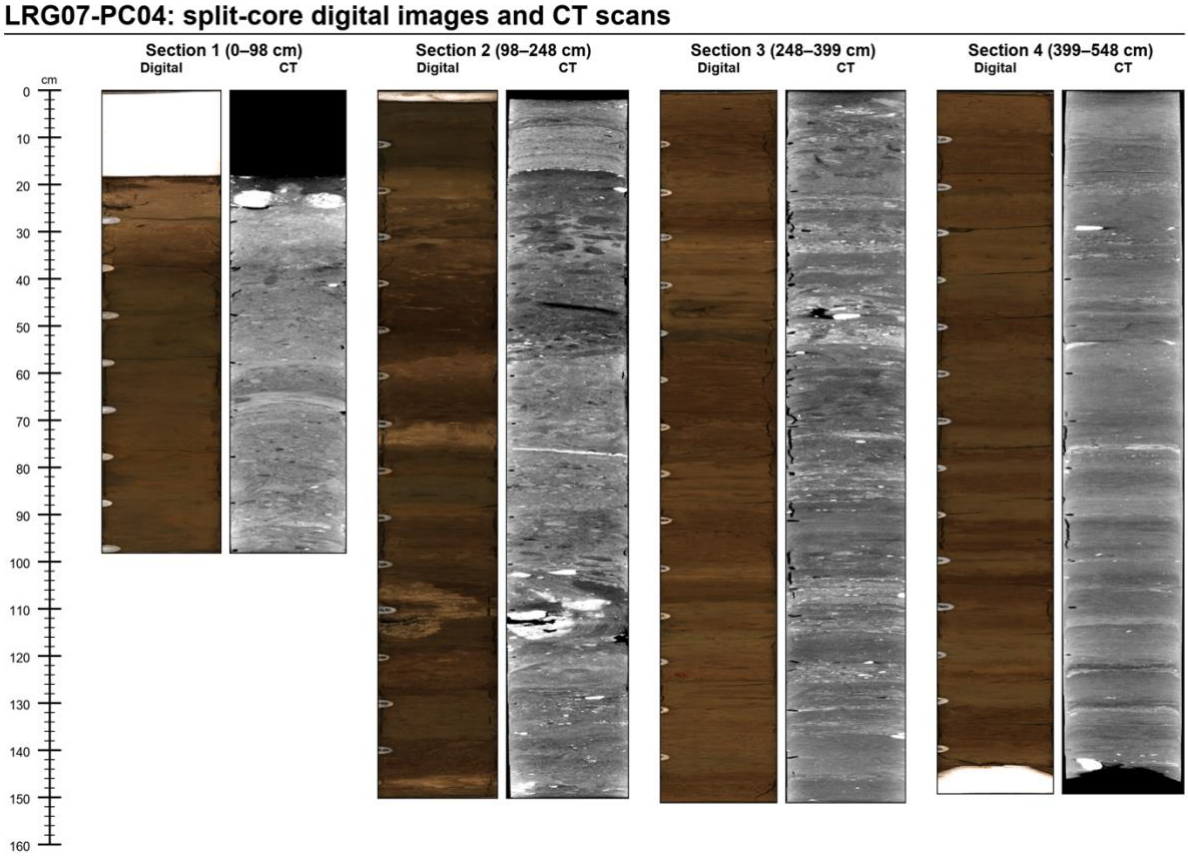

Figure 2.3. *Photo table of core LRG07-PC04 by section. For each of the four sections (0–98, 98–248, 248–399 and 399–548 cm), the split-core digital image is shown alongside the corresponding CT scan, illustrating downcore changes in colour, lithology, layering, bioturbation and coarse ice-rafted material. Section boundaries are at 98, 248 and 399 cm.*

Sediment provenance must be considered within both a regional and a basin-wide framework. The nearest exposed bedrock, in northern Greenland, is dominated by Palaeozoic successions of the Franklinian Basin, including carbonate-platform units and deeper-water siliciclastic deposits (Higgins et al., 1991; Henriksen and Higgins, 2008). Carbonate-platform successions are plausible sources of calcite- and dolomite-bearing detritus, whereas siliciclastic units may supply quartz, feldspar and the clay minerals illite and chlorite. Local bedrock cannot, however, account for all mineralogical signals. Hanslik et al. (2013) showed that carbonate-rich intervals in Greenland-side LOMROG cores include both biogenic and detrital components, with the strongest carbonate intervals reflecting detrital carbonate transported from Palaeozoic terrains in the Canadian Arctic. Such material is delivered across the Arctic Ocean by sea ice and icebergs, with pathways influenced by the Beaufort Gyre and Transpolar Drift (Bischof and Darby, 1997; Darby et al., 2002; Polyak et al., 2009). Because Ca resides partly in the silt and clay fraction, only part of the measured Ca intensity is attributable to carbonate microfossils (Hanslik et al., 2013), carbonate maxima in the core record a combined signal of foraminiferal abundance and detrital carbonate supply.

Clay minerals in Arctic marine sediments carry distinct provenance information (Myers and Darby, 2022).Smectite is derived predominantly from the weathering of basaltic rocks and volcanogenic material in the Kara–Laptev region, particularly the Putorana flood basalts, and is transported into the central Arctic by ocean currents and sea ice (Vogt and Knies, 2009). Illite and chlorite, the dominant

clay minerals in Arctic sediments, are supplied more broadly from the physical weathering of Palaeozoic sedimentary and metamorphic rocks around the Arctic margins. Both are abundant components of East Siberian and Chukchi Sea sediments (Swärd et al., 2018; Myers and Darby, 2022). Kaolinite is generally a minor but spatially variable component, with major sources including Franz Josef Land and Mesozoic sedimentary rocks of Alaska and the Canadian Arctic (Myers and Darby, 2022).

2.3 Oceanographic setting and carbonate-bearing intervals

The central Arctic Ocean is strongly stratified, with a cold, relatively fresh surface layer separated by a halocline from warmer Atlantic-derived water at intermediate depth (Aagaard and Carmack, 1989; Rudels et al., 2004). At 811 m, PC-04 lies within the lower Atlantic Layer, near the transition to Arctic Intermediate Water, so it is well placed to record indirect signals of changing Atlantic-water influence and upper-ocean conditions through microfossil abundance and carbonate preservation (Cronin et al., 2014; Vermassen et al., 2023). XRF-scanning Ca peaks in PC-04 commonly coincide with abundant planktic foraminifera, and the highest calcareous-microfossil abundances on the southern Lomonosov Ridge occur in these Ca-rich intervals (Hanslik et al., 2013). Because Ca is also a matrix mineral, from the weathering of carbonate terraines in Canada and Northern Greenland, only part of the measured Ca intensity is attributable to biogenic calcite (Hanslik et al., 2013).

3. Materials and methods

This chapter describes the core material and reference datasets, the GeoTek VNIR–SWIR hyperspectral acquisition and calibration, the spectral pre-treatment, the spectral-library and Mineral Analysis File (MAF) construction, and the procedures used to evaluate mineralogical and geochemical information from the HSi data.

The workflow (Fig. 3.1) first establishes the calibrated HSi products and the mineral-mapping framework, then evaluates HSi-derived variables against independent reference data through five processing routines: (i) MINSPEC library spectral unmixing; (ii) empirical single-wavelength proxy screening, including a local ±6-band robustness test; (iii) diagnostic absorption window feature-depth metrics; (iv) PLSR calibration of the XRD clay-mineral proportions, with a compositional-closure and residual-smectite check; and (v) unsupervised PCA/VPCA.

3.1 Study material and datasets

LRG07-PC04 comprises four sections (0–98, 98–248, 248–399 and 399–548 cm). The archived split-core surface was used for hyperspectral imaging. Independent reference and supporting datasets (XRD clay mineralogy, XRF, grain size, gamma density, CT and digital images) were used to evaluate and interpret the HSi-derived outputs.

The XRD dataset comprises 104 discrete samples between 19.0 and 542.5 cm and provides the clay-mineral reference data. It is an unpublished data set generated by colleagues at Tongji University. Kaolinite, illite, chlorite and smectite were re-calculated to sum to 100% at each analysed depth, so the values are relative proportions within the clay-mineral fraction rather than bulk-sediment % ages.

The XRF dataset comprises 1051 measurements between 17.5 and 543.5 cm at about 0.5 cm spacing, including Ca, Mn, Fe and Sr. Ca is used as an empirical indicator of Ca-bearing and carbonate-related variability, and Fe as an indicator of Fe-bearing or Fe-oxide response.

Additional datasets provided sedimentological and visual context. Grain-size data (262 samples, 18.5–544.0 cm; sand, silt and clay fractions) described sediment texture; MSCL physical-property data (524 measurements, 0.6–522.4 cm) provided bulk density; and digital images and CT scans supported sedimentological description.

3.2 Hyperspectral acquisition, reflectance calibration and data export

Data were acquired from the split surface of PC-04 using the GeoTek VNIR–SWIR hyperspectral core-scanning system at Stockholm University (Figure 3.2), which combines a motorised core tray, controlled illumination, RGB imaging and separate VNIR and SWIR push-broom cameras. The two cameras differ in their spatial and spectral sampling. The VNIR camera provides finer native cross-core spatial sampling than the SWIR camera, with a spectral sampling of approximately 2–3 nm per band. During export, the VNIR data were downsampled to match the SWIR pixel resolution, resulting in an effective cross-core pixel size of approximately 500 μm for both datasets. The principal sensor, acquisition and calibration specifications, including the spectral sampling and spatial resolution of each camera, are summarised in Table 3.1.

Before scanning, the split surface was cleaned, scraped and smoothed to reduce roughness, shadows, cracks and water films, and the calibration tile was set at the same height as the core surface so that calibration and sample measurements shared comparable geometry. Light and dark calibration were performed before scanning each section, and the calibration was checked against the factory Prime Tile profile as a quality control.

Raw detector measurements were converted to reflectance by the MINSPEC software using dark- and white-reference calibration, where dark calibration corrects for dark current and electronic offset and white-reference calibration normalizes the signal to the ceramic reference tile, following standard imaging-spectroscopy calibration practice (Clark and Roush, 1984). Reflectance was calculated for each wavelength as:

$$R_\lambda = \frac{I_s(\lambda) - I_d(\lambda)}{I_w(\lambda) - I_d(\lambda)} \cdot R_w(\lambda) \qquad (3.1)$$

where $R(\lambda)$ is the calibrated reflectance, $I_s(\lambda)$ the sample signal, $I_d(\lambda)$ the dark signal, $I_w(\lambda)$ the white-reference signal and $R_w(\lambda)$ the certified reflectance of the white standard; if the standard is treated as an ideal reflector, $R_w(\lambda)$ can be omitted and the expression becomes a relative reflectance correction.

Although the nominal VNIR and SWIR sensor ranges are about 400–1000 nm and 1300–2500 nm, the ranges retained after trimming noisy edge bands were about 450–950 nm (VNIR) and 1350–2450 nm (SWIR). The final exported datasets were line-averaged spectra along the depth axis, with about 204 VNIR and 300 SWIR bands, sampled at about 1 mm resolution over 0.05–547.95 cm.

Data inspection, spectral-library comparison and mineral-map generation were carried out in the GeoTek MINSPEC environment, and its outputs were compared with custom Python analyses developed for this project. MINSPEC stores data in ENVI-compatible format (binary image data with

an ASCII .hdr header describing data type, interleaving, dimensions, bands, sensor and wavelength metadata).

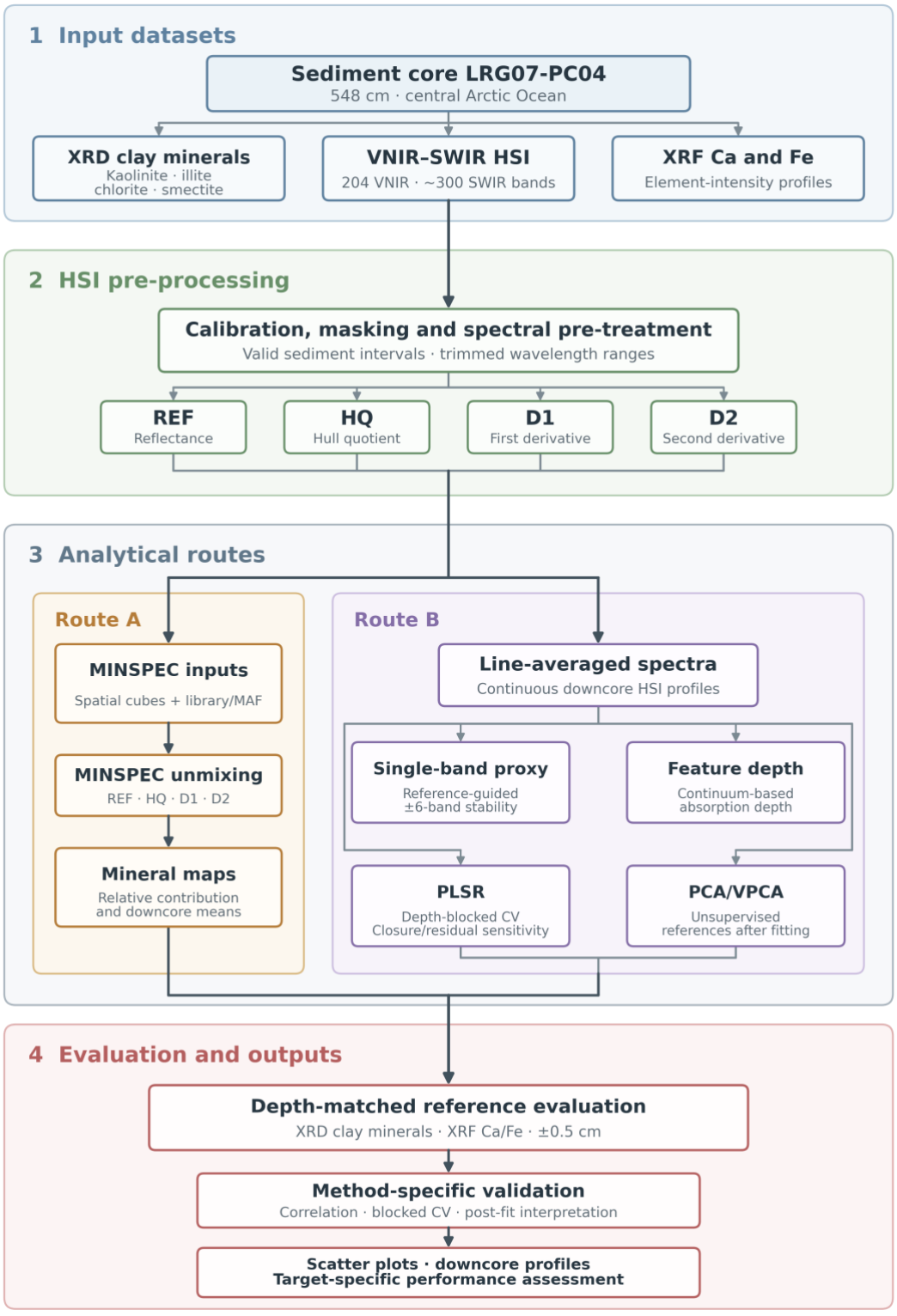

Figure 3.1. *Simplified HSI processing workflow for core LRG07-PC04, from split-core preparation, dark/white calibration and VNIR–SWIR scanning to the calibrated HSI cube and spectral pre-treatment. Pre-treated spectra feed two parallel routes: Route A uses the study-specific spectral library and customised MAF for MINSPEC unmixing and mineral maps; Route B extracts direct spectral proxies (single-band, local ±6-band, diagnostic-window and feature-depth variables). Outputs from both routes are evaluated against XRD and XRF before final products are selected for proxy interpretation, PLSR calibration and PCA/VPCA.*

Parameter	Specification
VNIR subsystem	Reflected-light range 0.4–1.0 µm; push-broom detector; 204 bands retained over the effective 450–950 nm range used for analysis.
VNIR spectral sampling	≈ 2–3 nm per band across the retained VNIR range.
VNIR pixel resolution	Higher native cross-core pixel resolution than the SWIR camera; downsampled on export to match the SWIR pixel resolution.
SWIR subsystem	SpecCam SWIR subsystem; reflected-light range 1.3–2.5 µm; 16-bit extended-wavelength InGaAs linear sensor; 145-pixel line scan with 50 µm pixel pitch.
SWIR spectral sampling	≈ 2 nm average bandwidth in the clay window; electronically tuneable configuration (1–300 channels), of which ~300 were retained over 1350–2450 nm.
SWIR pixel resolution	≈ 500 µm per pixel cross-core (145-pixel cross-core spatial line); the effective resolution of all exported products.
Calibration reference	Ceramic calibration tile positioned at the same height as the core surface so that calibration and sample measurements share comparable geometry.
Calibration procedure	Light and dark calibration before each new core image or when more than 10 min elapsed since the previous calibration; minimises illumination and camera-response drift.
Calibration QA/QC	Latest calibration checked against the factory-characterised Prime Tile profile; scope view used to check camera response, field of view and oversaturation before calibration.
Export / data format	MINSPEC ENVI-compatible format: binary image data with an ASCII. hdr header (data type, interleaving, dimensions, bands, sensor and wavelength metadata).
Effective analysis ranges	Trimmed to 450–950 nm (VNIR) and 1350–2450 nm (SWIR); these processed ranges are the datasets used in the analyses.

Table 3.1. *GeoTek VNIR–SWIR hyperspectral scanner configuration used for core LRG07-PC04, compiled from the GeoTek HSi Camera & Setup and MINSPEC documentation. Spectral sampling (nm per band) and pixel resolution are given explicitly for each camera. The VNIR camera has the higher native pixel resolution but was downsampled on export to the ~500 µm SWIR pixel resolution, so all products share that effective cross-core resolution. Nominal sensor ranges are reported separately from the effective exported ranges used after trimming noisy edge bands.*

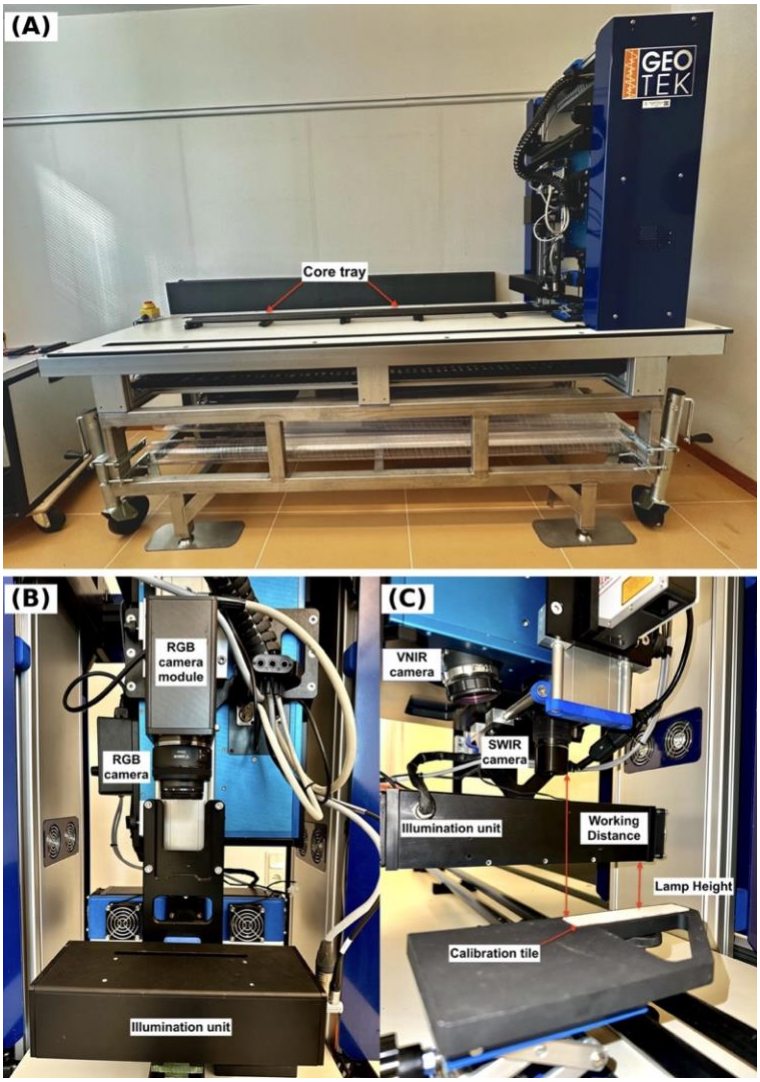

Figure 3.2. *Laboratory GeoTek hyperspectral core-scanning system and acquisition geometry at Stockholm University. (A) Scanner setup with the core tray on the scanning track. (B) RGB camera module and illumination unit. (C) VNIR and SWIR camera assembly, illumination unit, calibration tile, working distance and lamp-height configuration.*

3.3 Spectral-library design and MAF construction

GeoTek's proprietary processing software, MINSPEC, requires three basic inputs: the calibrated HSi cubes, a user-defined spectral library, and a customised Mineral Analysis File (MAF). The MAF is the file that tells MINSPEC which minerals to analyse for and over which wavelength range each should be assessed. Therefore, it links target minerals to the diagnostic wavelength intervals used during unmixing. The spectral library was selected from the USGS Spectral Library Version 7 (Kokaly et al., 2017), guided by the XRD results and the expected Arctic marine sediment mineralogy. Because the USGS library contains multiple spectra for any given mineral, a subset of entries was retained for each mineral based on visual agreement between candidate reference spectra. This reduction limited spectral ambiguity, reduced redundancy among similar endmembers and excluded geologically implausible minerals. The final library is listed in Appendix Table A.1.

The MAF covered kaolinite, illite, smectite, chlorite, calcite, dolomite, goethite and hematite. Initial intervals were defined from established mineral absorption regions and reference-library spectra, then

refined by visual inspection of endmember spectra in the reflectance, hull-quotient, first-derivative and second-derivative domains to identify diagnostic absorption regions (Figures 3.3 and 3.4). The mineral-specific windows are summarised in Table 3.2. The complete MAF file used in this study is provided in Appendix Figure A.1.

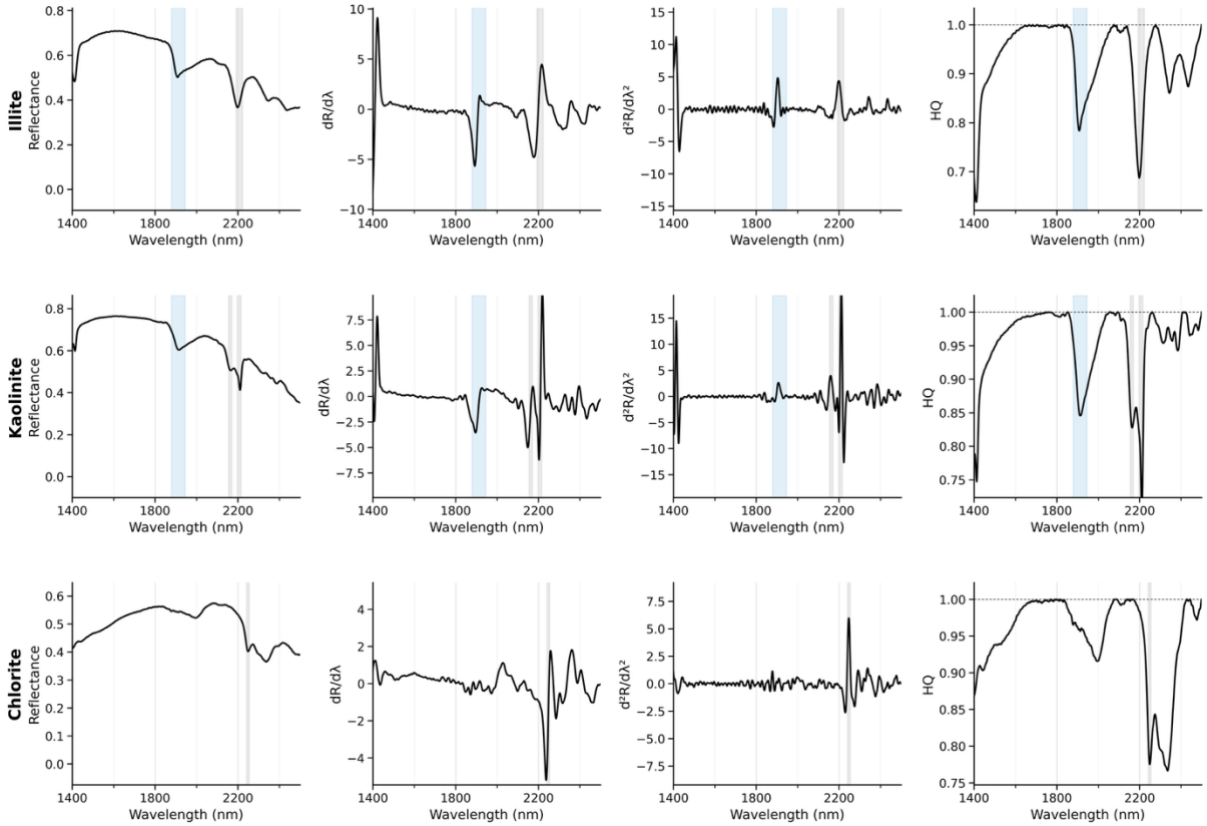

Figure 3.3. *Reference spectra of illite, kaolinite and chlorite used to guide wavelength-window selection for spectral-library and MAF construction, shown as reflectance (REF), first derivative (D1), second derivative (D2) and hull quotient (HQ). Blue shading indicates the broad approximately 1900 nm H_2O/OH hydration-sensitive absorption region, where applicable, whereas grey shading marks the selected SWIR Al–OH and Mg–OH clay-sensitive regions. These regions were guided by established VNIR–SWIR mineral-absorption behaviour and refined through visual inspection of the selected USGS Version 7 reference spectra (Hunt, 1977; van der Meer et al., 2012; Kokaly et al., 2017). The shaded intervals represent workflow-specific configuration windows rather than unique mineral-identification criteria.*

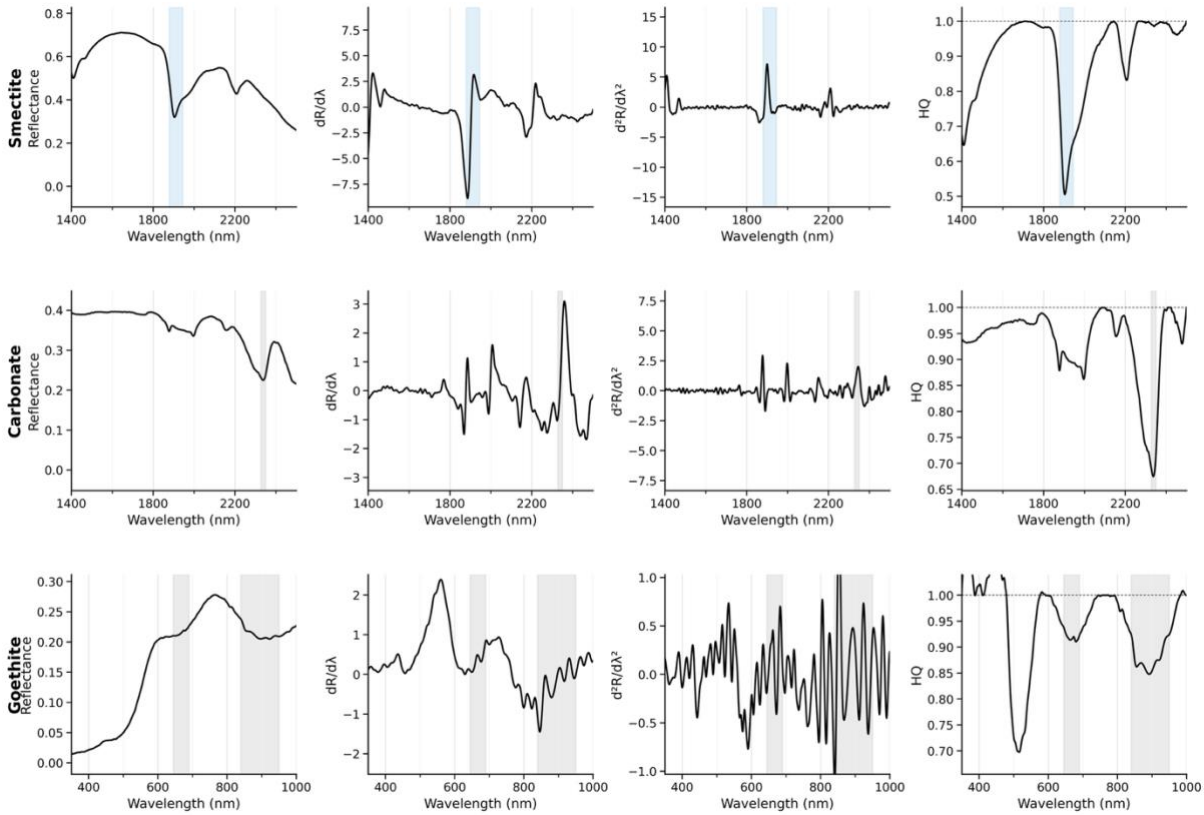

Figure 3.4. *Reference spectra of smectite, carbonate minerals and goethite used to guide wavelength-window selection for spectral-library and MAF construction, shown as reflectance (REF), first derivative (D1), second derivative (D2) and hull quotient (HQ). Blue shading indicates the broad approximately 1900 nm H_2O/OH hydration-sensitive absorption region, where applicable, whereas grey shading marks the selected SWIR CO_3-sensitive and VNIR Fe^{3+}-sensitive regions. These regions were guided by established VNIR–SWIR mineral-absorption behaviour and refined through visual inspection of the selected USGS Version 7 reference spectra (Hunt, 1977; van der Meer et al., 2012; Kokaly et al., 2017). The shaded intervals represent workflow-specific configuration windows rather than unique mineral-identification criteria.*

Mineral	Chemical formula	Mineral group	Primary window	Secondary window	Spectral meaning
Kaolinite	$Al_2Si_2O_5(OH)_4$	Clay – kaolin group	2160–2195 nm	—	Al–OH kaolinite-sensitive
Illite	$K_{0.65}Al_2[Al_{0.65}Si_{3.35}O_{10}](OH)_2$	Clay – mica/illite group	2195–2225 nm	—	Al–OH illite-sensitive
Montmorillonite / Smectite	Variable Ca/Na-rich smectite	Clay – smectite group	1885–1945 nm	—	H_2O/OH hydration-sensitive
Chlorite	$(Mg,Fe,Al)_6(Si,Al)_4O_{10}(OH)_8$	Clay – chlorite group	2235–2270 nm	—	Mg–OH / Fe–OH chlorite-sensitive
Dolomite	$CaMg(CO_3)_2$	Carbonate	2330–2344 nm	—	CO_3 dolomite-sensitive
Calcite	$CaCO_3$	Carbonate	2330–2344 nm	—	CO_3 calcite-sensitive
Goethite	FeO(OH)	Fe oxyhydroxide	890–920 nm	645–690 nm	VNIR Fe^{3+} Fe-oxide-sensitive
Hematite	Fe_2O_3	Fe oxide	890–920 nm	645–690 nm	VNIR Fe^{3+} Fe-oxide-sensitive

Table 3.2. *Target minerals and mineral-sensitive wavelength windows used to guide spectral-library selection and MAF construction. The windows were based on established VNIR–SWIR absorption regions and refined through visual inspection of the selected USGS Version 7 reference spectra (Hunt, 1977; van der Meer et al., 2012; Kokaly et al., 2017). They represent workflow-specific configuration intervals rather than unique mineral-identification criteria in isolation.*

3.4 Spectral pre-treatment

Spectra were evaluated in four domains: reflectance (REF), hull quotient (HQ), first derivative (D1) and second derivative (D2). Reflectance preserved the calibrated spectral shape and level. Hull quotient, implemented as continuum removal by division against the upper convex hull, suppressed broad continuum effects and enhanced relative absorption troughs (Clark and Roush, 1984). First- and second-derivative transforms emphasise slope changes and subtle absorption structure but can also amplify high-frequency noise and edge artefacts (Savitzky and Golay, 1964; Tsai and Philpot, 1998). The same pre-treatment was applied to core and reference-library spectra.

Hull quotient was calculated in MINSPEC as the reflectance divided by the fitted continuum:

$$HQ(\lambda) = \frac{R(\lambda)}{C(\lambda)} \tag{3.2}$$

where R(λ) is the reflectance spectrum and C(λ) is the continuum fitted over the selected wavelength interval. For candidate feature-based products used during proxy screening, feature depth at a band center λ_B was calculated as:

$$D(\lambda_b) = 1 - \frac{R(\lambda_b)}{C(\lambda_b)} \tag{3.3}$$

Feature area over the interval λ_1 to λ_2 was calculated as:

$$A = \int_{\lambda_1}^{\lambda_2} \left[1 - \frac{R(\lambda)}{C(\lambda)}\right] d\lambda \tag{3.4}$$

First-derivative spectra were calculated as:

$$\frac{dR}{d\lambda} \approx \frac{R(\lambda_{i+1}) - R(\lambda_{i-1})}{\lambda_{i+1} - \lambda_{i-1}} \tag{3.5}$$

Second-derivative spectra were calculated as:

$$\frac{d^2R}{d\lambda^2} \approx \frac{R(\lambda_{i+1}) - 2R(\lambda_i) + R(\lambda_{i-1})}{(\Delta\lambda)^2} \quad (3.6)$$

No additional smoothing filter was applied before derivative calculation. Before line averaging, unusable lateral margins were masked (about 2.5 cm from the left and 1 cm from the right of the core image) to remove cracks, irregular edge geometry, and edge artefacts, and only the effective VNIR and SWIR ranges were retained. Three downcore intervals were treated as non-sediment or artefact zones and masked (0.0–17.5 cm-top foam or non-sediment; 98.0–99.5 cm-a section-boundary; and 544.5–548.0 cm – core catcher imprint with foam).

3.5 HSi-derived outputs and spectral unmixing

HSi-derived variables were generated through two routes:

Route A: used MINSPEC unmixing: the calibrated cubes, the customized MAF and the study-specific library to generate mineral surface maps.

Route B: extracted spectral proxies from the pre-treated, line-averaged spectra (single-band, diagnostic-window and feature-depth variables). The line-averaged data were generated at 1 mm downcore resolution, reducing the three-dimensional HSi cube to a two-dimensional downcore product that was easier to work with while testing the different approaches in Python.

Linear spectral unmixing represents a measured spectrum as a combination of reference endmember spectra and a residual:

$$\mathbf{x} = \mathbf{S}\mathbf{a} + \mathbf{e}, \quad \mathbf{a} \geq 0, \quad \sum_i a_i = 1 \quad (3.7)$$

where x is the measured spectrum, S the matrix of reference endmember spectra, a the vector of endmember contributions and e the residual; non-negativity ($a \geq 0$) and sum-to-one ($\Sigma a = 1$) constraints may be applied (Adams et al., 1986; Keshava and Mustard, 2002; Bioucas-Dias et al., 2012). In this study MINSPEC unmixing used the software's internal implementation. Maps were exported on a 0–100 scale and interpreted as relative spectral contributions, with −999 values treated as no-data and masked. To assess sensitivity to pre-treatment, unmixing was applied across the REF, HQ, D1 and D2 domains.

3.6 Depth matching, profile averaging and invalid intervals

For comparison with the laboratory data, HSi products were reduced to one-dimensional downcore profiles by averaging valid pixel values across the usable core width at each depth step, after masking margins and artefacts (Section 3.4). The downcore mean for depth interval j was calculated as:

$$\bar{z}_j = \frac{1}{n_j} \sum_i z_{ij} \quad (3.8)$$

where $\bar{z}_j$ is the mean HSi value for depth interval j, z_{ij} is the individual valid spectral or proxy value within that interval, and n_j is the number of valid observations. Because HSi is continuous in depth whereas XRD and XRF are discrete, each reference sample was matched to the HSi profiles using a

±0.5 cm half-window around its reported depth, averaging all valid HSi values within the window. The same matching rule and half-window were used in all analyses.

3.7 Empirical single-band proxy screening and local ±6-band robustness

Single-band screening identified, for each target, the individual wavelength and spectral product most strongly associated with the corresponding reference variable. Candidate bands were evaluated across the REF, HQ, D1 and D2 products. For each band the depth-matched HSi value was compared with the reference variable using Pearson R, Pearson R^2, Spearman R and the number of matched observations. Bands were ranked by Pearson R^2 because both positive and negative relationships are meaningful. Pearson R was retained to preserve the direction of the relationship.

Screening used target-specific windows derived from known mineral-sensitive regions and the library/MAF design:

- kaolinite and illite in the Al–OH clay region (2155–2230 nm), against XRD;
- chlorite in the Mg–Fe–OH region (2230–2290 nm), against XRD chlorite;
- smectite in a hydration-sensitive window (1850–1960 nm) with a secondary Al–OH test (2155–2230 nm), against XRD smectite;
- carbonate/Ca in the carbonate-sensitive SWIR region (2310–2360 nm), against XRF Ca; and
- Fe in the Fe-sensitive VNIR region (850–950 nm), against XRF Fe.

Clay-mineral targets were screened against the 104 matched XRD samples and carbonate/Ca and Fe against the 1051 matched XRF measurements. The selected spectral proxies and their statistics are reported in Section 4.4.

For each spectral proxy, the six neighbouring bands on either side of the selected wavelength were compared with the same reference variable. This test determined whether the selected-band relationship represented a coherent local spectral response rather than an isolated, band-specific effect. Stability was summarised by the same-sign fraction and the median Pearson R^2 drop across the neighbourhood. A proxy was classified as stable when these values were ≥ 0.80 and ≤ 0.05, respectively, moderately stable when they were ≥ 0.65 and ≤ 0.10, and otherwise locally narrow. A locally narrow response was considered more sensitive to exact band selection, noise or small spectral shifts and was therefore interpreted cautiously rather than automatically rejected. Outcomes are reported in Section 4.4.1.

3.8 Diagnostic-window feature-depth metrics

Diagnostic-window feature metrics are commonly used in spectroscopy, and include the depth, area and central position of mineral diagnostic absorption bands (Figure 3.5). Feature depth was used in this work to quantify absorption strength from the reflectance spectra as it provided better initial results than feature area or position.

To obtain the feature depth. a local linear continuum was fitted between the reflectance values at the two window limits. The absorption minimum was then identified, and feature depth was measured as the vertical distance between the spectrum and the continuum at that position (Eq. 3.3). The calculation was applied independently to every valid REF line-average spectrum. Each depth row therefore produced one feature-depth value. For LRG07-PC04, the procedure was repeated for all 5259 valid depth rows to generate a continuous downcore feature-depth series. Figure 3.6 illustrates the workflow using two real examples from approximately 200 and 400 cm. These spectra are shown only to demonstrate the calculation; the subsequent analysis used the complete feature-depth series.

The feature-depth series was then aligned with the corresponding mineral-abundance or geochemical profile at common depth positions. Comparisons were made using all available paired observations, and the coefficient of determination was calculated from the complete set of matched depth values. This provided a direct test of whether the empirical band relationships described in Section 3.7 were associated with absorption features.

The diagnostic windows were:

- Al–OH clay, 2155–2230 nm, compared with kaolinite and illite;
- chlorite Mg–Fe–OH, 2230–2290 nm, compared with chlorite;
- carbonate/Ca, 2310–2360 nm, compared with XRF Ca;
- Fe-sensitive VNIR, 850–950 nm, compared with XRF Fe; and
- clay hydration, 1850–1960 nm, compared with smectite.

The Al–OH interval was treated as a combined clay-OH feature rather than as a mineral-specific kaolinite or illite absorption. The carbonate/Ca window was used as an empirical Ca-sensitive test. The hydration window was interpreted cautiously because it is strongly influenced by water content, moisture state and surface conditions. Results are presented in Section 4.5.

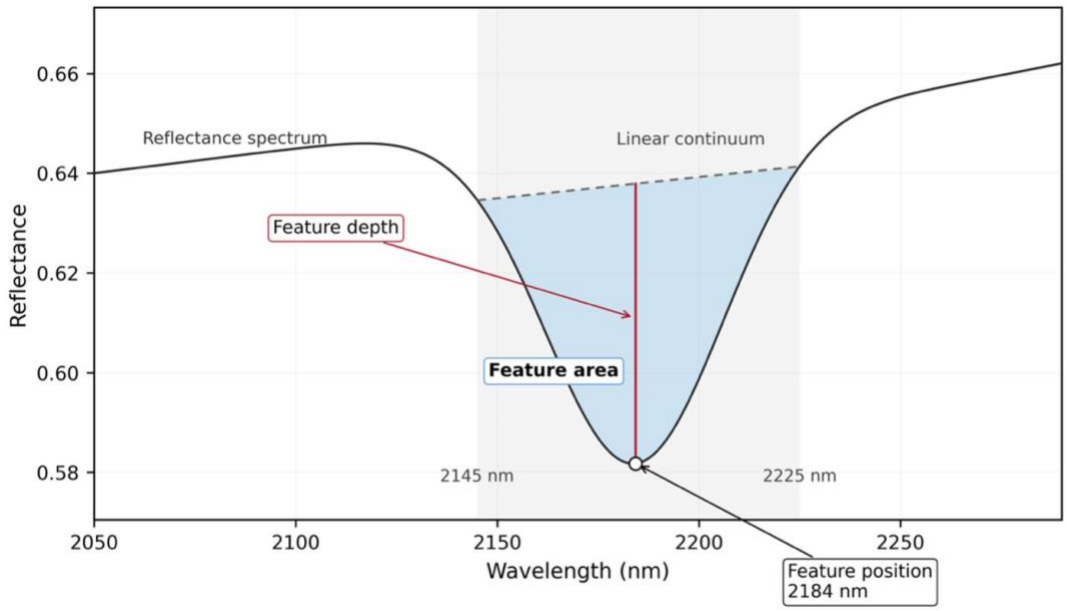

Figure 3.5. *Absorption-feature parameters extracted from reflectance spectra relative to a fitted continuum across a selected interval: feature position (wavelength of the absorption minimum), feature depth (vertical difference between continuum and minimum) and feature area (integrated area between continuum and spectrum).*

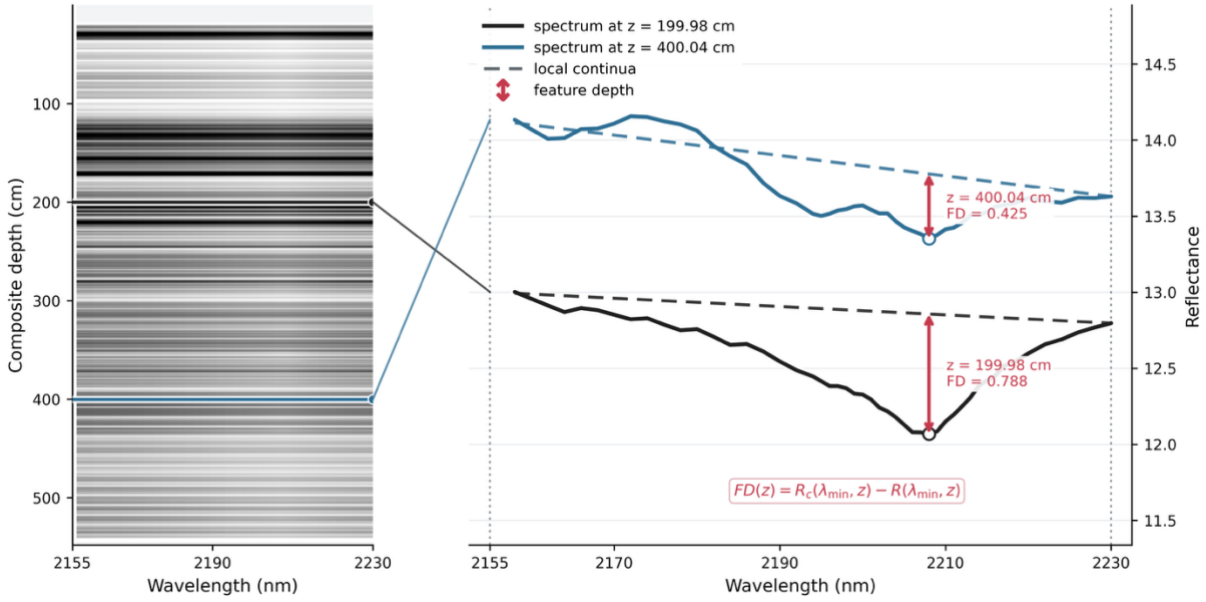

Figure 3.6. *Application of the feature-depth calculation to real REF line-average spectra from LRG07-PC04. Two depth rows are shown as examples, while the same calculation was applied independently to all valid depth rows used in the analysis.*

3.9 Partial least squares regression (PLSR) of clay minerals

PLSR was used as a supervised calibration to model the XRD relative clay-mineral proportions from the SWIR data. PLSR suits hyperspectral data because adjacent bands are highly collinear and the predictors can be numerous relative to the samples (Geladi and Kowalski, 1986; Wold et al., 2001). It decomposes the predictor matrix X and response y into latent structures and predicts from the regression coefficients:

$$\mathbf{X} = \mathbf{T}\mathbf{P}^{\top} + \mathbf{E}, \qquad \mathbf{y} = \mathbf{T}\mathbf{q} + \mathbf{f}, \qquad \hat{\mathbf{y}} = b_0 + \mathbf{X}\mathbf{b} \tag{3.9}$$

where T are the latent scores, P the predictor loadings, q the response loading, E and f the residuals, b the regression coefficients and b_0 the intercept.

Separate single-target models were built for kaolinite, illite, chlorite and smectite. Carbonate/Ca and Fe were not modelled, because their references are XRF intensities. Predictors were line-averaged SWIR spectra from REF, HQ, D1 and D2, tested over three window levels: the full SWIR range (about 1350–2450 nm), a broad clay-OH window (about 2050–2350 nm) and a target-focused window from the proxy screening. The tested ranges are illustrated in Figure 3.7. For each XRD depth, HSi spectra were

averaged within a ±0.5 cm half-window (Section 3.6), and only XRD samples with valid matched spectra were used.

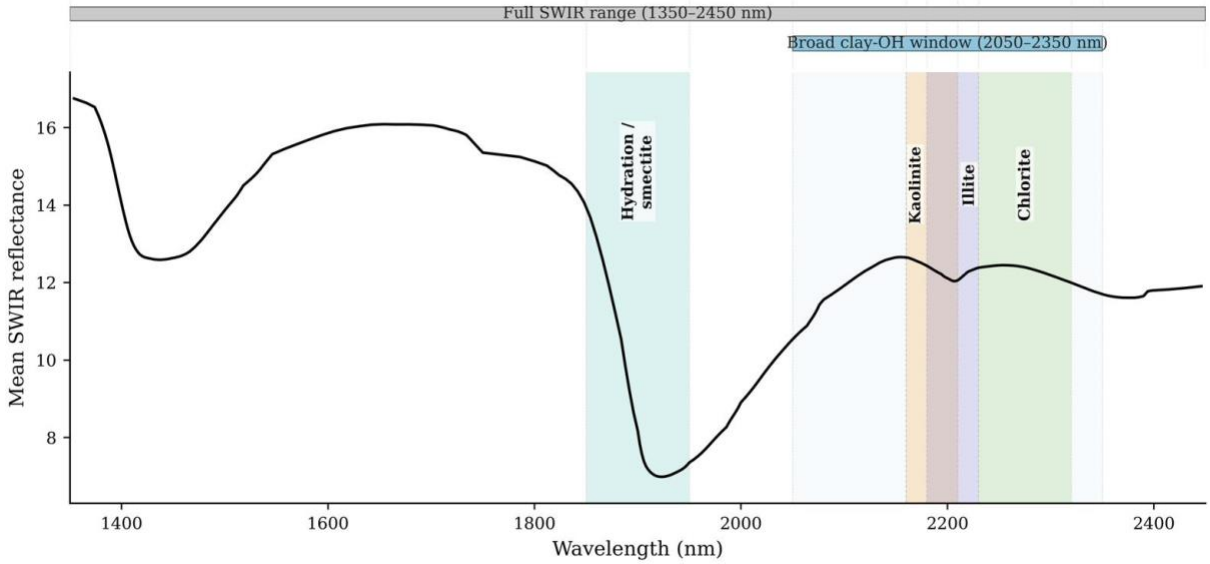

Figure 3.7. *Example mean line-averaged SWIR reflectance spectrum from core LRG07-PC04 with the wavelength ranges used for PLSR modelling. The upper bars show the full SWIR range and the broad clay-OH interval, while shaded vertical intervals mark the target-focused windows used for kaolinite, illite, chlorite and the hydration/smectite-sensitive response. These windows define modelling intervals rather than uniquely diagnostic mineral-identification regions.*

Modelling used the PLSR regression algorithm in scikit-learn (Pedregosa et al., 2011). Candidate models used 1–10 latent components, with a parsimony tolerance of $\Delta R^2 = 0.02$ favoring the simpler model.

Two cross-validation schemes were used. In ordinary random five-fold cross-validation the samples are shuffled and split into five folds at random; because neighboring depths in a slowly accumulating core are very similar, this places near-identical samples in both the training and the test folds and tends to flatter the model. Depth-blocked five-fold cross-validation splits the core into five contiguous depth intervals, so that the model is always tested on a stretch of core it was not trained on. This is what is meant by an out-of-fold prediction. For every sample, the predicted value comes from a model fitted only on the other folds, so the sample was never seen during its own prediction. Depth-blocked validation was therefore used, with random cross-validation kept only as an optimistic reference. Each candidate was evaluated by Pearson R, Pearson R^2, the predictive R^2 score, the root-mean-square error (RMSE, the typical size of the prediction error in % age units) and the mean absolute error (MAE, the average absolute error in the same units).

Because the number of matched XRD samples is modest (N = 104 for the clay minerals), the statistical significance of each retained relationship was also assessed. For the correlation-based results, the p-value of the Pearson correlation was computed, and a relationship was considered significant at $p < 0.05$; for N = 104, this corresponds to |R| greater than about 0.19, and for the 1051 matched XRF samples to |R| greater than about 0.06. These significance levels are reported alongside the R and R^2 values in Chapter 4.

A model was retained only if both the depth-blocked Pearson R and the depth-blocked predictive R^2 score were positive; a positive Pearson R^2 alone was insufficient, because it can remain positive when

the predictive R^2 score is zero or negative. Three classes were used: retained primary (positive R, positive R^2 score, Pearson $R^2 \geq 0.40$); retained with caution (positive R, positive R^2 score, Pearson R^2 between 0.20 and 0.40); and tested but not retained. Retained models were refitted on all valid XRD-matched samples and applied to the continuous line-averaged SWIR series to generate downcore prediction profiles. Selected models and their validation statistics are reported in Section 4.6.

3.9.1 Closure and residual-smectite sensitivity test

Smectite was the only clay mineral where the PLSR results were not retained. Because the XRD variables are compositional and sum to 100%, whereas the four single-target models were fitted independently, the predictions were not expected to preserve closure. A closure sensitivity test evaluated how the independent predictions behaved in compositional space and whether the weak smectite response could be examined as a residual. The three clay-mineral predictions (kaolinte, illite, chlorite) were summed at each XRD-matched depth and the deviation from 100% was calculated; a non-negative closed variant was produced by setting negative predictions to zero and renormalising to 100%; and residual smectite was estimated as:

$$\hat{S}_{res} = 100 - (\hat{K} + \hat{I} + \hat{Ch}) \qquad (3.10)$$

This residual was compared with XRD smectite using the same metrics as the PLSR models. As an additional check, a PLS2 model was run. Instead of fitting one mineral at a time, PLS2 predicts all four clay minerals together in a single model, which allows the shared spectral structure among them to be used but still does not force the predictions to sum to 100%.

3.10 PCA/VPCA spectral-structure analysis

Principal component analysis (PCA) and varimax-rotated PCA (VPCA) were applied as unsupervised analyses of spectral structure. The motivation for including PCA was its historical use in mineral identification using *derivative reflectance spectroscopy* in Arctic sediments (Ortiz, 2011) Unlike PLSR, PCA does not use reference data during fitting. The XRD and XRF variables were correlated with the component scores after fitting to assess the mineralogical or geochemical relevance of the dominant spectral modes. Where a component showed a strong reference association, its downcore score profile was also plotted against the corresponding XRD or XRF profile and against the best single-target predictor from the other approaches. The main SWIR run used SWIR_D1 over the clay/OH window (2155–2330 nm), targeting Al–OH and Mg/Fe–OH structure, and the main VNIR run used VNIR_D1 over about 500–950 nm, targeting Fe-, colour- and provenance-related derivative structure. The VNIR derivative run follows the established use of VNIR derivative reflectance and varimax-rotated PCA to extract mineral- and provenance-related modes from Arctic marine sediment (Ortiz, 2011). Three supplementary runs (SWIR_D2, VNIR_REF, VNIR_HQ) were also tested (Table 3.3).

All runs were fitted to valid sediment intervals, excluding the non-sediment and artefact zones (Sections 3.4, 3.6); bands with insufficient valid data were removed, and retained variables were median-imputed and standardised before PCA. Up to eight components were retained per run. Varimax rotation was applied as an interpretive orthogonal rotation that redistributes variance among components without changing the total variance represented and without creating a predictive model. For each run, the exported outputs included explained variance, downcore PC and rotated-PC score profiles, PC/RC correlations with XRD and XRF variables, and the strongest positive and negative loading wavelengths. Results are reported in Section 4.7.

Run ID	Status	Product	Window (nm)	Spectral purpose	Bands	Depths
MAIN_SWIR_D1_CLAY_2155_2330	Main	SWIR_D1	2155–2330	Clay/OH structure; Al–OH and Mg/Fe–OH region	74	5259
MAIN_VNIR_D1_500_950	Main	VNIR_D1	~500–950	VNIR derivative Fe/provenance/colour structure	168	5259
SUPP_SWIR_D2_CLAY_2155_2330	Supplementary	SWIR_D2	2155–2330	Second-derivative clay/OH curvature check	74	5259
SUPP_VNIR_REF_500_950	Supplementary	VNIR_REF	~500–950	Raw VNIR reflectance sensitivity check	168	5259
SUPP_VNIR_HQ_500_950	Supplementary	VNIR_HQ	~500–950	Continuum-normalised VNIR sensitivity check	168	5259

Table 3.3. *PCA/VPCA run inventory used for unsupervised spectral-structure analysis. Two main runs (SWIR_D1 over 2155–2330 nm; VNIR_D1 over about 500–950 nm) and three supplementary sensitivity-check runs (SWIR_D2, VNIR_REF, VNIR_HQ). All runs were fitted only to HSi spectra from valid sediment intervals; XRD and XRF data were not used during fitting but were used afterwards to interpret component scores through depth-matched correlations. Up to eight components were retained per run.*

3.11 Treatment of compositional clay-mineral data

The four XRD clay minerals are relative proportions that sum to 100% at each depth, so they are not independent: if one increases, the others must fall. A statistically complete treatment would transform them into log-ratios (for example, centered or isometric log-ratios) before regression. Here the four minerals were instead modelled as raw relative% ages using independent single-target PLSR calibrations, without log-ratio transformation and without enforcing closure, because this keeps each model directly interpretable against its own XRD reference and comparable with the direct-proxy and PCA/VPCA results.

4. Results

This chapter first reports the mineralogical and geochemical composition of LRG07-PC04 from the reference data and then reports on the HSi-based approaches to predicting that composition.

4.1 Core-scale visual and sedimentological characteristics

PC-04 shows pronounced downcore variability in lithology, clay mineralogy, geochemistry and hyperspectral appearance (Figure 4.1). The upper and middle core alternates between sand, clayey sand, sandy clay and clay, with sandy and mixed units most common above about 380–400 cm, where lithology changes frequently over short intervals. Below this, the core becomes more clay-rich, although smaller-scale variability persists. Bulk density ranges from about 1.65 to 1.95 g cm^{-3}, with higher values broadly coinciding with coarser units and lower values in finer, clay-rich intervals. The VNIR and SWIR false-colour composites reveal clear spectral contrasts across the split-core surface, including where colour differences are subtle, and demonstrate directly how variable the spectral response is downcore.

4.2 Reference mineralogical and geochemical patterns

The XRD record shows clear downcore variability in the relative proportions of the four clay minerals (Figure 4.1). Illite is dominant on average (16.2–47.9%; mean 36.2%), followed by chlorite (8.8–33.1%; mean 24.0%), smectite (3.4–60.6%; mean 21.0%) and kaolinite (7.9–45.5%; mean 18.7%). Kaolinite is

enriched in the upper 100 cm where it commonly exceeds 25–35%, with further peaks near 200.5, 274.5–294.5 and 354.5–384.5 cm, and decreases below about 400 cm to mostly 8–18%. Illite remains moderate to high throughout and lacks the sustained lower-core decrease seen in kaolinite. Chlorite varies within a narrower range, mostly 20–28%. Smectite is irregular, with a pronounced maximum near 372.5 cm and higher values near 178.5–184.5 cm and in parts of the lower core. Because the variables are closed, some inverse relationships among components are expected, the clearest being between the kaolinite-rich upper and middle intervals and the smectite-rich intervals around 360–380 cm.

The XRF record shows a different structure (Figure 4.1). Ca intensities are elevated mainly in the upper and middle core, with high-Ca intervals at about 19–33, 119–172, 204–222 and 244.5–246.5 cm and the highest value at 209 cm, then decrease strongly below about 250 cm. Fe is more variable, reaching a maximum at 76.5 cm and remaining comparatively high and variable in several lower-core intervals, especially below about 400 cm. The Ca and Fe profiles therefore follow distinct downcore patterns, with Ca enriched in the upper and middle core and Fe high and variable elsewhere.

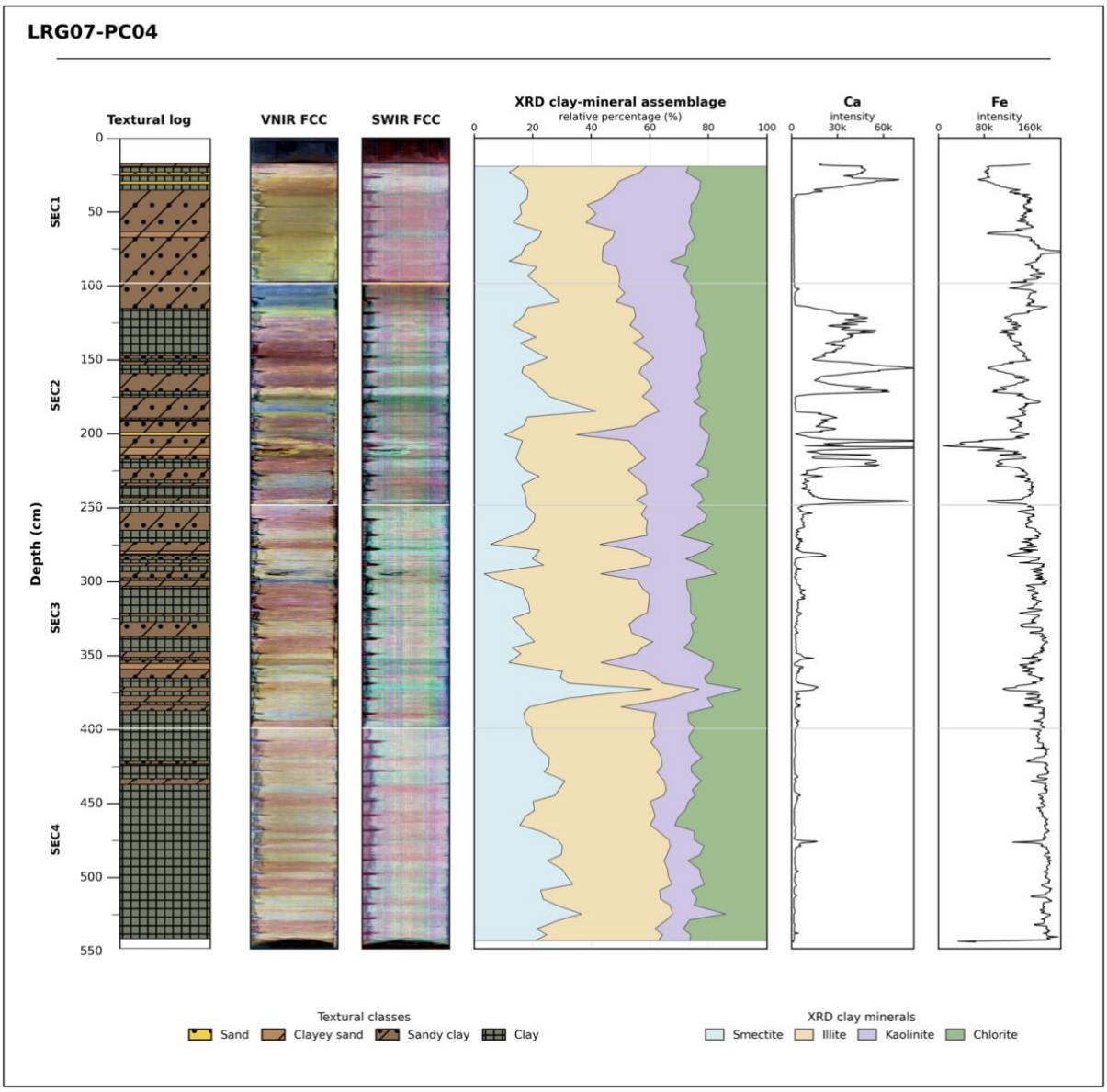

Figure 4.1. *Core-scale overview of LRG07-PC04. From left to right: textural log; XRD clay-mineral assemblage (relative% ages of smectite, illite, kaolinite and chlorite); XRF Ca intensity; XRF Fe intensity; and the VNIR and SWIR false-colour composites. The false-colour composites illustrate how variable the spectral response is across the split-core surface. Section boundaries are at 98, 248 and 399 cm.*

4.3 MINSPEC unmixing comparison

MINSPEC unmixing outputs were compared with the XRD and XRF reference data across the REF, HQ, D1 and D2 domains, with each mineral map reduced to a line-averaged downcore mean profile (Table 4.1). The results were generally poor but varied strongly among targets and domains. Kaolinite produced a usable response in the reflectance and hull-quotient domains, with hull quotient the most suitable MINSPEC product ($R = 0.32$, $R^2 = 0.10$). Chlorite- and Fe-oxide-sensitive outputs were best expressed in first-derivative form (chlorite $R = 0.31$; Fe $R = 0.43$, $R^2 = 0.18$), whereas carbonate and smectite/hydration showed their strongest, though still weak, responses in second-derivative form. Illite produced no coherent or interpretable unmixing signal in any tested domain.

Although spectral unmixing was the preferred approach when starting this project, it quickly became apparent that other methods produced superior results. Judged directly on the maps themselves, most of the MINSPEC outputs are unconvincing. They show strong cross-core variation, a generally noisy appearance, and mineral concentrations that are commonly enhanced along the edges of the cores, which is an acquisition artefact rather than real mineral enrichment. The kaolinite and, to a lesser extent, the Fe-oxide maps are the only ones with a spatially coherent structure that tracks the reference data.The illite, smectite and carbonate maps do not. Across targets, the unmixing outputs are generally weaker than the single-band proxies reported in Section 4.4.

Target	Reference	REF R / R^2	HQ R / R^2	D1 R / R^2	D2 R / R^2	Best
Carbonate total	XRF Ca	−0.02 / 0.00	0.07 / 0.01	no signal	0.08 / 0.01	D2
Kaolinite	XRD Kaolinite	0.31 / 0.10	0.32 / 0.10	0.15 / 0.03	0.16 / 0.03	HQ
Illite	XRD Illite	no signal	no signal	no signal	no signal	—
Chlorite	XRD Chlorite	no signal	no signal	0.31 / 0.10	no signal	D1
Smectite / hydration	XRD Smectite	0.14 / 0.03	0.16 / 0.03	0.19 / 0.04	0.24 / 0.06	D2
Fe-oxide total	XRF Fe	0.31 / 0.10	0.37 / 0.14	0.43 / 0.18	0.39 / 0.16	D1

Table 4.1. *MINSPEC unmixing-domain comparison across spectral products. For each target, MINSPEC unmixing-derived mean profiles from the REF, HQ, D1 and D2 domains were compared with the corresponding XRD or XRF reference variable; values are Pearson R / R^2. "No signal" indicates no coherent or interpretable unmixing response. The "Best" column identifies the most suitable MINSPEC output per target, which does not necessarily become the final selected HSi proxy.*

4.4 Selected empirical single-band proxies

Single-band screening identified the wavelength and spectral product most strongly associated with each reference variable (Table 4.2). The strongest relationships were spread across the first derivative, second-derivative and hull-quotient products rather than concentrated in one. Kaolinite was best represented by a SWIR first-derivative response at 2204 nm in the Al–OH window ($R = 0.660$, $R^2 = 0.440$), and illite by a SWIR second-derivative response at 2195 nm in the same region ($R = 0.480$, $R^2 = 0.230$). Chlorite showed a weaker but interpretable relationship with a SWIR first-derivative band at 2278 nm in the Mg–Fe–OH window ($R = 0.450$, $R^2 = 0.200$). Smectite was the weakest clay-mineral target, its best proxy being a SWIR hull-quotient response at 1854 nm in the hydration window ($R = −0.210$, $R^2 = 0.040$).

For the geochemical targets, carbonate/Ca was best represented by a SWIR second-derivative response at 2330 nm ($R = 0.570$, $R^2 = 0.320$) and Fe by a VNIR first-derivative response at 919.6 nm ($R = -0.600$, $R^2 = 0.360$). All of these relationships are statistically significant ($p < 0.001$) except smectite, which is significant only at $p \approx 0.01$ and explains very little variance; for $N = 104$ the significance threshold is $|R| \approx 0.19$, so smectite is above the threshold but weak. The negative signs for smectite and Fe reflect the sign convention of the derivative or transformed response and do not, by themselves, imply an inverse mineralogical relationship.

Target	Product	Window (nm)	λ (nm)	Pearson R	Pearson R^2	Spearman R	p	N
Kaolinite	SWIR_D1	2155–2230	2204	0.660	0.440	−0.708	<0.001	104
Illite	SWIR_D2	2155–2230	2195	0.480	0.230	0.592	<0.001	104
Chlorite	SWIR_D1	2230–2290	2278	0.450	0.200	0.446	<0.001	104
Smectite	SWIR_HQ	1850–1960	1854	−0.210	0.040	−0.196	≈0.01	104
Carbonate/Ca	SWIR_D2	2310–2360	2330	0.570	0.320	0.537	<0.001	1051
Fe	VNIR_D1	850–950	919.6	−0.600	0.360	−0.645	<0.001	1051

Table 4.2. *Selected empirical single-band spectral proxies. Bands were selected by maximum Pearson R^2 within target-specific search windows across the REF, HQ, D1 and D2 products. The p column reports the significance of the Pearson correlation. Negative R values indicate inverse relationships between the transformed spectral variable and the reference dataset and are common for derivative-based products. The bands are empirical proxies, not direct abundance measurements or feature-depth metrics.*

4.4.1 Local ±6-band stability of selected proxies

The ±6-band robustness test assessed whether each selected proxy represented a locally coherent response or a narrow, wavelength-specific maximum (Table 4.3). Illite, chlorite, smectite and Fe retained the same correlation sign across all neighboring bands. Illite (SWIR_D2 2195 nm) showed a median local R^2 of 0.216 against a best-band R^2 of 0.230 and was classified as stable; chlorite (SWIR_D1 2278 nm) was stable with a median local R^2 of 0.193 against 0.200; and Fe (VNIR_D1 919.6 nm) was stable with 0.355 against 0.360. Smectite was also sign-consistent but very weak, with a best-band R^2 of 0.040 and a median local R^2 of 0.024, showing that local sign stability alone does not imply a strong mineral-specific proxy. Kaolinite (SWIR_D1 2204 nm) had the strongest single-band relationship but a lower same-sign fraction (0.77), indicating a strong but locally narrow response; carbonate/Ca (SWIR_D2 2330 nm) was similarly narrow. The test therefore separates proxy strength from proxy robustness. Illite, chlorite and Fe are locally stable; kaolinite and carbonate/Ca are strong but locally concentrated; and smectite is sign-consistent but too weak to be a robust mineral-specific proxy.

Target	Product	λ (nm)	Best R^2	Median local R^2	Same-sign fraction	Stability class
Kaolinite	SWIR_D1	2204	0.440	0.397	0.77	narrow
Illite	SWIR_D2	2195	0.230	0.216	1.00	stable
Chlorite	SWIR_D1	2278	0.200	0.193	1.00	stable
Smectite	SWIR_HQ	1854	0.040	0.024	1.00	stable but weak
Carbonate/Ca	SWIR_D2	2330	0.320	0.143	0.85	narrow
Fe	VNIR_D1	919.6	0.360	0.355	1.00	stable

Table 4.3. *Local ±6-band stability summary for the selected empirical proxies. For each best band, six neighboring bands on either side were evaluated for correlation-sign consistency and Pearson R^2 drop. The same-sign fraction is the proportion of neighboring bands sharing the selected band's correlation direction; median local R^2 summarises explanatory strength across the neighborhood. Stability class reflects local robustness, not overall proxy strength.*

4.5 Diagnostic-window feature-depth results

Feature-depth metrics tested whether the empirical single-band relationships correspond to coherent absorption features across physically defined windows, so that the two approaches can be compared for each target (Table 4.4). The Al–OH clay window (2155–2230 nm) gave the clearest diagnostic response, relating positively to XRD kaolinite (R = 0.440, R^2 = 0.200) and negatively to XRD illite (R = −0.470, R^2 = 0.220). The opposite signs indicate that this window captures a shared Al–OH clay response in which kaolinite and illite vary in opposite directions within the closed composition, rather than a species-specific feature. The chlorite, carbonate/Ca, Fe and smectite feature-depth metrics were much weaker. The chlorite Mg–Fe–OH window (2230–2290 nm) related only weakly to XRD chlorite (R = 0.070, R^2 = 0.000); the carbonate/Ca window (2310–2360 nm) was weak against XRF Ca (R = 0.110, R^2 = 0.010) despite the stronger single-band proxy; and the Fe window (850–950 nm) showed limited agreement with XRF Fe (R = 0.320, R^2 = 0.100). The smectite hydration window (1850–1960 nm) showed no meaningful relationship with XRD smectite (R = 0.000, $R^2 \approx 0.000$).

Compared directly with the specific-wavelength proxies of Section 4.4, feature depth is the weaker choice for every target. For kaolinite, illite, carbonate/Ca and Fe the specific derivative band explains substantially more reference variance than the corresponding feature-depth window, and for chlorite and smectite neither approach is strong. The practical implication is that the specific derivative band is the more effective product rather than the broader feature-depth window.

Feature (window, nm)	Target	Pearson R	Pearson R^2	Spearman R	Retention	N
Al–OH clay (2155–2230)	Kaolinite	0.440	0.200	0.311	retained with caution	104
Al–OH clay (2155–2230)	Illite	−0.470	0.220	−0.495	retained with caution	104
Chlorite Mg–Fe–OH (2230–2290)	Chlorite	0.070	0.000	0.111	tested, not retained	104
Carbonate/Ca (2310–2360)	Carbonate	0.110	0.010	0.520	tested, not retained	1051
Fe VNIR (850–950)	Fe	0.320	0.100	0.288	tested, not retained	1051
Hydration (1850–1960)	Smectite	0.000	0.000	−0.020	tested, not retained	104

Table 4.4. *Diagnostic-window feature-depth results. Feature depth was computed from REF spectra across fixed physical windows and compared with the matched XRD or XRF reference variable. Only the Al–OH clay window gives an interpretable, if non-species-specific, kaolinite–illite response; the other windows are weak. Retention labels indicate whether the feature-depth metric was carried forward as an interpretive check.*

4.6 PLSR clay-mineral prediction results

PLSR tested whether multi-band SWIR information could improve clay-mineral prediction beyond the single-band and feature-depth proxies, using depth-blocked out-of-fold validation as the primary criterion — that is, every prediction was made by a model that had not seen the sample's own stretch of core (Table 4.5). The retained models differed strongly among minerals. Kaolinite produced the strongest retained model (SWIR_D2, 2155–2330 nm, 3 components, 74 bands): depth-blocked R =

0.760, Pearson R^2 = 0.570, predictive R^2 score = 0.541, RMSE = 5.38. Illite was retained with caution (SWIR_HQ, 2155–2230 nm, 4 components, 49 bands): R = 0.660, Pearson R^2 = 0.430, R^2 score = 0.329, RMSE = 5.17; both R and R^2 are significant at $p < 0.001$. Chlorite was retained with caution as the weakest retained model (SWIR_REF, full 1350–2450 nm, 8 components, 297 bands): R = 0.480, Pearson R^2 = 0.230, R^2 score = 0.262, RMSE = 2.96; the broad full-SWIR selection indicates a distributed rather than narrowly diagnostic response. Smectite was tested but not retained (SWIR_REF, 1850–1960 nm, 10 components, 37 bands): although it gave a weak positive correlation (R = 0.330, Pearson R^2 = 0.110), its depth-blocked predictive R^2 score was slightly negative (−0.004, RMSE = 7.58), meaning it did not predict XRD smectite better than simply using the mean. Smectite is therefore shown explicitly as a tested but non-retained target rather than omitted.

The observed-versus-predicted plots show kaolinite with the clearest positive relationship and closest distribution around the 1:1 line, illite and chlorite with positive but more compressed relationships, and smectite with only a weak positive relationship. The retained models were then applied to the continuous line-averaged SWIR series to generate downcore prediction profiles (Section 4.9).

Target	Product	Window (nm)	Comp.	Bands	DB R	DB R^2	R^2 score	RMSE	Decision
Kaolinite	SWIR_D2	2155–2330	3	74	0.760	0.570	0.541	5.38	Retained primary
Illite	SWIR_HQ	2155–2230	4	49	0.660	0.430	0.329	5.17	Retained with caution
Chlorite	SWIR_REF	1350–2450	8	297	0.480	0.230	0.262	2.96	Retained with caution
Smectite	SWIR_REF	1850–1960	10	37	0.330	0.110	−0.004	7.58	Not retained

Table 4.5. *Selected single-target PLSR models and depth-blocked validation performance. Depth-blocked (DB) R and R^2 describe the observed–predicted correlation; the predictive R^2 score evaluates skill relative to the 1:1 line. A model was retained only when both the depth-blocked R and the predictive R^2 score were positive. All retained models are significant at $p < 0.001$; smectite is shown as tested but not retained because its R^2 score was negative despite a weak positive correlation.*

4.6.1 Closure and residual-smectite sensitivity test

Because the XRD proportions sum to 100% whereas the four PLSR models were fitted independently, the predictions were evaluated for compositional closure (Table 4.6; Figure 4.2). The four-mineral predicted sum was centered near 100% (mean 99.3%, median 99.5%) but ranged from 37.7 to 137.9%, with a mean absolute deviation of 5.7%, confirming that the predictions are near-closed on average but not constrained at individual depths. Residual smectite, calculated as 100 minus predicted kaolinite, illite and chlorite, related positively to XRD smectite (R = 0.469, R^2 = 0.220, predictive R^2 score = 0.209, RMSE = 6.73), an improvement over the slightly negative direct smectite model, but the relationship remained weak and dispersed and was not treated as a robust smectite prediction.

The PLS2 multi-output test likewise did not improve smectite enough to retain it, indicating that the weak smectite result reflects limited smectite-specific spectral predictability. The downcore profiles (Figure 4.2) show the predicted sum fluctuating around 100% and the residual-smectite profile reproducing some broad XRD variability but with incomplete agreement.

Test	Result	Interpretation
Four-mineral single-target PLSR sum	Mean 99.3%; median 99.5%; range 37.7–137.9%; mean absolute deviation from 100% = 5.7%.	Predictions centered near 100%, but closure not enforced; interpret as semi-quantitative, not closed compositional estimates.
Residual-smectite test	Residual = 100 − predicted (kaolinite + illite + chlorite); vs XRD smectite: R = 0.469, R^2 = 0.220, R^2 score = 0.209, RMSE = 6.73, N = 104.	Recovered part of the smectite variability but too weak to retain; supports treating smectite as poorly constrained.
PLS2 / multi-output test	No meaningful improvement sufficient to retain smectite.	Weakness is not only a closure issue; reflects limited smectite-specific spectral predictability in the tested SWIR data.

Table 4.6. *Closure and residual-smectite sensitivity-test summary for the single-target PLSR clay-mineral predictions. The independently predicted proportions are centered near 100%, but closure was not mathematically enforced; the residual-smectite test recovered part of the XRD smectite variability but not enough to retain smectite as a robust prediction target.*

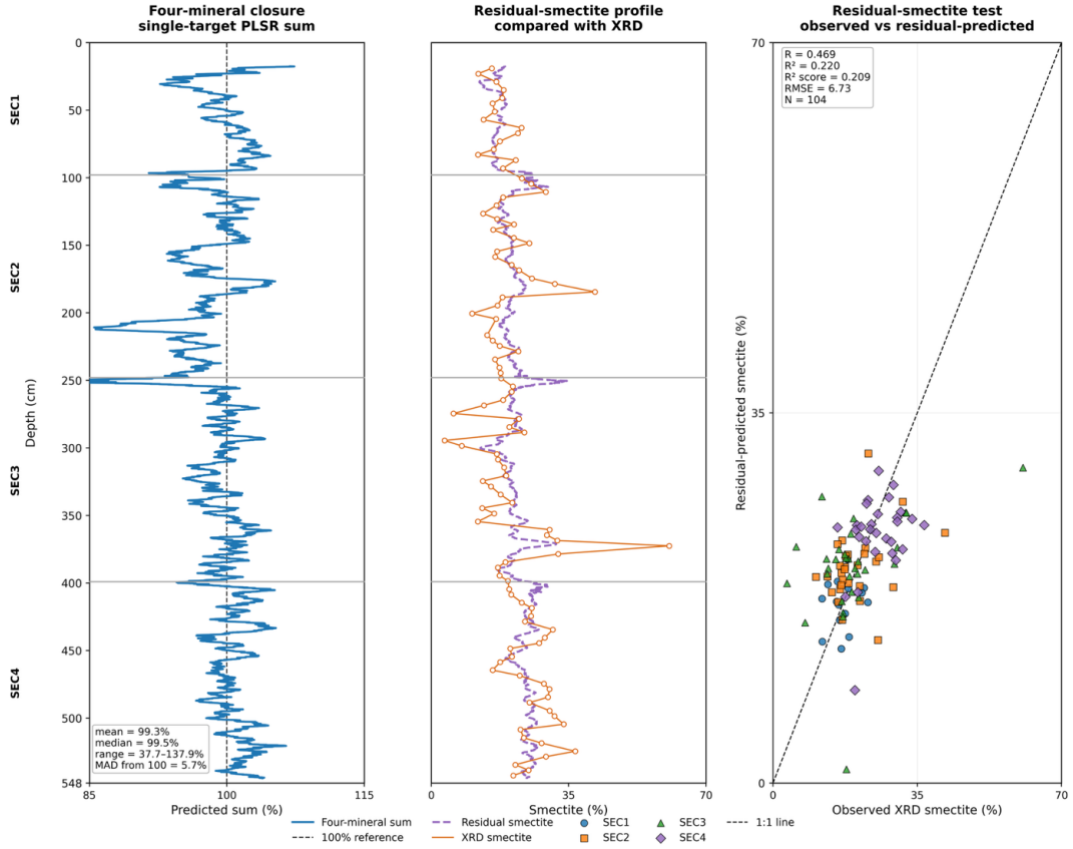

Figure 4.2. *Closure and residual-smectite sensitivity test. (A) Sum of the four independently predicted single-target PLSR proportions compared with the 100% closure reference. (B) Residual-smectite profile (100 − predicted kaolinite − illite − chlorite) compared with XRD smectite. (C) Observed XRD smectite versus residual-predicted smectite. The residual approach improves on the direct smectite model but remains too dispersed to support smectite as a robust retained prediction.*

4.7 PCA/VPCA spectral modes and reference correlations

PCA and varimax-rotated PCA (VPCA) were run as an independent, unsupervised route to the same targets. The main question is whether they recover the mineral structure as well as, or better than, the supervised methods (Table 4.7). The two main runs had different variance structures: in the SWIR_D1 clay/OH run the first five components explained 49.9, 22.6, 12.7, 5.9 and 4.1% of the variance, whereas in the VNIR_D1 run the first two components explained 47.1 and 39.2%, followed by 8.4, 2.0 and 1.3%. The strongest component–reference associations were target-specific. Kaolinite was most strongly associated with SWIR_D2 RC1 ($R = 0.690$, $R^2 = 0.480$) and illite with SWIR_D2 RC2 with opposite sign ($R = -0.630$, $R^2 = 0.390$), consistent with the shared Al–OH region and the closed composition. Chlorite was more weakly associated with SWIR_D1 RC2 ($R = 0.430$, $R^2 = 0.180$).

The geochemical associations were split between the two spectral regions. The strongest associations overall came from a single rotated SWIR_D2 mode that captures a Ca–Fe contrast (Ca with RC6, $R = 0.760$, $R^2 = 0.570$; Fe with the same component but opposite sign, $R = -0.700$; Ca/Sr also with RC6, $R = 0.723$), whereas the VNIR runs carried the Mn and colour-related structure, with Mn most strongly associated with VNIR_HQ RC2 ($R = 0.626$, $R^2 = 0.391$) and Sr more weakly with VNIR_D1 RC7 ($R = -0.479$). The VNIR derivative and hull-quotient components therefore add the Mn and colour/provenance structure that the SWIR clay run does not.

For the components with the strongest mineral associations, the downcore rotated-component scores were plotted against the matched XRD or XRF profile and against the best single-target predictor from Sections 4.4 and 4.6 (Figure 4.3D). These comparisons show that the leading kaolinite and Ca–Fe components track the reference profiles about as closely as the corresponding supervised proxies, but not more closely: VPCA reaches the same target ranking by an independent route rather than outperforming the supervised predictions.

Smectite again stands out as the exception. Its strongest component-level association was SWIR_D1 RC8 ($R = -0.300$, $R^2 = 0.090$), substantially weaker than kaolinite, illite, Ca or Fe, and it formed no clear independent component pattern. The PCA/VPCA results therefore reach the same target-wise conclusions as the supervised methods without using the reference data during fitting. Kaolinite and illite are expressed through Al–OH-sensitive SWIR modes, Ca and Fe through a strong contrasting SWIR_D2 mode, and smectite is not robustly resolved.

Target	Ref.	Run	PC/RC	Pearson R	Pearson R^2	Spearman R	N	Strength
Kaolinite	XRD	SWIR_D2	RC1	0.690	0.480	0.707	104	moderate
Illite	XRD	SWIR_D2	RC2	−0.630	0.390	−0.655	104	moderate
Chlorite	XRD	SWIR_D1	RC2	0.430	0.180	0.434	104	weak
Smectite	XRD	SWIR_D1	RC8	−0.300	0.090	−0.292	104	very weak
Ca	XRF	SWIR_D2	RC6	0.760	0.570	0.568	1051	strong
Fe	XRF	SWIR_D2	RC6	−0.700	0.490	−0.593	1051	moderate–strong
Mn	XRF	VNIR_HQ	RC2	0.626	0.391	0.643	1051	moderate
Sr	XRF	VNIR_D1	RC7	−0.479	0.229	−0.473	1051	weak–moderate
Ca/Sr	XRF	SWIR_D2	RC6	0.723	0.523	0.536	1051	strong

Table 4.7. *Priority PCA/VPCA component–reference associations. For each reference variable, the strongest absolute Pearson correlation with a PCA/VPCA component across the evaluated runs is reported, with Pearson R^2 as a strength measure and Spearman R as a rank-based comparison. VNIR runs contribute the Mn, Sr and colour/provenance structure; the SWIR_D2 RC6 mode carries the Ca–Fe contrast. PCA/VPCA reproduces the supervised target ranking without using the reference data during fitting.*

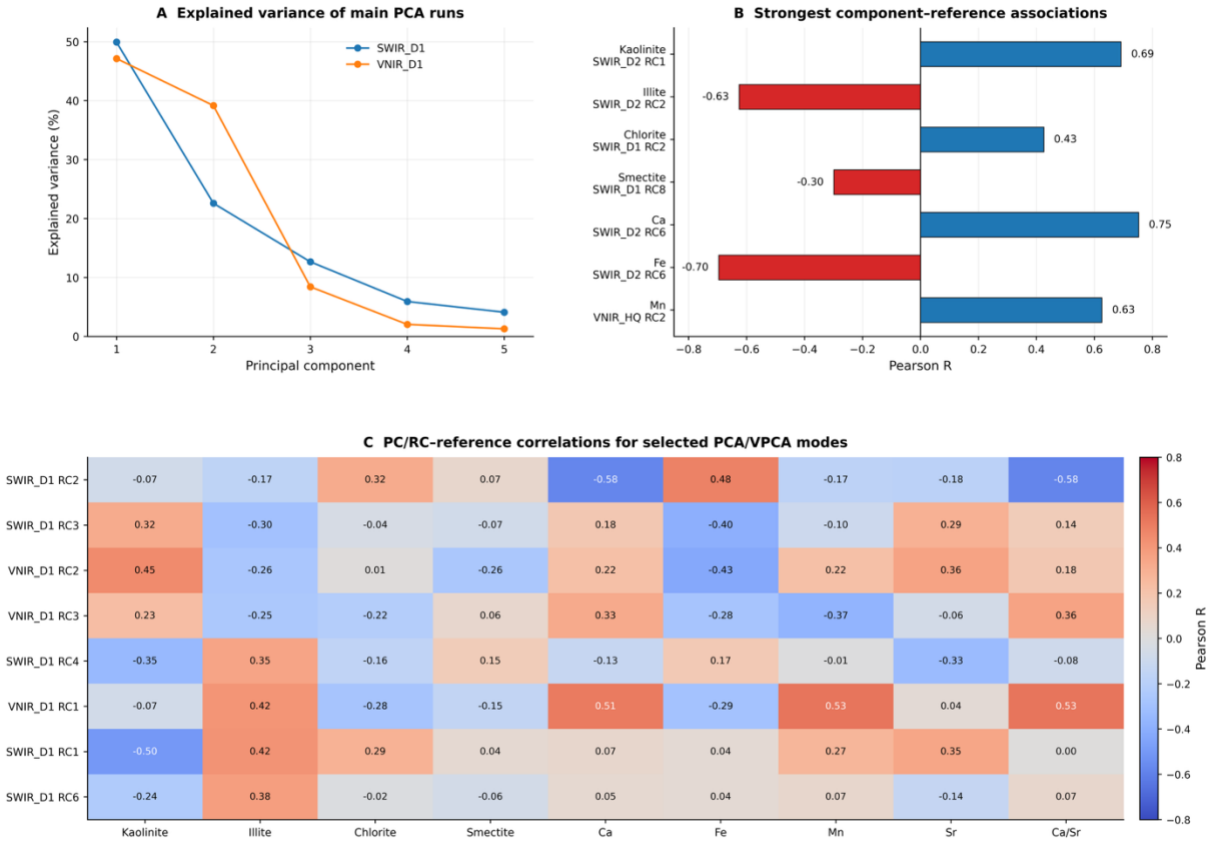

Figure 4.3. *PCA/VPCA spectral modes and reference correlations. (A) Explained variance of the first five unrotated components for the two main runs (SWIR_D1 and VNIR_D1). (B) Strongest component–reference associations across the evaluated runs for selected targets. (C) Pearson correlations between selected PC/RC modes from the main SWIR_D1 and VNIR_D1 runs and the XRD/XRF reference variables.*

4.8 Diagnostic controls on map recoverability

Bringing the per-target evidence together clarifies which MINSPEC unmixing maps worked (Table 4.8). Recoverability tracked the combination of reference dynamic range, feature specificity and feature–reference agreement rather than mineral presence alone. Kaolinite combined adequate XRD variability (P90–P10 = 17.7%) with a positive Al–OH feature-depth relationship (R = +0.440) and a usable, if weak, reflectance/hull-quotient unmixing response, and was the most recoverable clay target, though still only as a relative diagnostic map. Illite had comparable XRD variability but an inverse, shared Al–OH feature-depth relationship (R = −0.470) and produced no coherent unmixing signal in any domain. Chlorite had both a low XRD dynamic range (P90–P10 = 7.4%) and weak feature–reference agreement (R = +0.070) and was only weakly and domain-dependently recoverable. Smectite had adequate XRD variability but a null hydration-window relationship (R = 0.000) and was not

recoverable as a smectite-specific map. Carbonate/Ca showed a broad, weak carbonate-window relationship, and is reported as a Ca-related rather than a carbonate-abundance association, with XRF Ca retained as an elemental reference. Fe was partially recoverable as an Fe-related spectral and colour response (best D1 unmixing R = 0.43), with XRF Fe retained as an elemental reference. Only kaolinite and, more loosely, Fe yielded a map of interpretive value; the remaining targets are better served by the empirical proxies and PLSR.

Target	Reference range (P90–P10)	Feature-depth relation (Table 4.4)	MINSPEC unmixing (Table 4.1)	Recoverability
Kaolinite	17.74 (XRD)	Positive Al–OH: R = +0.440, R^2 = 0.200.	Best in HQ/REF: R ≈ 0.32.	Partially recoverable, as a relative diagnostic map.
Illite	16.58 (XRD)	Inverse Al–OH: R = −0.470, R^2 = 0.220.	No coherent signal in any domain.	Not recoverable as a stable map (poor endmember separability).
Chlorite	7.41 (XRD)	Very weak: R = +0.070, R^2 = 0.000.	Weak D1-only: R = 0.31.	Weakly recoverable at best.
Smectite / hydration	16.79 (XRD)	Null: R = 0.000, R^2 = 0.000.	Weak D2 only: R = 0.24.	Not recoverable as a smectite-specific map.
Carbonate / Ca	33 570 (XRF Ca)	Broad, weak: R = +0.110, Spearman +0.520.	Weak across domains.	Ca-related, not carbonate abundance.
Fe / Fe-oxide	66 332 (XRF Fe)	Weak–moderate: R = +0.320.	Best in D1: R = 0.43.	Partially recoverable as an Fe-related response.

Table 4.8. *Diagnostic controls on MINSPEC map recoverability. The table links reference dynamic range (robust P90–P10), feature-depth behaviour (Table 4.4) and unmixing-domain behaviour (Table 4.1) into a per-target recoverability interpretation. MINSPEC outputs are relative spectral-diagnostic products; XRF Ca and Fe are elemental reference variables, not carbonate or Fe-mineral abundances. The kaolinite–illite contrast is central: both have adequate XRD variability, but the Al–OH relationship is positive for kaolinite and inverse for illite, consistent with poor illite endmember separability.*

4.9 Mineral- and element-specific proxy panels

The following sections compare downcore variation in the MINSPEC map, the best empirical proxy, the feature-depth, PLSR model prediction and the VPCA so that the approaches can be judged side by side.

4.9.1 Kaolinite

Kaolinite is the best-constrained clay-mineral target (Figures 4.4 and 4.5). The strongest empirical relationship came from SWIR_D1 at 2204 nm (R = 0.660, R^2 = 0.440, N = 104; Table 4.2), which is also the single most predictive proxy of any clay mineral in the study. The Al–OH feature-depth metric was positive but much weaker (R = 0.440, R^2 = 0.200; Table 4.4), confirming that the proxy sits within a real Al–OH absorption band while showing that the specific first-derivative band, not the broader feature-depth window, is the more effective predictor for kaolinite. The MINSPEC unmixing mean was weak (R ≈ 0.320; Table 4.1) and the map noisier and edge affected. PLSR gave the strongest retained clay-mineral model (R = 0.760, Pearson R^2 = 0.570, predictive R^2 score = 0.541, RMSE = 5.38; Table 4.5), and the leading rotated component reproduced the same structure without using the reference data during fitting (SWIR_D2 RC1, R = 0.690, R^2 = 0.480; Table 4.7). Downcore, the 2204 nm proxy and the PLSR profile both reproduce the upper- and middle-core kaolinite enrichment and the decline below about 400 cm, whereas the unmixing mean follows the pattern only loosely. Kaolinite is therefore best

predicted by the SWIR_D1 2204 nm proxy or the PLSR model (Section 4.6). PCA/VPCA provides the second-best prediction, but as an untrained approach lacks the physical basis of the single band proxy.

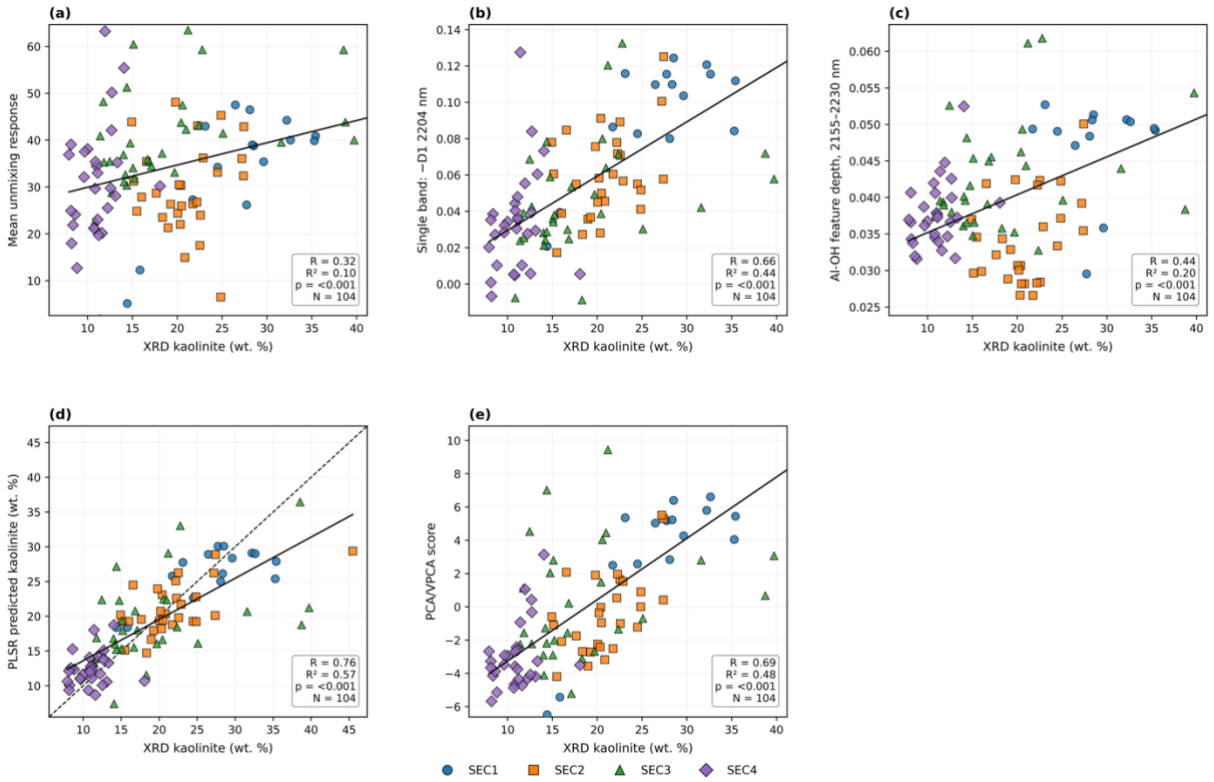

Figure 4.4. *Kaolinite-sensitive HSi products plotted against XRD kaolinite. (a) MINSPEC unmixing mean; (b) the selected SWIR_D1 2204 nm single-band proxy, plotted with reversed sign; (c) the Al–OH feature-depth metric (2155–2230 nm); (d) the depth-blocked out-of-fold PLSR prediction; and (e) the leading PCA/VPCA component score. Each panel reports the Pearson R, Pearson R², significance and number of matched samples.*

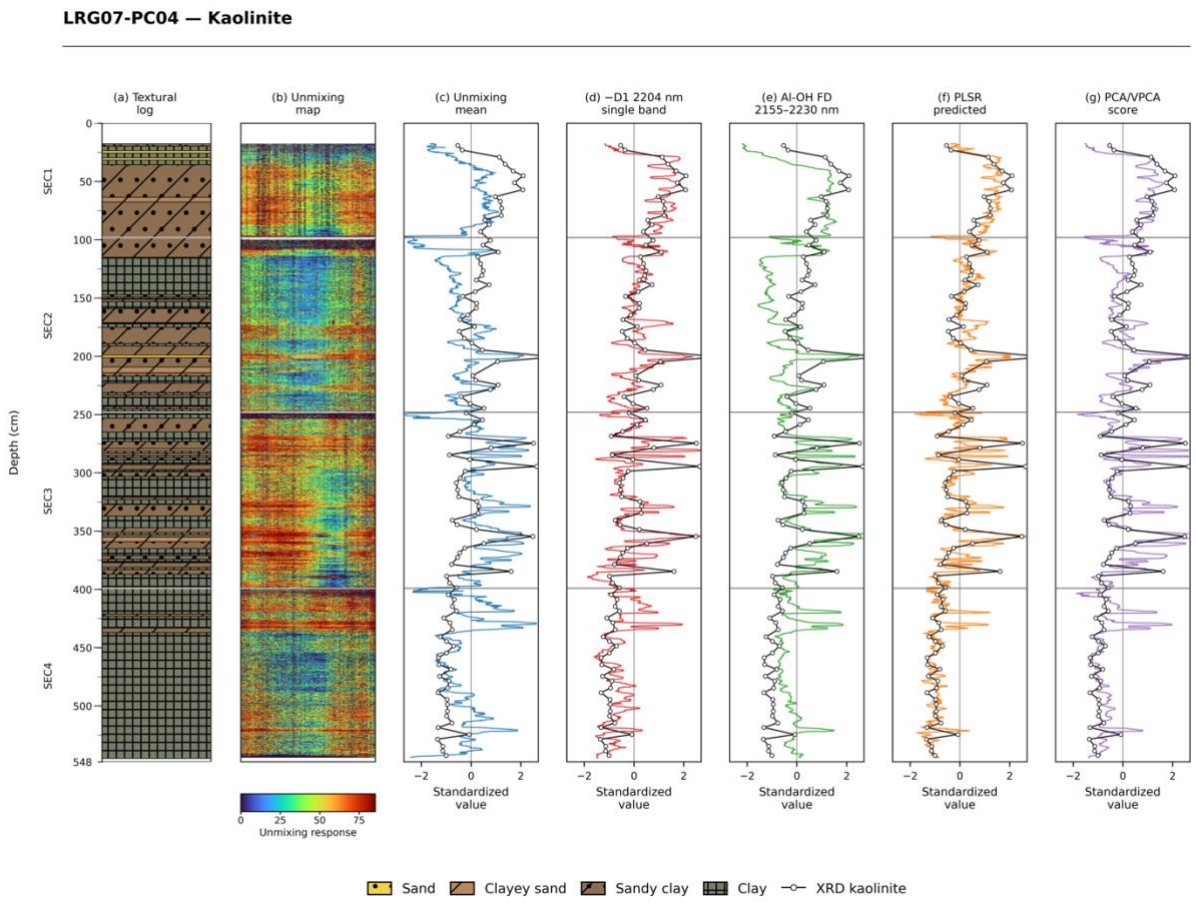

Figure 4.5. *Downcore comparison of kaolinite-sensitive HSi products for LRG07-PC04. From left to right: textural log; MINSPEC kaolinite unmixing map; line-averaged unmixing mean; the SWIR_D1 2204 nm single-band proxy, plotted with reversed sign; the Al–OH feature-depth metric (2155–2230 nm); the depth-blocked PLSR prediction; and the leading PCA/VPCA component score. The profile panels are shown as standardised values with the XRD kaolinite reference overlaid. The derivative proxy and the PLSR prediction reproduce the upper- and middle-core kaolinite enrichment and the decline below about 400 cm.*

4.9.2 Illite

No usable or interpretable MINSPEC unmixing output was obtained for illite, so the corresponding panel is blank and the comparison rests on the remaining products (Figures 4.6 and 4.7). The strongest empirical relationship came from SWIR_D2 at 2195 nm ($R = 0.480$, $R^2 = 0.230$, $N = 104$; Table 4.2), within the same Al–OH region as kaolinite but capturing local second-derivative curvature; the ±6-band test showed the proxy to be locally coherent (same-sign fraction 1.00; Table 4.3). The REF Al–OH feature-depth metric related negatively to illite ($R = −0.470$, $R^2 = 0.220$; Table 4.4) and is plotted sign-reversed in Figure 4.6. The negative relationship reflects the non-specific, shared Al–OH window in which kaolinite and illite contribute to opposite directions. PLSR was retained only with caution ($R = 0.660$, Pearson $R^2 = 0.430$, predictive R^2 score = 0.216, RMSE = 5.17; Table 4.5), and the associated rotated component carried the same Al–OH signal with opposite sign (SWIR_D2 RC2, $R = −0.630$, $R^2 = 0.390$; Table 4.7). Downcore, the 2195 nm proxy captures the persistence of moderate-to-high illite through much of the middle and lower core, while the PLSR profile follows the same broad trend over a narrower predicted range. Illite is therefore resolved through the derivative Al–OH response rather

than as a MINSPEC unmixing product, with PLSR and PCA/VPCA with slightly less predictive capability.

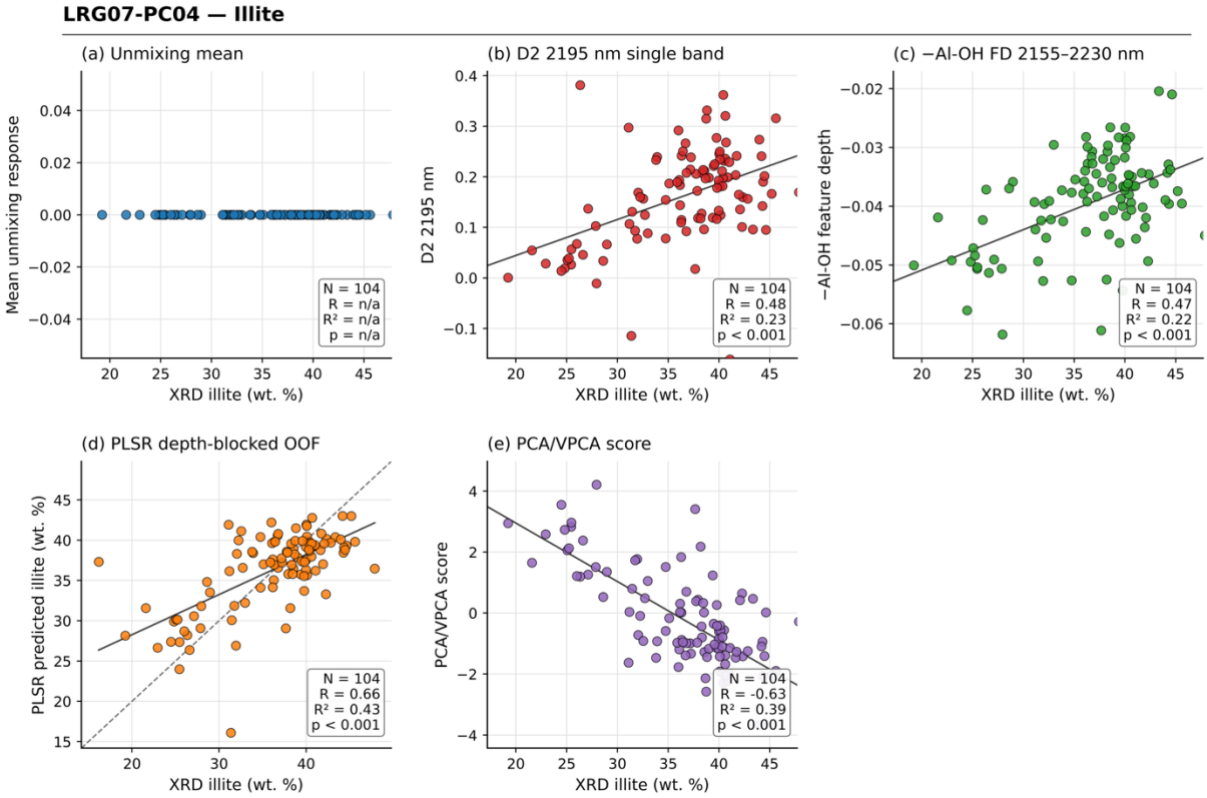

Figure 4.6. *Illite-sensitive HSi products plotted against XRD illite. (a) MINSPEC unmixing mean; (b) the selected SWIR_D2 2195 nm single-band proxy; (c) the sign-reversed Al–OH feature-depth metric (2155–2230 nm); (d) the depth-blocked out-of-fold PLSR prediction; and (e) the leading PCA/VPCA component score. No usable MINSPEC illite map was obtained, so the unmixing panel carries no interpretable signal. The second-derivative proxy gives the strongest relationship, whereas the feature-depth metric reflects a broader, non-species-specific Al–OH clay response.*

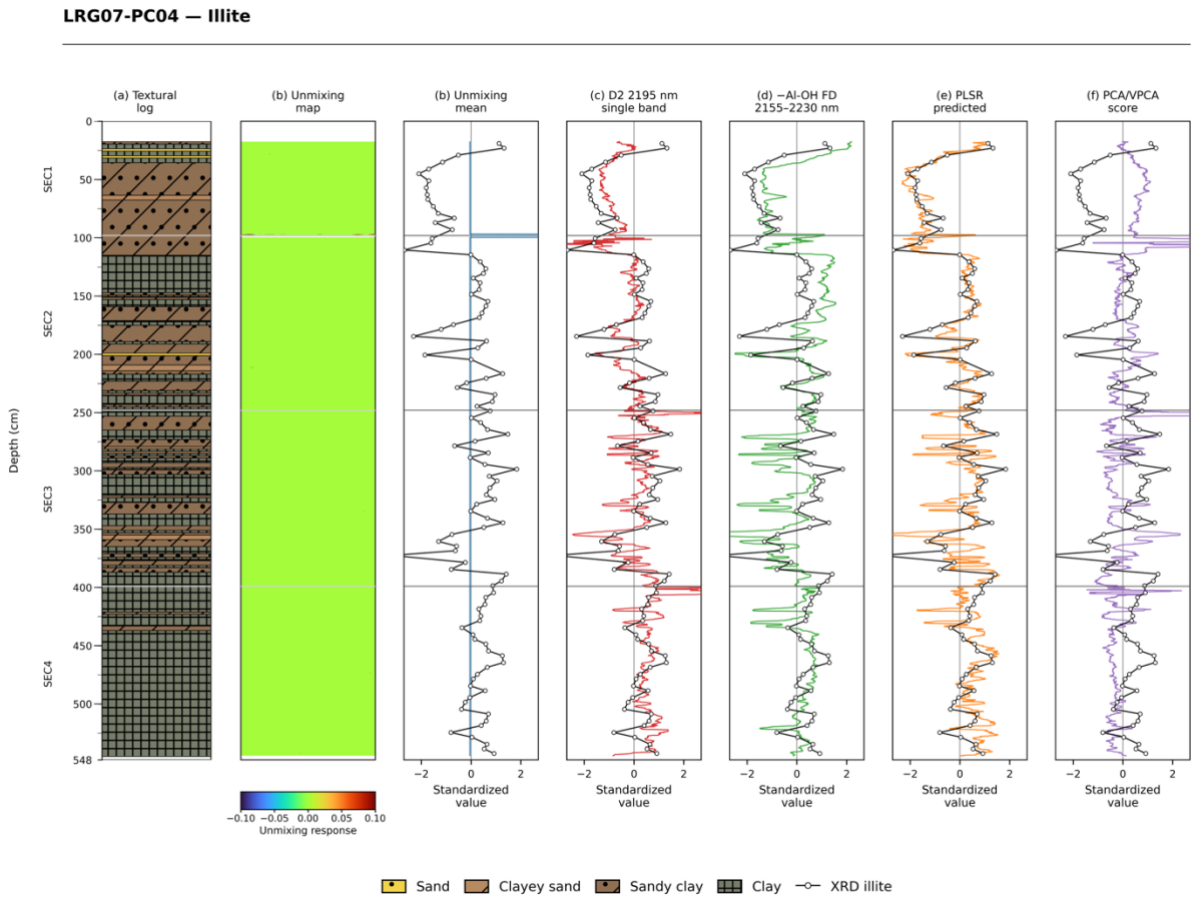

Figure 4.7. *Downcore comparison of illite-sensitive HSi products for LRG07-PC04. From left to right: textural log; MINSPEC illite unmixing map (no usable output); line-averaged unmixing mean; the SWIR_D2 2195 nm single-band proxy; the Al–OH feature-depth metric (2155–2230 nm); the depth-blocked PLSR prediction; and the leading PCA/VPCA component score. The profile panels are shown as standardised values with the XRD illite reference overlaid. Illite is resolved through the derivative Al–OH response rather than through unmixing.*

4.9.3 Chlorite

The strongest empirical relationship with XRD chlorite came from SWIR_D1 at 2278 nm in the Mg–Fe–OH region (R = 0.450, R^2 = 0.200, N = 104; Table 4.2), weaker than for kaolinite or illite (Figures 4.8 and 4.9). The ±6-band test showed the proxy to be locally coherent (same-sign fraction 1.00; Table 4.3). The REF Mg–Fe–OH feature-depth metric (2230–2290 nm) related only weakly to chlorite (R = 0.070, R^2 = 0.00; Table 4.4). The MINSPEC chlorite map shows generally low apparent contributions with sparse, patchy higher-response areas, including near the lateral split-core margins, and the unmixing mean remains low through much of the core (best D1 R = 0.31; Table 4.1). PLSR provided the weakest retained model, selected over the full SWIR range (1350–2450 nm R = 0.480, Pearson R^2 = 0.230, predictive R^2 score = 0.262, RMSE = 2.96; Table 4.5), and the rotated-component association was correspondingly weak (SWIR_D1 RC2, R = 0.430, R^2 = 0.180; Table 4.7). Downcore, the 2278 nm proxy and the PLSR profile capture part of the broad chlorite profile but follow the central tendency rather than individual excursions, which may be explained by the narrow abundance range of XRD-derived chlorite and overlap with other Mg–Fe–OH-bearing phases. Chlorite is therefore resolved only moderately, mainly through the derivative proxy and the PLSR model.

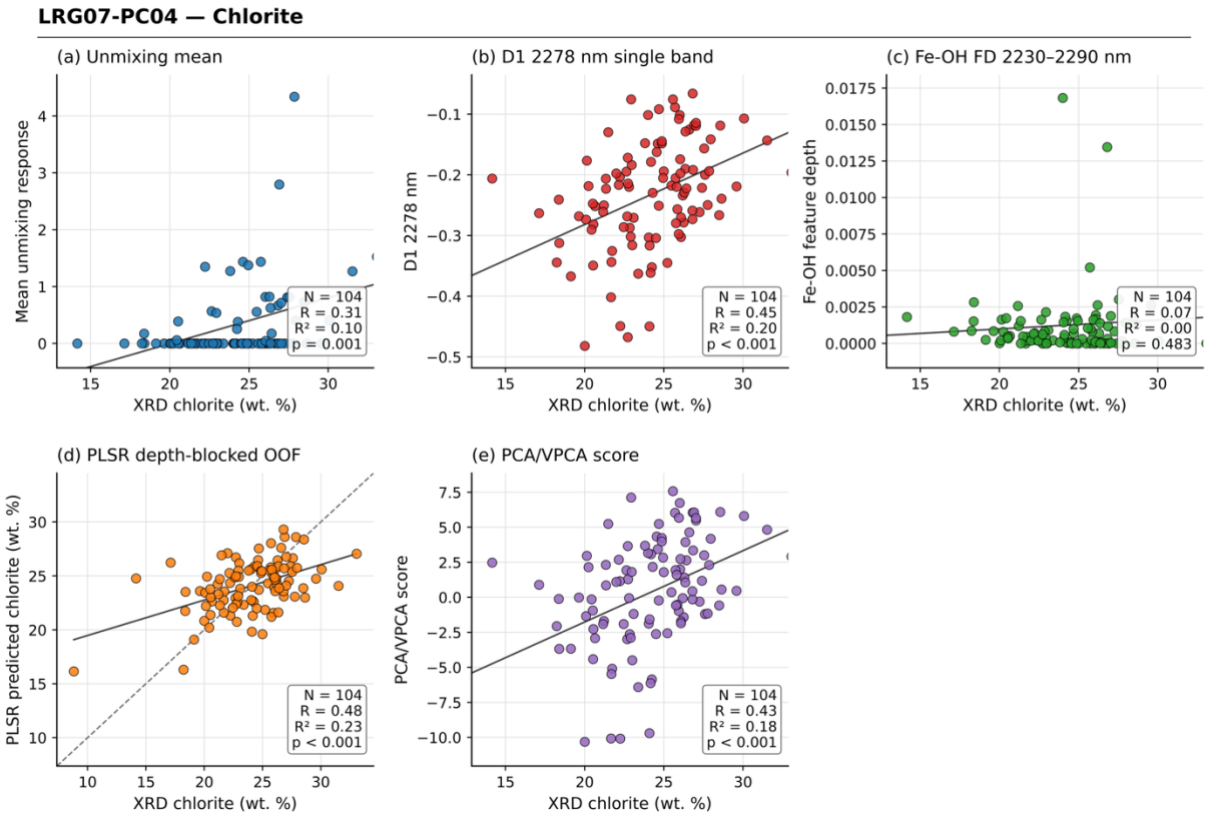

Figure 4.8. *Chlorite-sensitive HSi products plotted against XRD chlorite. (a) MINSPEC unmixing mean; (b) the selected SWIR_D1 2278 nm single-band proxy; (c) the Mg–Fe–OH feature-depth metric (2230–2290 nm); (d) the depth-blocked out-of-fold PLSR prediction; and (e) the leading PCA/VPCA component score. The derivative proxy and the full-range PLSR model give the clearest response; the feature-depth metric and the unmixing output are weak.*

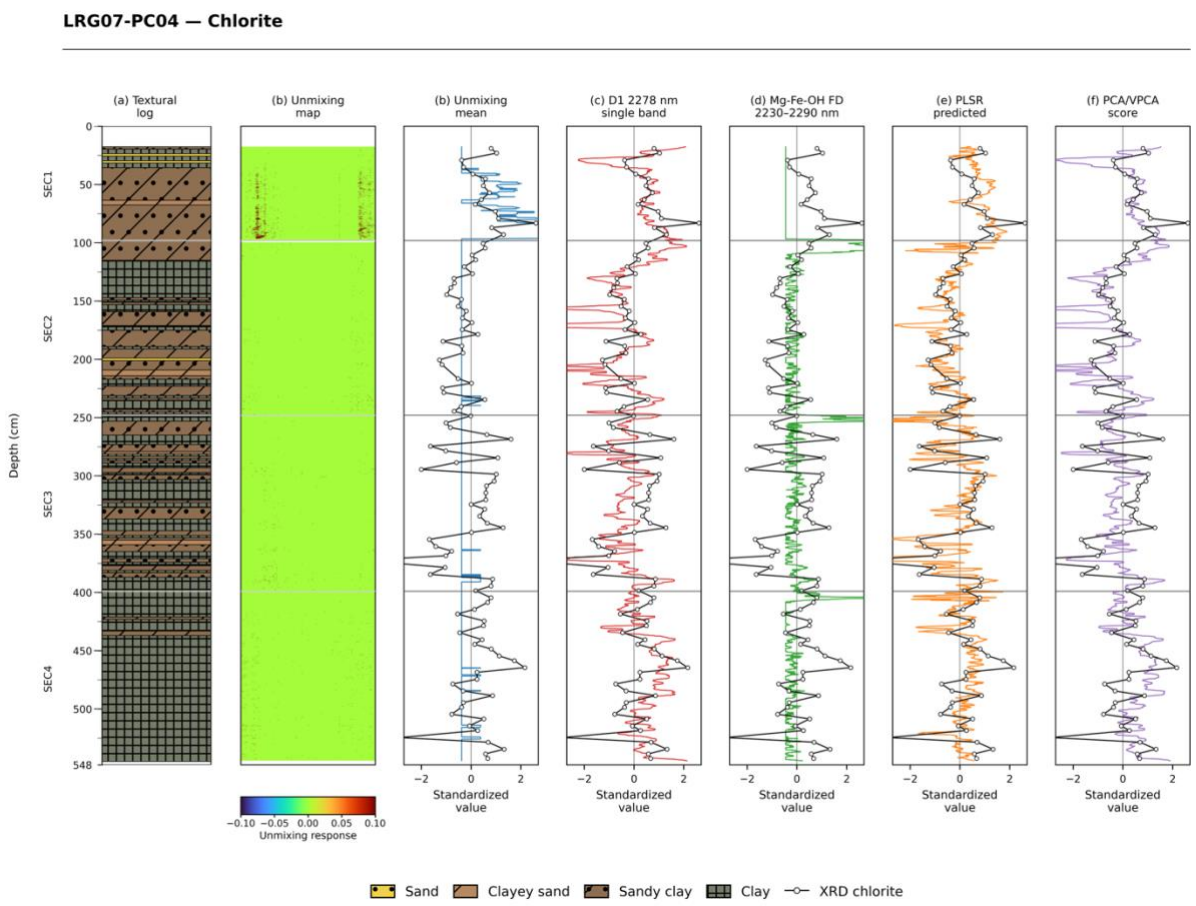

Figure 4.9. *Downcore comparison of chlorite-sensitive HSi products for LRG07-PC04. From left to right: textural log; MINSPEC chlorite unmixing map; line-averaged unmixing mean; the SWIR_D1 2278 nm single-band proxy; the Mg–Fe–OH feature-depth metric (2230–2290 nm); the depth-blocked PLSR prediction; and the leading PCA/VPCA component score. The profile panels are shown as standardised values with the XRD chlorite reference overlaid. Agreement is weaker and less direct than for kaolinite or illite.*

4.9.4 Smectite

Smectite was the weakest clay-mineral target (Figures 4.10 and 4.11). The best single-band proxy was SWIR_HQ at 1854 nm in the hydration window ($R = -0.210$, $R^2 = 0.040$, $N = 104$; Table 4.2), plotted sign-reversed. The ±6-band test showed local sign consistency but low explanatory strength (median local $R^2 = 0.024$; Table 4.3). The REF hydration feature-depth metric (1850–1960 nm) showed no meaningful agreement with XRD smectite ($R = 0.000$, $R^2 \approx 0.000$; Table 4.4). The MINSPEC smectite map shows broad spatial responses across much of the surface, with higher contributions again focused on the core margins (best D2 $R = 0.240$; Table 4.1). PLSR was tested but not retained as it produced a weak positive correlation ($R = 0.330$, Pearson $R^2 = 0.110$) but a slightly negative predictive R^2 score (-0.004, RMSE = 7.58; Table 4.5), meaning it did not predict XRD smectite better than the reference mean. The strongest rotated-component association was correspondingly weak (SWIR_D1 RC8, $R = -0.300$, $R^2 = 0.090$; Table 4.7). Downcore, none of the products reproduces the XRD smectite profile consistently.

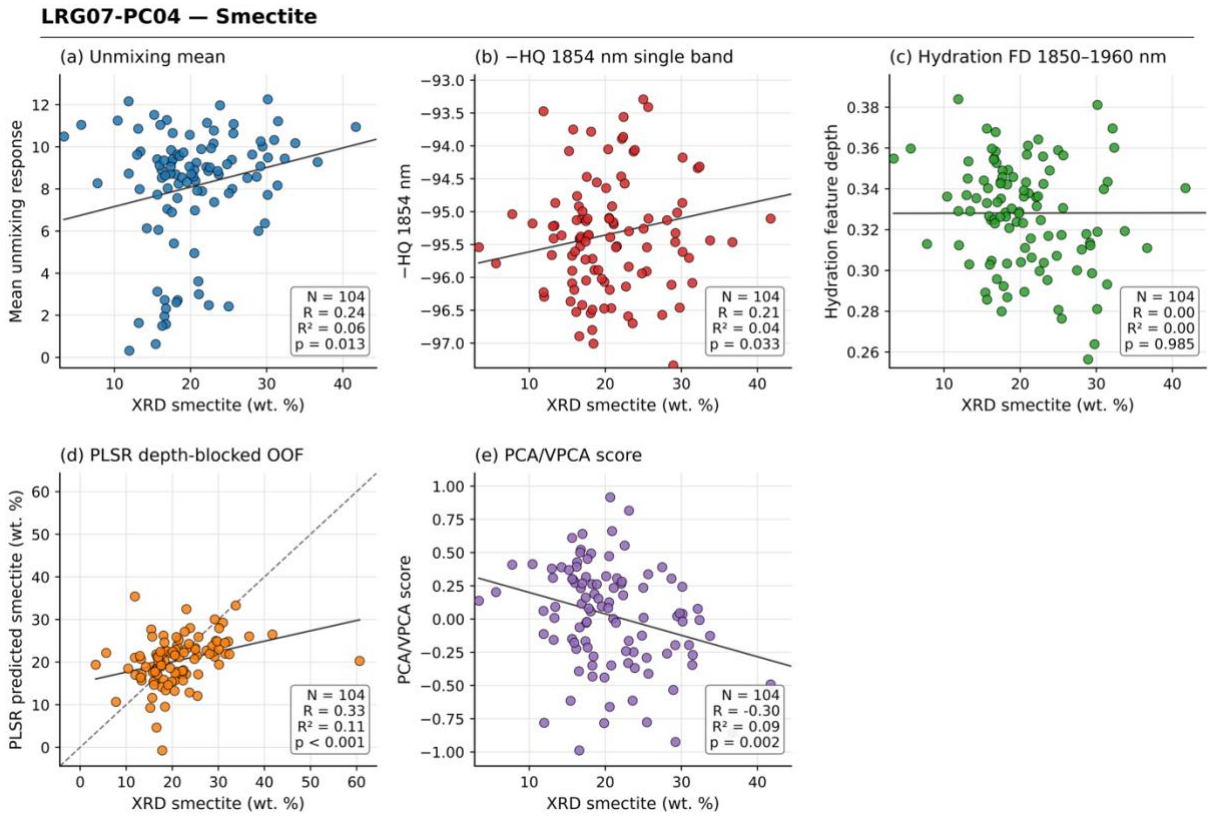

Figure 4.10. *Smectite- and hydration-sensitive HSi products plotted against XRD smectite. (a) MINSPEC unmixing mean; (b) the selected SWIR_HQ 1854 nm single-band proxy, plotted with reversed sign; (c) the hydration feature-depth metric (1850–1960 nm); (d) the depth-blocked out-of-fold PLSR prediction; and (e) the leading PCA/VPCA component score. No product provides a robust smectite relationship; the hydration window records non-specific H_2O and OH absorption rather than a smectite-diagnostic feature.*

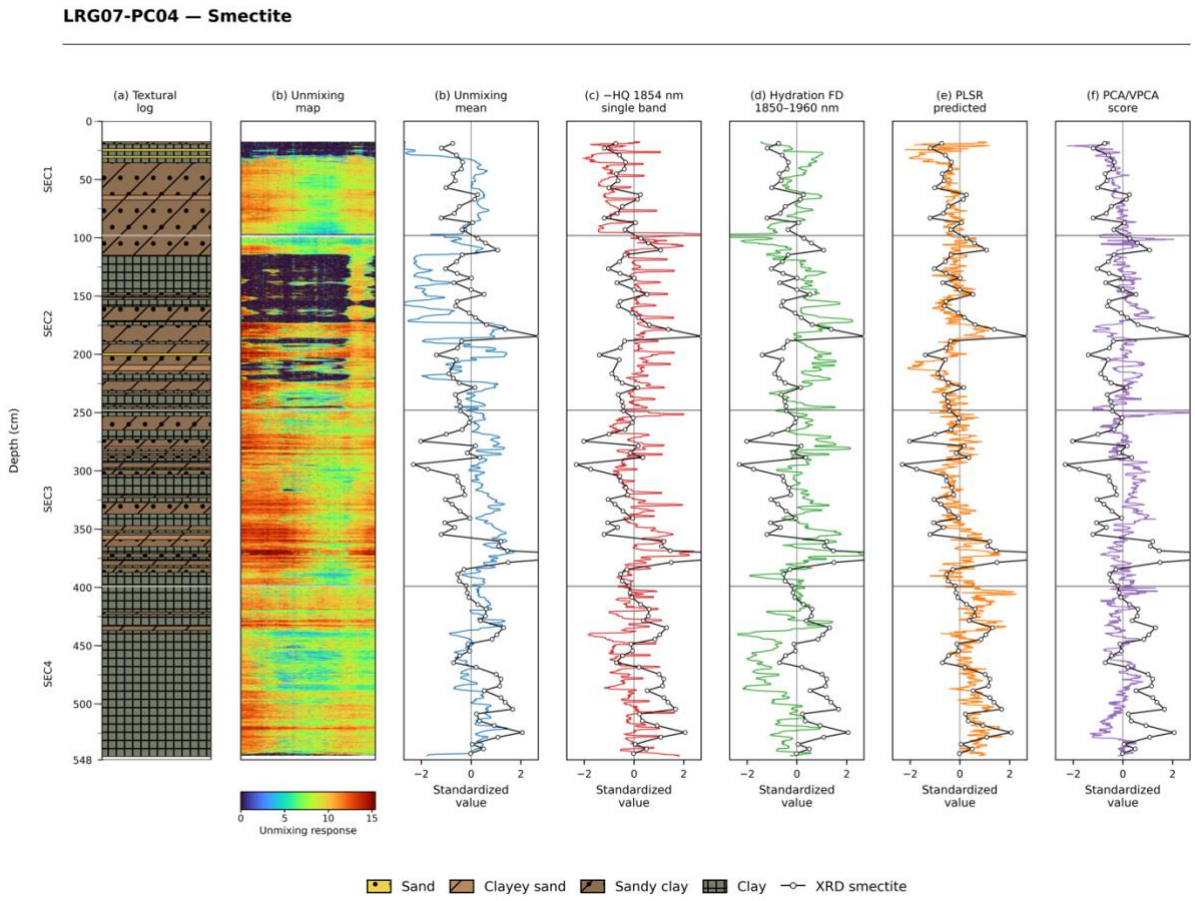

Figure 4.11. *Downcore comparison of smectite- and hydration-sensitive HSi products for LRG07-PC04. From left to right: textural log; MINSPEC smectite unmixing map; line-averaged unmixing mean; the SWIR_HQ 1854 nm single-band proxy, plotted with reversed sign; the hydration feature-depth metric (1850–1960 nm); the depth-blocked PLSR prediction; and the leading PCA/VPCA component score. The profile panels are shown as standardised values with the XRD smectite reference overlaid. None of the products reproduces the XRD smectite profile consistently.*

4.9.5 Carbonate/Ca

The strongest empirical relationship with XRF Ca came from SWIR_D2 at 2330 nm in the carbonate-sensitive region ($R = 0.570$, $R^2 = 0.320$, $N = 1051$; Table 4.2; Figures 4.12 and 4.13). The ±6-band test showed the proxy to be narrow and derivative-sensitive rather than broadly stable (same-sign fraction 0.850; Table 4.3). The REF feature-depth metric (2310–2360 nm) was weak against XRF Ca ($R = 0.110$, $R^2 = 0.010$; Table 4.4). The MINSPEC carbonate map shows generally low, diffuse apparent contributions, and the unmixing mean captures some broad upper- and middle-core variability without the full amplitude of XRF Ca (Table 4.1). The rotated component associated with Ca gave the strongest association in the study (SWIR_D2 RC6, $R = 0.760$, $R^2 = 0.570$; Table 4.7), recovering the same Ca structure from unsupervised decomposition alone. No PLSR model was fitted for Ca because the PLSR calibration was restricted to the four XRD clay minerals (Section 3.9), so no PLSR panel is shown. Downcore, the 2330 nm proxy captures the contrast between the Ca-enriched upper and middle core and the Ca-poor lower core (below about 250 cm) more closely than either the unmixing mean or the feature-depth metric.

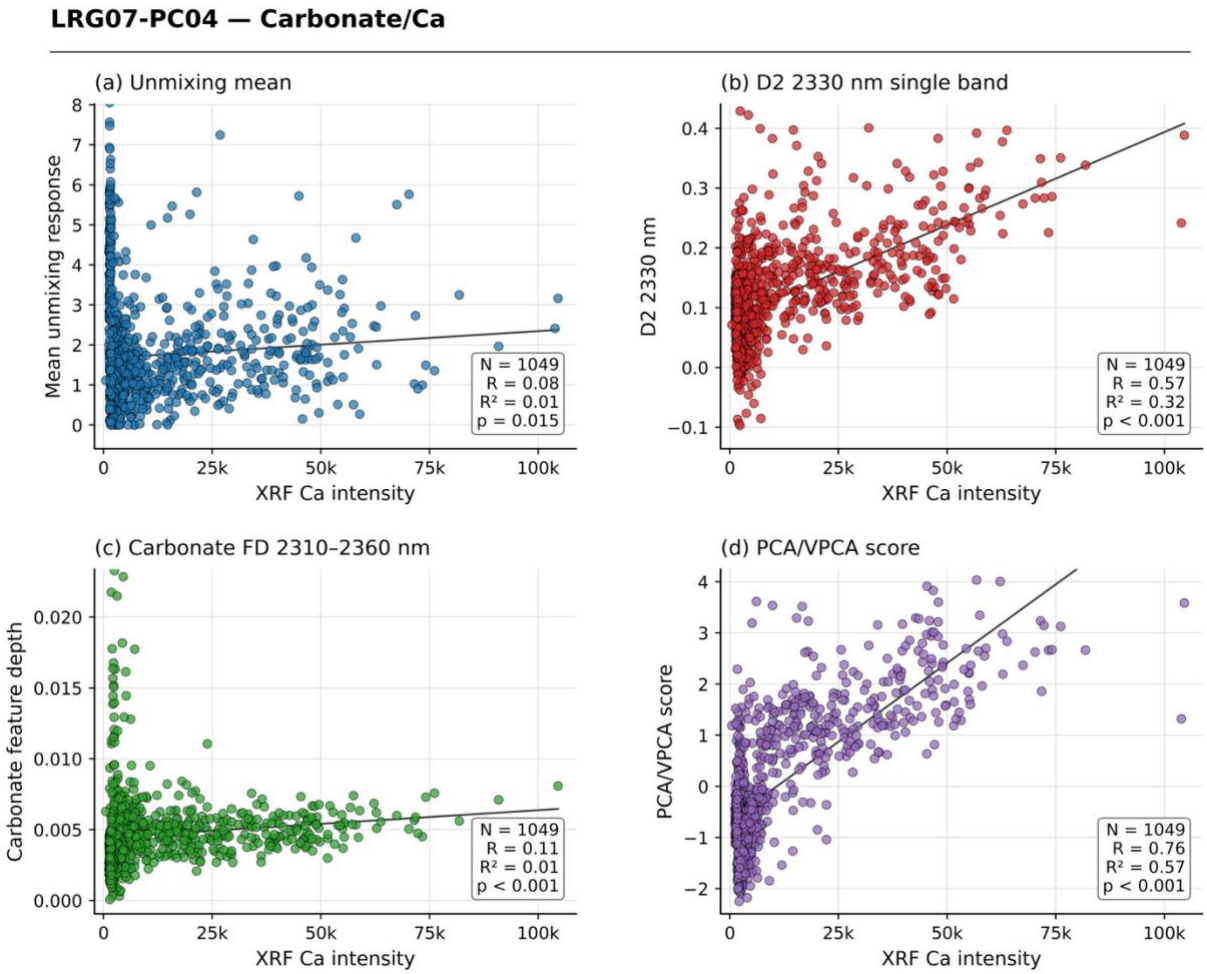

Figure 4.12. *Carbonate/Ca-sensitive HSi products plotted against XRF Ca intensity. (a) MINSPEC unmixing mean; (b) the selected SWIR_D2 2330 nm single-band proxy; (c) the carbonate feature-depth metric (2310–2360 nm); and (d) the leading PCA/VPCA component score. The leading PCA/VPCA component score shows the strongest relationship. The HSi products are Ca-sensitive spectral indicators, not quantitative carbonate-abundance estimates.*

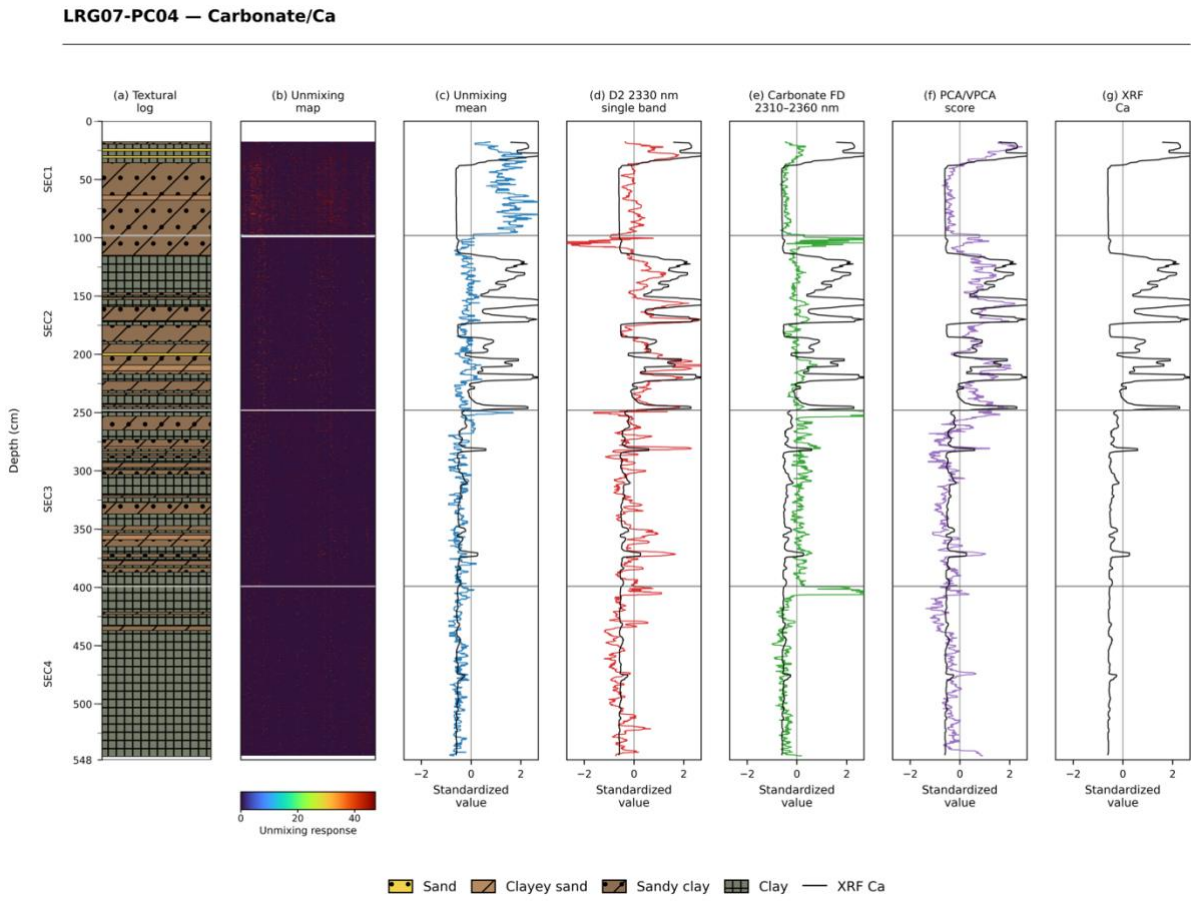

Figure 4.13. *Downcore comparison of carbonate/Ca-sensitive HSi products for LRG07-PC04. From left to right: textural log; MINSPEC carbonate unmixing map; line-averaged unmixing mean; the SWIR_D2 2330 nm single-band proxy; the carbonate feature-depth metric (2310–2360 nm); the leading PCA/VPCA component score; and the XRF Ca reference profile. The 2330 nm proxy captures the contrast between the Ca-enriched upper and middle core and the Ca-poor lower core more closely than the unmixing or feature-depth products.*

4.9.6 Fe-oxide/Fe

The strongest empirical relationship with XRF Fe came from VNIR_D1 at 919.6 nm ($R = -0.600$, $R^2 = 0.360$, $N = 1051$; Table 4.2; Figures 4.14 and 4.15), plotted with reversed sign. The negative correlation reflects the sign convention of the first-derivative response in the Fe-sensitive VNIR region, not an inverse mineralogical relationship. The ±6-band test showed the proxy to be locally stable (same-sign fraction 1.00; Table 4.3). The REF feature-depth metric (850–950 nm) was weaker against XRF Fe ($R = 0.320$, $R^2 = 0.100$; Table 4.4). The MINSPEC Fe-oxide map is more visually structured than the SWIR clay maps, with pronounced banding, and gave the strongest unmixing response of any target (best D1 $R = 0.430$; Table 4.1), although its line-averaged profile does not match XRF Fe at all depths. Fe is associated with the same rotated SWIR_D2 component that carries Ca but with opposite sign (RC6, $R = -0.700$, $R^2 = 0.490$; Table 4.7), so Ca and Fe are expressed jointly as a single contrasting spectral mode rather than as independent mineral predictions. Similar to Ca, no PLSR model was fitted (Section 3.9). Downcore, XRF Fe remains high and variable through much of the core and, unlike Ca, does not decrease sharply below the middle core; the sign-reversed 919.6 nm proxy reproduces part of this broad structure, with local mismatches at individual depths.

Several of the more strongly Fe-enriched intervals in the lower core coincide with dark brown, fine-grained sediment, and it is worth noting that such intervals in central Arctic cores are often also Mn-enriched and associated with interglacial deposition (Löwemark et al., 2014). The XRF Mn record here shows some covariation with Fe in these intervals, so at least part of the high Fe response, and the banded appearance of the MINSPEC Fe map, may reflect Fe–Mn-oxide-bearing horizons. The best HSi expression of Fe variability was the empirical derivative proxy.

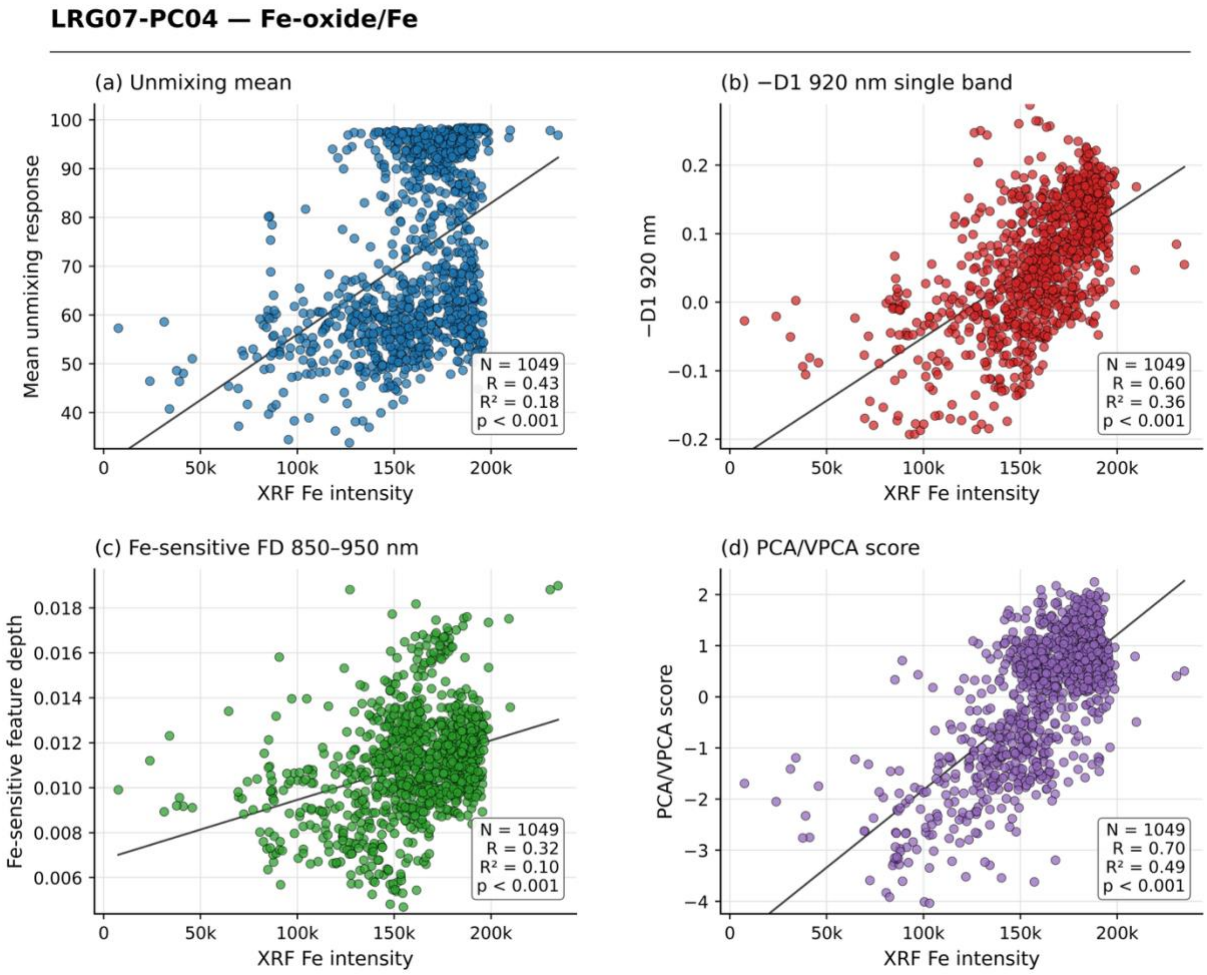

Figure 4.14. *Fe-sensitive HSi products plotted against XRF Fe intensity. (a) MINSPEC unmixing mean; (b) the selected VNIR_D1 919.6 nm single-band proxy, plotted with reversed sign; (c) the Fe-sensitive feature-depth metric (850–950 nm); and (d) the leading PCA/VPCA component score. The first-derivative proxy shows the strongest relationship. The HSi products are Fe-sensitive spectral indicators, not quantitative Fe-oxide or total-Fe measurements.*

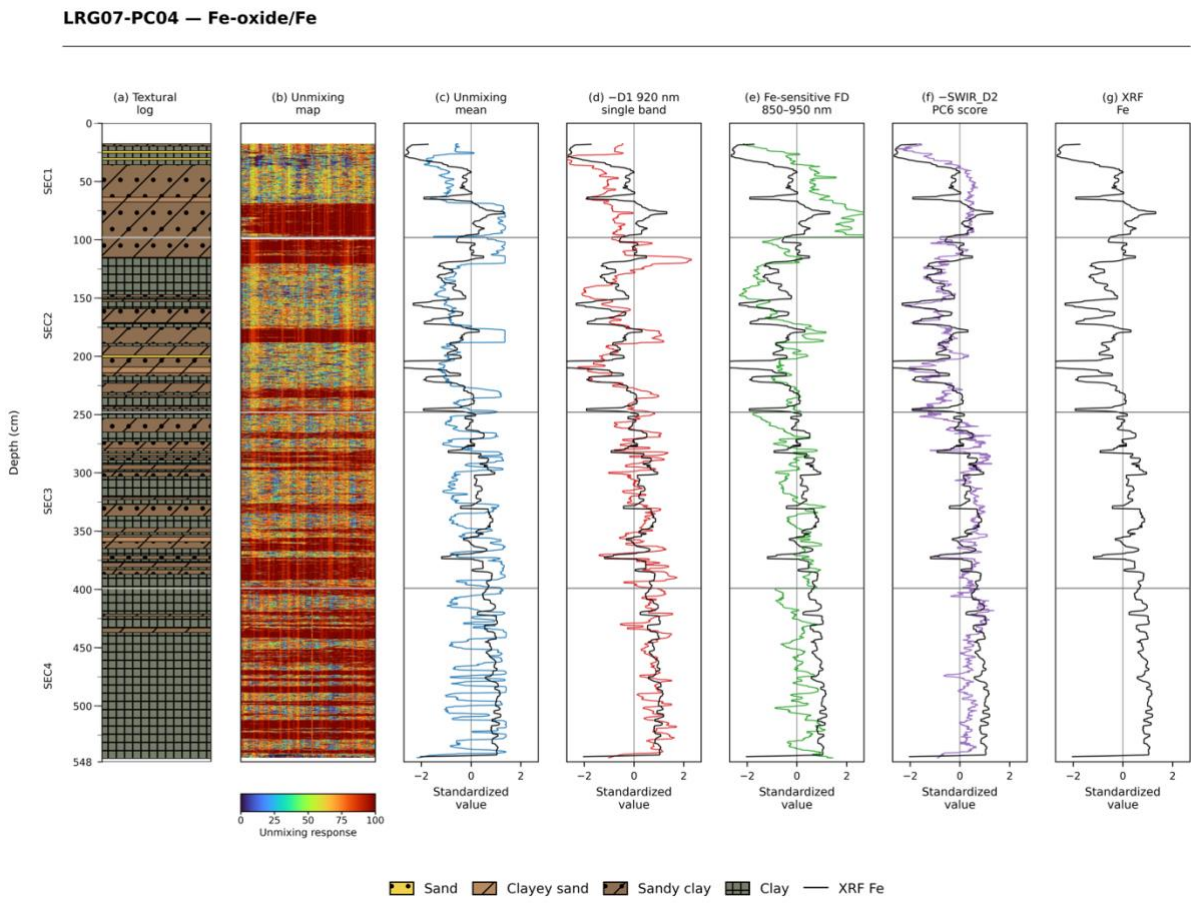

Figure 4.15. *Downcore comparison of Fe-sensitive HSi products for LRG07-PC04. From left to right: textural log; MINSPEC Fe-oxide unmixing map; line-averaged unmixing mean; the VNIR_D1 919.6 nm single-band proxy, plotted with reversed sign; the Fe-sensitive feature-depth metric (850–950 nm); the leading PCA/VPCA component score; and the XRF Fe reference profile. The sign-reversed derivative proxy reproduces part of the broad downcore Fe structure, with local mismatches at individual depths.*

4.10 Integrated target-wise comparison

Read across all approaches, the targets fall into a clear and consistent order, and the comparison reveals that different analysis approaches provide the preferred method for individual targets (Table 4.9). Kaolinite is recovered by every method and is best predicted by the SWIR_D1 2204 nm proxy or the PLSR model. Illite and chlorite are recovered with caution, illite through the SWIR_D2 2195 nm derivative proxy and chlorite through PLSR, with no useful MINSPEC unmixing-map for either. Carbonate/Ca and Fe are best recovered as empirical geochemical indicators through their derivative proxies (SWIR_D2 2330 nm and VNIR_D1 919.6 nm). Smectite is the consistent negative result and is not recoverable by any method. Overall, empirical derivative proxies and PLSR are the most effective methods.

Target	Best product to use	Confidence	MINSPEC map useful?
Kaolinite	SWIR_D1 2204 nm proxy / PLSR (SWIR_D2)	High	Only weakly
Illite	SWIR_D2 2195 nm derivative proxy	Moderate	No
Chlorite	PLSR (full SWIR)	Moderate–low	No
Carbonate/Ca	SWIR_D2 2330 nm proxy (indicator)	Moderate (indicator)	No
Fe	VNIR_D1 919.6 nm proxy (indicator)	Moderate (indicator)	Partly
Smectite	None — negative result	—	No

Table 4.9. *Target-wise summary of the single best HSi product for each mineral and element, the confidence in it, and whether the MINSPEC unmixing map adds anything. The table summarises the practical outcome of the comparison: derivative proxies and PLSR account for most of the recoverable signal, and only kaolinite, and partly Fe, is served by unmixing.*

5. Discussion

This chapter investigates why the HSi workflow behaved differently across mineral and geochemical targets, and what those differences imply for the use of VNIR–SWIR core scanning in Arctic marine sediment. The central argument is that HSi is reliable when the right product is chosen for each target and needs to be validated against reference data.

5.1 Why MINSPEC unmixing underperformed the empirical proxies

MINSPEC unmixing generally produced poor mineral-sensitive maps and did not reproduce the XRD and XRF reference variability as strongly as targeted band screening (Tables 4.1, 4.2). The most likely reasons are intrinsic to library-based unmixing of fine-grained marine mud rather than failures of the software. Linear unmixing represents each measured spectrum as a weighted combination of reference endmembers (Adams et al., 1986; Keshava and Mustard, 2002; Bioucas-Dias et al., 2012), which assumes the sediment surface behaves as an approximately linear mixture of spectrally separable components. Fine-grained marine sediment violates this assumption in two ways: A) The clay minerals share strongly overlapping Al–OH and Mg–Fe–OH absorptions and B) the sediment is a fine mixture in which scattering is non-linear, and the diagnostic features are shallow against a variable continuum controlled by colour, grain size and moisture content. Reflectance spectroscopy of pelagic sediment is reliable only when a few minerals with distinctive signatures dominate (Jarrard and Vanden Berg, 2006). PC-04 (and other Arctic sediments) instead contains co-varying abundances of clay and bulk minerals as well as carbonate and Fe-bearing phases, which is close to or beyond the practical limit Jarrard and Vanden Berg identified for compositional spectroscopy.

Two further factors are specific to the MINSPEC unmixing implemented here. First, the internal optimisation and constraint settings were not user-controlled, so the unmixing could not be tuned to the shallow, overlapping features of this material. Second, the maps are exported on a relative 0–100 scale and are sensitive to the chosen library, diagnostic windows and spectral domain. The lateral patterning near the split-core margins (for example in the kaolinite and smectite maps) is best explained as an acquisition artefact related to surface geometry or camera configuration rather than as real cross-core mineral enrichment. The empirical single-band and PLSR proxies, by contrast, are calibrated directly against the reference data and therefore absorb part of these matrix effects into the fitted relationship, which is the main reason they outperform unmixing for most targets.

5.1.1 What controls map recoverability

The contrast between targets is best interpreted as the product of several controls acting together rather than a simple ranking of mineral abundance (Table 4.8). Recoverability was high only where a target combined an adequate reference dynamic range, a feature-specific and accessible absorption, and a consistent feature–reference relationship. Kaolinite met all three conditions and was recoverable as a relative diagnostic map. Illite failed despite adequate reference variability because its Al–OH feature is shared with kaolinite and relates to the reference variable with opposite sign, so library unmixing could not separate the two endmembers. Chlorite failed on two counts, a narrow XRD range and weak feature–reference agreement. Smectite failed because its screening window records non-specific hydration rather than a smectite-diagnostic feature. Carbonate/Ca and Fe are limited by the reference variable itself where XRF Ca and Fe are elemental and integrate several phases, so even a coherent spectral mode maps to a geochemical contrast rather than to mineral abundance. These different controls can explain why the same workflow produces a usable map for one clay mineral and none for another.

5.2 Why empirical derivative bands often outperformed unmixing and feature depth

For most targets the strongest HSi–reference relationship came from a single derivative or hull-quotient-normalised band rather than from unmixing or reflectance feature depth (Table 4.2). Taking the derivative of a spectrum removes the broad, slowly changing background caused by colour, grain size and brightness, and leaves the sharp local bends that mark a narrow absorption (Tsai and Philpot, 1998). Because the useful clay and carbonate signals in this core are shallow and sit on a strong, variable background, a method that strips that background away works better than one, such as feature depth or library unmixing, that has to model it. The use of VNIR derivative spectroscopy to extract lithological and provenance information from Arctic sediment is well established (Ortiz, 2011), and the present results extend the same idea into the SWIR clay region.

Feature depth measures absorption strength against a fitted local continuum across a fixed window (Section 3.8). It is physically interpretable but more exposed to continuum errors and to blending of neighbouring features. The Al–OH window behaved coherently and gave interpretable, opposite-sign kaolinite and illite relationships (Table 4.4), but the chlorite, carbonate, Fe and smectite windows were weak even where the corresponding derivative band was moderately strong. The useful signals in PC-04 are therefore carried more by local spectral shape than by broad, cleanly resolved troughs, which favours derivative screening over feature depth for this material.

5.3 Clay minerals: kaolinite, illite and chlorite

Kaolinite is the best-constrained clay-mineral target across every method. It produced the strongest single-band proxy (SWIR_D1 2204 nm, $R = 0.660$, $R^2 = 0.440$), the strongest PLSR model (SWIR_D2, R^2 score 0.541) and a clear PCA/VPCA expression (SWIR_D2 RC1, $R = 0.692$). Two factors can explain this 1) kaolinite has a comparatively distinctive Al–OH absorption near 2160–2195 nm, 2) it shows real downcore abundance variation in PC-04, with marked upper- and middle-core enrichment and lower values below about 400 cm, so there is a wide reference range for the calibration to resolve.

Illite is resolved by a derivative Al–OH response rather than through unmixing. No usable MINSPEC illite map was obtained, yet the SWIR_D2 2195 nm proxy is locally stable, and the PLSR model is retained with caution (R^2 score 0.329, $p < 0.001$). Illite is captured by derivatives but not by unmixing because illite and kaolinite occupy the same Al–OH region and vary in opposite directions within the closed XRD composition. Library unmixing struggles to separate two endmembers competing for the

same shallow feature, whereas a second-derivative band captures local curvature, while a multi-band PLSR model can exploit the systematic difference in feature shape. The opposite-sign kaolinite and illite relationships in the shared Al–OH feature-depth window and in the PCA/VPCA rotated components are the direct expression of this shared-region, closed-composition behaviour and should be read as a clay-OH contrast rather than two independent signals.

Chlorite is only moderately resolved. Its best proxy (SWIR_D1 2278 nm, R = 0.450) is locally stable but weaker than kaolinite or illite, its reflectance feature depth is effectively absent (R^2 = 0.000), and its retained PLSR model required the full SWIR range rather than a narrow diagnostic window. The full-range selection is itself diagnostic as chlorite prediction here is driven not by one clean absorption but by a distributed, lower-amplitude response. This is consistent with chlorite's narrow XRD range in PC-04 (mostly 20–28%), which gives the calibration little contrast, and with the overlap of the chlorite Mg–Fe–OH feature with other Mg- and Fe-bearing phases.

5.4 Why smectite remained weak across every method

Smectite is the clearest negative result of the thesis. It was the weakest single-band proxy (SWIR_HQ 1854 nm, R^2 = 0.062), showed no diagnostic hydration feature depth ($R^2 \approx 0.000$), was not retained by PLSR (R^2 score −0.004), and had no robust PCA/VPCA expression (best component R = −0.300). Because the failure is reproduced by four independent approaches, it is unlikely to be an artefact of any one method. It reflects limited smectite-specific spectral predictability in this dataset rather than an analytical mistake.

This outcome deserves comment against the literature, because smectite is in principle a spectrally distinctive clay. In dry, relatively pure samples it has diagnostic H_2O and Al–OH features and is routinely identified by reflectance spectroscopy. The reason it is resolvable in the literature but not here is the combination of a wet, mixed matrix and a non-specific screening window. Smectite was screened mainly through the 1850–1960 nm hydration window, but that region records H_2O and OH absorption from bound water, surface moisture and several hydrated or hydroxyl-bearing components, not smectite alone. Reflectance spectroscopy of moist sediment is specifically degraded by pore and surface water (Jarrard and Vanden Berg, 2006). Smectite's diagnostic Al–OH feature near 2200 nm also overlaps the kaolinite–illite region, leaving no clean, smectite-specific window in this material. The residual-smectite closure test recovered slightly more variance (R^2 score 0.209) than the direct model, but that improvement is expected from error redistribution among the other three predicted components and is not an independent smectite signal. Documenting smectite as a tested, non-retained target is therefore more defensible than omitting it, and it marks a concrete boundary of the method for this core. Under moist, mixed-mineral conditions, VNIR–SWIR HSi does not recover expandable-clay content, even though smectite is resolvable in cleaner, dry sediment mixtures.

5.5 Carbonate/Ca and Fe as empirical geochemical indicators

The carbonate/Ca and Fe responses are best understood as empirical geochemical spectral indicators, not mineral-abundance estimates. On the reference side, XRF Ca and Fe are elemental intensity records, not measurements of carbonate or Fe-oxide content. In PC-04, Ca is a mixed signal of biogenic calcareous microfossils and detrital carbonate, with only part of the Ca intensity attributable to discrete microfossil tests because detrital Ca also resides in the silt and clay fraction (Hanslik et al., 2013). A proxy calibrated against Ca therefore tracks a composite geochemical quantity and cannot be promoted to a carbonate-abundance estimate. XRF intensities are further affected by water content and surface effects at the split-core surface (Tjallingii et al., 2007; Weltje and Tjallingii, 2008), adding scatter independent of the spectroscopy.

On the spectral side, the carbonate/Ca proxy (SWIR_D2 2330 nm, R = 0.570) sits near the CO_3 absorption region and tracks the upper–middle-core Ca enrichment more faithfully than either unmixing or feature depth, but it is locally narrow and derivative-sensitive, so it is a tracer of Ca-related variability rather than a carbonate measurement. The Fe proxy (VNIR_D1 919.6 nm, R = −0.600) lies in the Fe^{3+} electronic-transition region (Hunt, 1977) and is locally stable, but VNIR Fe-related reflectance is influenced by sediment colour, oxidation state, grain size, organic matter and moisture, so it integrates several Fe-bearing phases.

It is worth checking whether Ca and Fe really are out of phase in this core, because a single rotated SWIR_D2 component captures them with opposite sign (Ca R = 0.760; Fe R = −0.700; Table 4.7). Downcore, the two are broadly antiphased. Ca is enriched in the upper and middle core and falls sharply below about 250 cm, whereas Fe stays high and variable in the lower core. This is a real covariation in the data rather than an artefact of the rotation. The relationship is not perfectly reciprocal, however, and the Mn record adds an important qualification. Where Fe is high in the darker, fine-grained lower-core intervals, Mn tends to be enriched as well, and such Fe–Mn-enriched, foraminifera-bearing intervals are commonly interglacial in central Arctic cores. If Mn, Fe and foraminiferal Ca are partly co-enriched in the same interglacial intervals, then the Ca–Fe contrast recovered by VPCA is better read as a broad lithological and redox contrast between carbonate-rich and terrigenous, Fe–Mn-oxide-bearing sediment than as a clean two-endmember antiphasing. The proxy remains a useful geochemical indicator, but this covariation is a reason not to over-interpret the single Ca–Fe mode.

Because these are geochemical rather than mineralogical products, the natural question is what a better reference would be. For carbonate specifically, bulk-mineralogy XRD, quantifying calcite and dolomite directly rather than inferring them from elemental Ca, would provide a more appropriate target than XRF Ca.

5.6 What PLSR added, and why depth-blocked validation was essential

PLSR contributed two things beyond single-band screening. It combines many overlapping bands into one calibration (Geladi and Kowalski, 1986; Wold et al., 2001), which suits hyperspectral data, and it yields continuous downcore predictions that extend the discrete XRD samples onto the HSi depth scale. For kaolinite and illite the multi-band models confirmed and slightly strengthened the single-band picture. For chlorite the model captured downcore patterns no single band expressed and for smectite the multi-band and closure variants showed that the limitation is the signal available, not the model.

This last point should not be read as the mineral information being absent from the spectra in general. For the targets that carry a usable feature, kaolinite, illite, chlorite, and the Ca and Fe indicators, the information clearly is present and is recovered well, which is exactly why the tool is promising. The PLSR organises the available signal efficiently but cannot create predictability where a target has no accessible feature or is overprinted by other physical aspects (like moisture content). This is consistent with comparative work on lake and marine sediment cores. For example, Ghanbari et al. (2020) found that inferring sediment particle size from hyperspectral data worked well when a genuine spectral response was present, and that switching among model types (PLSR, principal-component regression, support-vector regression, random forests) changed performance only at the margins. In other words, the model choice matters less than whether the target has a usable feature in the first place.

Depth-blocked cross-validation was essential component of the PLSR. Ordinary random cross-validation shuffles the samples before splitting them, so nearly identical neighboring depths end up in both the training and the test sets and the model is effectively tested on data very like what it was trained on, and this inflates the apparent skill. Depth-blocked validation holds out whole contiguous stretches of core, giving an honest out-of-fold estimate. This is illustrated by smectite where the depth-blocked

predictive R^2 score was slightly negative (−0.004) despite a weak positive correlation, meaning it did not beat a simple mean prediction once this spatial similarity was controlled. Requiring both a positive depth-blocked Pearson R and a positive predictive R^2 score is what turns that distinction into a defensible retention rule. Any HSi calibration on downcore sediment that reports only a random cross-validation correlation should be regarded as optimistic.

5.7 What the closure and residual-smectite test does and does not show

The closure test shows that four independently fitted single-target models reproduce the compositional constraint approximately but not exactly. The predicted four-mineral sum was centred near 100% (mean 99.3%) but ranged from 37.7 to 137.9% at individual depths (Table 4.6). This is the expected behaviour of independent models that were never constrained to closen. A formally correct treatment would apply a log-ratio transformation before regression (Section 3.11). The consequence is that the predicted proportions are semi-quantitative estimates, and the near-100-% mean should not be read as evidence that closure was enforced. As already discussed for smectite (Section 5.4), the residual-smectite calculation does not provide an indirect route to predicting smectite as estimating it as 100 minus the other three clay-mineral predictions accumulates their prediction error, so part of any apparent skill is propagated error. Future work should investigate whether log-transformation can improve the individual or closed-sum estimates.

5.8 What PCA/VPCA contributed

PCA and varimax-rotated PCA were used as an independent, unsupervised approach to the same targets, as they are currently widely used in VNIR reflectance spectroscopy of Arctic sediments. The key question is whether working without the reference data during fitting recovers the mineral structure better than the supervised methods, by sidestepping the calibration limitations identified above. It does not. VPCA reaches the same target ranking, kaolinite and illite as opposite-sign Al–OH modes, a strong Ca–Fe contrast in a single rotated SWIR_D2 mode, and no coherent smectite mode. The downcore comparison (Figure 4.3D) shows its leading components tracking the reference profiles about as closely as the supervised proxies, but not more closely.

5.9 Contribution to HSI in Arctic marine sediment cores

HSi core scanning has been developed most fully for lake sediments, where VNIR spectra are used for pigments, organic matter, grain size and broad minerogenic components (Jacq et al., 2022; Zander et al., 2022), and for hard-rock and drill-core logging, where absorption-feature clustering maps lithology and alteration (Rodger et al., 2021). Quantitative compositional spectroscopy of marine sediment has strong but geographically limited precedents, mainly in carbonate- and opal-rich equatorial settings (Jarrard and Vanden Berg, 2006). In the Arctic the established spectral approach has been VNIR-derivative reflectance with VPCA for provenance rather than SWIR clay-mineral calibration (Ortiz, 2011). Arctic marine sediment-core clay mineralogy by VNIR–SWIR HSi, validated against XRD and XRF, has not previously been a developed application.

The contribution here is therefore methodological. It establishes, for a real central-Arctic core, a VNIR–SWIR workflow can predict kaolinite robustly, illite and chlorite with caution, carbonate/Ca and Fe as empirical geochemical indicators, and smectite not at all. It also shows that empirical derivative proxies and PLSR generally outperform library unmixing for mixed terrigenous dominated fine-grained Arctic sediments.

5.10 Limitations

Several limitations bound the interpretation. A single core with 104 XRD calibration samples is not in itself a fatal constraint, but the narrow spread of clay-mineral abundances in this one core is a real constraint. With limited compositional contrast to learn from, the calibrations have little dynamic range, and chlorite in particular suffers from a very small XRD range. A wider reference dataset, spanning more central-Arctic cores and a broader range of clay-mineral compositions, is the single most important requirement for improving the PLSR predictions, and this need is itself one of the main results of the thesis.

Another limitation is that the reference targets are themselves indirect. XRD clay proportions are closed relative fractions, and XRF Ca and Fe are elemental intensities, so even a perfect spectral proxy would track a composite quantity. For carbonate, bulk-mineralogy XRD (direct calcite and dolomite) would be a stronger reference than elemental Ca and could include further mineral components (beyond the clay minerals) that would influence any single spectral signal.

The clay-mineral models were fitted independently without a log-ratio transformation, so closure is only approximate (Section 5.7). Surface effects, including moisture, roughness, curvature, illumination geometry and grain size, affect reflectance and are hard to separate from composition. They degrade the hydration region most severely, which is a likely reason for the poor smectite predictions. Moisture is a particular difficulty because the relevant quantity is the water content at the moment of scanning, which changes quickly as the split surface dries under the heat of the lamp. The same interval can therefore present a different hydration signal at the start and end of a scan, which is very hard to correct after the fact. Finally, MINSPEC unmixing was run with internal settings that could not be tuned to this material, so its weak performance is specific to this out-of-the-box configuration rather than a general verdict on unmixing.

5.11 Future work

The clearest priority is a larger training and calibration dataset rather than further testing of the existing calibrations on PC04. Assembling matched HSi and XRD data across several central-Arctic cores, spanning a wider range of clay-mineral compositions, would provide the compositional contrast the single-core calibration lacks and would directly test whether the kaolinite, illite and chlorite models transfer or must be refitted locally.

A natural question is which method that larger effort should focus on. The present results suggest that no single fixed proxy is the answer, because each mineral is best predicted in a different spectral domain. A supervised model that can take these different domain representations as inputs and learn a single predictive workflow is therefore well suited to the problem. In practice these points toward PLSR as the baseline and, with enough calibration data, toward more flexible machine-learning models (for example support-vector regression or random forests) that can combine the reflectance, derivative and hull-quotient forms of the spectra into one prediction per mineral.

6. Conclusion

This thesis evaluated to what extent VNIR–SWIR hyperspectral core scanning can identify and interpret downcore mineralogical and geochemical variability in an Arctic marine sediment core. It compared different HSi processing approaches against XRF and clay-mineral XRD reference data in order to establish which approach is the best one to take forward.

The clearest result is that recoverability differs sharply among mineral targets but is consistent across methods. Kaolinite is robustly recovered, giving the strongest single-band proxy, the strongest retained PLSR model and a clear PCA/VPCA expression. Illite and chlorite are recovered with caution, illite mainly as a derivative Al–OH response and a cautiously retained PLSR model, with no usable MINSPEC unmixing map, and chlorite only moderately, through a locally stable derivative proxy and a full-range PLSR model. Carbonate/Ca and Fe are recovered as empirical geochemical indicators rather than mineral-abundance estimates, expressed most clearly through derivative proxies and, jointly, through a strong rotated PCA/VPCA mode. Smectite is not robustly recovered by any method likely due to interferences from water content and other hydrated minerals.

Empirical derivative and hull-quotient proxies and, above all, PLSR, are the most promising approaches for future work. MINSPEC library unmixing and reflectance feature depth added little for this fine-grained, spectrally overlapping material, and PCA/VPCA reproduced the supervised ranking as an independent confirmation rather than as a better predictor.

The main obstacle to going further is not the method but the data available to calibrate it. The predictions here are limited by a single core with a narrow spread of clay-mineral abundances. Future work should aim at building a broader Arctic training dataset with greater compositional variability and extend the reference data toward bulk mineralogy so that carbonate and other phases can be calibrated directly. PLSR, or with enough calibration data, a more flexible machine-learning model that takes the different spectral-domain representations of each mineral as inputs, has the potential to build a predictive tool applicable to Arctic Ocean sediments that are dominated by terrigenous components. On that basis, VNIR–SWIR hyperspectral core scanning has clear potential to turn discrete mineralogical and geochemical measurements into continuous, high-resolution downcore records in Arctic marine sediments

References

Aagaard, K. and Carmack, E.C., 1989. The role of sea ice and other fresh water in the Arctic circulation. Journal of Geophysical Research, 94(C10), 14485–14498. https://doi.org/10.1029/JC094iC10p14485

Adams, J.B., Smith, M.O. and Johnson, P.E., 1986. Spectral mixture modeling: a new analysis of rock and soil types at the Viking Lander 1 site. Journal of Geophysical Research, 91(B8), 8098–8112. https://doi.org/10.1029/JB091iB08p08098

Aymerich, I.F., Oliva, M., Giralt, S. and Martín-Herrero, J., 2016. Detection of tephra layers in Antarctic sediment cores with hyperspectral imaging. PLOS ONE, 11(1), e0146578. https://doi.org/10.1371/journal.pone.0146578

Bioucas-Dias, J.M., Plaza, A., Dobigeon, N., Parente, M., Du, Q., Gader, P. and Chanussot, J., 2012. Hyperspectral unmixing overview: geometrical, statistical, and sparse regression-based approaches. IEEE Journal of Selected Topics in Applied Earth Observations and Remote Sensing, 5(2), 354–379. https://doi.org/10.1109/JSTARS.2012.2194696

Bischof, J.F. and Darby, D.A., 1997. Mid- to Late Pleistocene ice drift in the western Arctic Ocean: evidence for a different circulation in the past. Science, 277(5322), 74–77. https://doi.org/10.1126/science.277.5322.74

Clark, R.N. and Roush, T.L., 1984. Reflectance spectroscopy: quantitative analysis techniques for remote sensing applications. Journal of Geophysical Research, 89(B7), 6329–6340. https://doi.org/10.1029/JB089iB07p06329

Cochran, J.R., Edwards, M.H. and Coakley, B.J., 2006. Morphology and structure of the Lomonosov Ridge, Arctic Ocean. Geochemistry, Geophysics, Geosystems, 7(5), Q05019. https://doi.org/10.1029/2005GC001114

Cronin, T.M., DeNinno, L.H., Polyak, L., Caverly, E.K., Poore, R.Z., Brenner, A.R., Rodriguez-Lazaro, J. and Marzen, R.E., 2014. Quaternary ostracode and foraminiferal biostratigraphy and paleoceanography in the western Arctic Ocean. Marine Micropaleontology, 111, 118–133. https://doi.org/10.1016/j.marmicro.2014.05.001

Croudace, I.W., Rindby, A. and Rothwell, R.G., 2006. ITRAX: description and evaluation of a new multi-function X-ray core scanner. In: Rothwell, R.G. (ed.), New Techniques in Sediment Core Analysis. Geological Society, London, Special Publications, 267, 51–63. https://doi.org/10.1144/GSL.SP.2006.267.01.04

Croudace, I.W., Löwemark, L., Tjallingii, R. and Zolitschka, B., 2019. Current perspectives on the capabilities of high resolution XRF core scanners. Quaternary International, 514, 5–15. https://doi.org/10.1016/j.quaint.2019.04.002

Darby, D.A., Bischof, J.F., Spielhagen, R.F., Marshall, S.A. and Herman, S.W., 2002. Arctic ice export events and their potential impact on global climate during the late Pleistocene. Paleoceanography, 17(2), 1025. https://doi.org/10.1029/2001PA000639

Geladi, P. and Kowalski, B.R., 1986. Partial least-squares regression: a tutorial. Analytica Chimica Acta, 185, 1–17. https://doi.org/10.1016/0003-2670(86)80028-9

Ghanbari, H., Jacques, O., Adaïmé, M.-É., Gregory-Eaves, I. and Antoniades, D., 2020. Remote sensing of lake sediment core particle size using hyperspectral image analysis. Remote Sensing, 12(23), 3850. https://doi.org/10.3390/rs12233850

Ghanbari, H. and Antoniades, D., 2022. Convolutional neural networks for mapping of lake sediment core particle size using hyperspectral imaging. International Journal of Applied Earth Observation and Geoinformation, 112, 102906. https://doi.org/10.1016/j.jag.2022.102906

Goetz, A.F.H., Vane, G., Solomon, J.E. and Rock, B.N., 1985. Imaging spectrometry for Earth remote sensing. Science, 228(4704), 1147–1153. https://doi.org/10.1126/science.228.4704.1147

Hanslik, D., Löwemark, L. and Jakobsson, M., 2013. Biogenic and detrital-rich intervals in central Arctic Ocean cores identified using X-ray fluorescence scanning. Polar Research, 32(1), 18386. https://doi.org/10.3402/polar.v32i0.18386

Henriksen, N. and Higgins, A.K., 2008. Geological research and mapping in the Caledonian orogen of East Greenland, 70°N–82°N. In: Higgins, A.K., Gilotti, J.A. and Smith, M.P. (eds.), The Greenland Caledonides: Evolution of the Northeast Margin of Laurentia. Geological Society of America Memoir 202, 1–27. https://doi.org/10.1130/2008.1202(01)

Higgins, A.K., Ineson, J.R., Peel, J.S., Surlyk, F. and Sønderholm, M., 1991. Lower Palaeozoic Franklinian Basin of North Greenland. Grønlands Geologiske Undersøgelse Bulletin, 160, 71–139. https://doi.org/10.34194/bullggu.v160.6714

Hunt, G.R., 1977. Spectral signatures of particulate minerals in the visible and near infrared. Geophysics, 42(3), 501–513. https://doi.org/10.1190/1.1440721

Jacq, K., Debret, M., Fanget, B., Coquin, D., Sabatier, P., Pignol, C., Arnaud, F. and Perrette, Y., 2022. Theoretical principles and perspectives of hyperspectral imaging applied to sediment core analysis. Quaternary, 5(2), 28. https://doi.org/10.3390/quat5020028

Jakobsson, M., Marcussen, C. and LOMROG Scientific Party, 2008. Lomonosov Ridge off Greenland 2007 (LOMROG): cruise report. Geological Survey of Denmark and Greenland, Copenhagen, 122 pp. https://doi.org/10.22008/gpub/27967

Jakobsson, M., Nilsson, J., O'Regan, M., Backman, J., Löwemark, L., Dowdeswell, J.A., Mayer, L., Polyak, L., Colleoni, F., Anderson, L.G., Björk, G., Darby, D., Eriksson, B., Hanslik, D., Hell, B., Marcussen, C., Sellén, E. and Wallin, Å., 2010. An Arctic Ocean ice shelf during MIS 6 constrained by new geophysical and geological data. Quaternary Science Reviews, 29(25–26), 3505–3517. https://doi.org/10.1016/j.quascirev.2010.03.015

Jarrard, R.D. and Vanden Berg, M.D., 2006. Sediment mineralogy based on visible and near-infrared reflectance spectroscopy. In: Rothwell, R.G. (ed.), New Techniques in Sediment Core Analysis. Geological Society, London, Special Publications, 267, 129–140. https://doi.org/10.1144/GSL.SP.2006.267.01.09

Keshava, N. and Mustard, J.F., 2002. Spectral unmixing. IEEE Signal Processing Magazine, 19(1), 44–57. https://doi.org/10.1109/79.974727

Kokaly, R.F., Clark, R.N., Swayze, G.A., Livo, K.E., Hoefen, T.M., Pearson, N.C., Wise, R.A., Benzel, W.M., Lowers, H.A., Driscoll, R.L. and Klein, A.J., 2017. USGS Spectral Library Version 7. U.S. Geological Survey Data Series 1035, 61 pp. https://doi.org/10.3133/ds1035

Kury, M.S., Ghanbari, H., Francus, P., Antoniades, D. and Homayouni, S., 2026. Estimating particle size in silty lake sediments using a fine-tuned deep learning model on hyperspectral imagery. Sedimentary Geology, 501, 107123. https://doi.org/10.1016/j.sedgeo.2026.107123

Löwemark, L., März, C., O'Regan, M. and Gyllencreutz, R., 2014. Arctic Ocean Mn-stratigraphy: genesis, synthesis and inter-basin correlation. Quaternary Science Reviews, 92, 97–111. https://doi.org/10.1016/j.quascirev.2013.11.018

Mandende, H., Ndou, C. and Mothupi, T., 2023. Hyperspectral core scanner: an effective mineral mapping tool for apatite in the Upper Zone, northern limb, Bushveld Complex. Journal of the Southern African Institute of Mining and Metallurgy, 123(2), 81–92. https://doi.org/10.17159/2411-9717/1890/2023

Myers, W.B. and Darby, D.A., 2022. A compilation of the silt and clay mineralogy from coastal and shelf regions of the Arctic Ocean. Marine Geology, 454, 106948. https://doi.org/10.1016/j.margeo.2022.106948

Ortiz, J.D., 2011. Application of visible/near infrared derivative spectroscopy to Arctic paleoceanography. IOP Conference Series: Earth and Environmental Science, 14(1), 012011. https://doi.org/10.1088/1755-1315/14/1/012011

Pedregosa, F., Varoquaux, G., Gramfort, A., Michel, V., Thirion, B., Grisel, O., Blondel, M., Prettenhofer, P., Weiss, R., Dubourg, V., Vanderplas, J., Passos, A., Cournapeau, D., Brucher, M., Perrot, M. and Duchesnay, É., 2011. Scikit-learn: machine learning in Python. Journal of Machine Learning Research, 12, 2825–2830.

Polyak, L., Bischof, J., Ortiz, J.D., Darby, D.A., Channell, J.E.T., Xuan, C., Kaufman, D.S., Løvlie, R., Schneider, D.A., Eberl, D.D., Adler, R.E. and Council, E.A., 2009. Late Quaternary stratigraphy and sedimentation patterns in the western Arctic Ocean. Global and Planetary Change, 68(1–2), 5–17. https://doi.org/10.1016/j.gloplacha.2009.03.014

Rodger, A., Fabris, A. and Laukamp, C., 2021. Feature extraction and clustering of hyperspectral drill core measurements to assess potential lithological and alteration boundaries. Minerals, 11(2), 136. https://doi.org/10.3390/min11020136

Rudels, B., Jones, E.P., Schauer, U. and Eriksson, P., 2004. Atlantic sources of the Arctic Ocean surface and halocline waters. Polar Research, 23(2), 181–208. https://doi.org/10.1111/j.1751-8369.2004.tb00007.x

Savitzky, A. and Golay, M.J.E., 1964. Smoothing and differentiation of data by simplified least squares procedures. Analytical Chemistry, 36(8), 1627–1639. https://doi.org/10.1021/ac60214a047

Swärd, H., O'Regan, M., Pearce, C., Semiletov, I., Stranne, C., Tarras, H. and Jakobsson, M., 2018. Sedimentary proxies for Pacific water inflow through the Herald Canyon, western Arctic Ocean. Arktos, 4(1), 19. https://doi.org/10.1007/s41063-018-0055-x

Swärd, H., Andersson, P., Hilton, R., Vogt, C. and O'Regan, M., 2022. Mineral and isotopic (Nd, Sr) signature of fine-grained deglacial and Holocene sediments from the Mackenzie Trough, Arctic Canada. Arctic, Antarctic, and Alpine Research, 54(1), 346–367. https://doi.org/10.1080/15230430.2022.2096425

Tjallingii, R., Röhl, U., Kölling, M. and Bickert, T., 2007. Influence of the water content on X-ray fluorescence core-scanning measurements in soft marine sediments. Geochemistry, Geophysics, Geosystems, 8(2), Q02004. https://doi.org/10.1029/2006GC001393

Tsai, F. and Philpot, W., 1998. Derivative analysis of hyperspectral data. Remote Sensing of Environment, 66(1), 41–51. https://doi.org/10.1016/S0034-4257(98)00032-7

van der Meer, F.D., van der Werff, H.M.A., van Ruitenbeek, F.J.A., Hecker, C.A., Bakker, W.H., Noomen, M.F., van der Meijde, M., Carranza, E.J.M., de Smeth, J.B. and Woldai, T., 2012. Multi- and hyperspectral geologic remote sensing: a review. International Journal of Applied Earth Observation and Geoinformation, 14(1), 112–128. https://doi.org/10.1016/j.jag.2011.08.002

Vermassen, F., O'Regan, M., de Boer, A., Schenk, F., Razmjooei, M., West, G., Cronin, T.M., Jakobsson, M. and Coxall, H.K., 2023. A seasonally ice-free Arctic Ocean during the Last Interglacial. Nature Geoscience, 16(8), 723–729. https://doi.org/10.1038/s41561-023-01227-x

Viscosi-Shirley, C., Mammone, K., Pisias, N. and Dymond, J., 2003. Clay mineralogy and multi-element chemistry of surface sediments on the Siberian-Arctic shelf: implications for sediment provenance and grain size sorting. Continental Shelf Research, 23(11–13), 1175–1200. https://doi.org/10.1016/S0278-4343(03)00091-8

Vogt, C. and Knies, J., 2009. Sediment pathways in the western Barents Sea inferred from clay mineral assemblages in surface sediments. Norwegian Journal of Geology, 89(1–2), 41–55.

Wahsner, M., Müller, C., Stein, R., Ivanov, G., Levitan, M., Shelekhova, E. and Tarasov, G., 1999. Clay-mineral distribution in surface sediments of the Eurasian Arctic Ocean and continental margin as indicator for source areas and transport pathways: a synthesis. Boreas, 28(1), 215–233. https://doi.org/10.1111/j.1502-3885.1999.tb00216.x

Weltje, G.J. and Tjallingii, R., 2008. Calibration of XRF core scanners for quantitative geochemical logging of sediment cores: theory and application. Earth and Planetary Science Letters, 274(3–4), 423–438. https://doi.org/10.1016/j.epsl.2008.07.054

Wold, S., Sjöström, M. and Eriksson, L., 2001. PLS-regression: a basic tool of chemometrics. Chemometrics and Intelligent Laboratory Systems, 58(2), 109–130. https://doi.org/10.1016/S0169-7439(01)00155-1

Zander, P.D., Wienhues, G. and Grosjean, M., 2022. Scanning hyperspectral imaging for in situ biogeochemical analysis of lake sediment cores: review of recent developments. Journal of Imaging, 8(3), 58. https://doi.org/10.3390/jimaging8030058

Appendix

No.	Mineral group	Target mineral	Library label	Selected endmember / source spectrum	Domain
1	Clay minerals	Illite	illite	illite:3-ogs-54-ijs	SWIR
2	Clay minerals	Illite	illite	illite:41	SWIR
3	Clay minerals	Illite	illite	illite:42	SWIR
4	Clay minerals	Illite	illite	illite:63	SWIR
5	Clay minerals	Illite	illite	illite:64	SWIR
6	Clay minerals	Illite	illite	illite:illca1	SWIR
7	Clay minerals	Illite	illite	illite:illeeco1	SWIR
8	Clay minerals	Illite	illite	illite:illeeco2	SWIR
9	Clay minerals	Illite	illite	illite:illchl	SWIR
10	Clay minerals	Illite	illite	illite:illemv1	SWIR
11	Clay minerals	Illite	illite	illite:illcup2	SWIR
12	Clay minerals	Illite	illite	illite:illite-muscov2	SWIR
13	Clay minerals	Illite	illite	illite:illite-muscger1	SWIR
14	Clay minerals	Illite	illite	illite:illite-parag1	SWIR
15	Clay minerals	Illite	illite	illite:illite-pheng	SWIR
16	Clay minerals	Illite	illite	illite:illite-pheng-muscs	SWIR
17	Clay minerals	Illite	illite	illite:illnrv1	SWIR
18	Clay minerals	Illite	illite	illite:illnrv2	SWIR
19	Clay minerals	Illite	illite	illite:illnv1	SWIR
20	Clay minerals	Illite	illite	illite:illnv1e	SWIR
21	Clay minerals	Illite	illite	illite:illor1	SWIR
22	Clay minerals	Illite	illite	illite:illrXnv1	SWIR
23	Clay minerals	Illite	illite	illite:illrcnv1	SWIR
24	Clay minerals	Illite	illite	illite:illshaz1	SWIR
25	Clay minerals	Kaolinite	kaolinite-lo	kaolinite-lo:47	SWIR
26	Clay minerals	Kaolinite	kaolinite-lo	kaolinite-lo:50	SWIR
27	Clay minerals	Kaolinite	kaolinite-lo	kaolinite-lo:51	SWIR
28	Clay minerals	Kaolinite	kaolinite-lo	kaolinite-lo:52	SWIR
29	Clay minerals	Kaolinite	kaolinite-lo	kaolinite-lo:56	SWIR
30	Clay minerals	Kaolinite	kaolinite	kaolinite:43	SWIR
31	Clay minerals	Kaolinite	kaolinite	kaolinite:44	SWIR
32	Clay minerals	Kaolinite	kaolinite	kaolinite:45	SWIR
33	Clay minerals	Kaolinite	kaolinite	kaolinite:46	SWIR
34	Clay minerals	Kaolinite	kaolinite	kaolinite:48	SWIR

No.	Mineral group	Target mineral	Library label	Selected endmember / source spectrum	Domain
35	Clay minerals	Kaolinite	kaolinite	kaolinite:49	SWIR
36	Clay minerals	Kaolinite	kaolinite	kaolinite:57	SWIR
37	Clay minerals	Kaolinite	kaolinite	kaolinite:54	SWIR
38	Clay minerals	Kaolinite	kaolinite	kaolinite:55	SWIR
39	Clay minerals	Kaolinite	kaolinite	kaolinite:58	SWIR
40	Clay minerals	Kaolinite	kaolinite	kaolinite:61	SWIR
41	Clay minerals	Kaolinite	kaolinite	kaolinite:70	SWIR
42	Clay minerals	Kaolinite	kaolinite	kaolinite:71	SWIR
43	Clay minerals	Kaolinite	kaolinite	kaolinite:72	SWIR
44	Clay minerals	Kaolinite	kaolinite	kaolinite:kaolar1	SWIR
45	Clay minerals	Kaolinite	kaolinite	kaolinite:kaolaux1	SWIR
46	Clay minerals	Kaolinite	kaolinite	kaolinite:kaolaux2	SWIR
47	Clay minerals	Kaolinite	kaolinite	kaolinite:kaolca1	SWIR
48	Clay minerals	Kaolinite	kaolinite	kaolinite:kaolic18	SWIR
49	Clay minerals	Kaolinite	kaolinite	kaolinite:kaolic31	SWIR
50	Clay minerals	Kaolinite	kaolinite	kaolinite:kaolic32	SWIR
51	Clay minerals	Kaolinite	kaolinite	kaolinite:kaolic38	SWIR
52	Clay minerals	Kaolinite	kaolinite	kaolinite:kaolic41	SWIR
53	Clay minerals	Kaolinite	kaolinite	kaolinite:kaolic42	SWIR
54	Clay minerals	Kaolinite	kaolinite	kaolinite:kaolic43	SWIR
55	Clay minerals	Kaolinite	kaolinite	kaolinite:kaolic57-lo	SWIR
56	Clay minerals	Kaolinite	kaolinite	kaolinite:kaolic81	SWIR
57	Clay minerals	Kaolinite	kaolinite	kaolinite:kaolcup1	SWIR
58	Clay minerals	Kaolinite	kaolinite	kaolinite:kaolcup2	SWIR
59	Clay minerals	Kaolinite	kaolinite	kaolinite:kaolf1	SWIR
60	Clay minerals	Kaolinite	kaolinite	kaolinite:kaolf2	SWIR
61	Clay minerals	Kaolinite	kaolinite	kaolinite:kaoli100	SWIR
62	Clay minerals	Kaolinite	kaolinite	kaolinite:kaoli108	SWIR
63	Clay minerals	Kaolinite	kaolinite	kaolinite:kaoli109	SWIR
64	Clay minerals	Kaolinite	kaolinite	kaolinite:kaoli113	SWIR
65	Clay minerals	Kaolinite	kaolinite	kaolinite:kaoli114	SWIR
66	Clay minerals	Kaolinite	kaolinite	kaolinite:kaoli115	SWIR
67	Clay minerals	Kaolinite	kaolinite	kaolinite:kaoli116	SWIR
68	Clay minerals	Kaolinite	kaolinite	kaolinite:kaoli121	SWIR
69	Clay minerals	Kaolinite	kaolinite	kaolinite:kaoli144	SWIR
70	Clay minerals	Kaolinite	kaolinite	kaolinite:kaoli152	SWIR
71	Clay minerals	Kaolinite	kaolinite	kaolinite:kaoli157	SWIR
72	Clay minerals	Kaolinite	kaolinite	kaolinite:kaolic38	SWIR
73	Clay minerals	Kaolinite	kaolinite	kaolinite:kaolltev	SWIR
74	Clay minerals	Kaolinite	kaolinite	kaolinite:kaolnm1	SWIR
75	Clay minerals	Kaolinite	kaolinite	kaolinite:kaolnm1	SWIR

No.	Mineral group	Target mineral	Library label	Selected endmember / source spectrum	Domain
76	Clay minerals	Chlorite	chlorite-clinochlore	chlorite-clinochlore:chlorite-	SWIR
77	Clay minerals	Chlorite	chlorite-fe	chlorite-fe:chamosite14	SWIR
78	Clay minerals	Chlorite	chlorite-fe	chlorite-fe:chamosite15	SWIR
79	Clay minerals	Chlorite	chlorite-fe	chlorite-fe:chamosite16	SWIR
80	Clay minerals	Chlorite	chlorite-fe	chlorite-fe:chlorite-fe-chamca	SWIR
81	Clay minerals	Chlorite	chlorite-fe	chlorite-fe:chlorite-fe-chamma	SWIR
82	Clay minerals	Chlorite	chlorite-fe	chlorite-fe:chlorite-fe-chamak	SWIR
83	Clay minerals	Chlorite	chlorite-fe	chlorite-fe:chlorite-fe-chlcan	SWIR
84	Clay minerals	Chlorite	chlorite-fe	chlorite-fe:chlorite-fe-chlmt1	SWIR
85	Clay minerals	Chlorite	chlorite-fe	chlorite-fe:chlorite-fe-chlpal	SWIR
86	Clay minerals	Chlorite	chlorite-fe	chlorite-fe:chlorite-fe-clince	SWIR
87	Clay minerals	Chlorite	chlorite-fe	chlorite-fe:chlorite-fe-clincg	SWIR
88	Clay minerals	Chlorite	chlorite-fe	chlorite-fe:chlorite-fe-ripca1	SWIR
89	Clay minerals	Chlorite	chlorite-fe	chlorite-fe:chlorite-fe-ripca2	SWIR
90	Clay minerals	Chlorite	chlorite-fe	chlorite-fe:chlorite-fe-ripco1	SWIR
91	Clay minerals	Chlorite	chlorite-fe	chlorite-fe:chlorite-fe-sherca	SWIR
92	Clay minerals	Chlorite	chlorite-fe	chlorite-fe:chlorite-fe-sherf	SWIR
93	Clay minerals	Chlorite	chlorite-fe	chlorite-fe:chlorite-fe-val-e0500043	SWIR
94	Clay minerals	Chlorite	chlorite-fe	chlorite-fe:chlorite-fe-sher	SWIR
95	Clay minerals	Chlorite	chlorite-fe	chlorite-fe:chlorite-muscovite	SWIR
96	Clay minerals	Chlorite	chlorite-mg	chlorite-mg:chlorite-mg-chlca2	SWIR
97	Clay minerals	Chlorite	chlorite-mg	chlorite-mg:chlorite-mg-chlms	SWIR
98	Clay minerals	Chlorite	chlorite-mg	chlorite-mg:chlorite-mg-chlne1	SWIR
99	Clay minerals	Chlorite	chlorite-mg	chlorite-mg:chlorite-mg-clinec	SWIR
100	Clay minerals	Chlorite	chlorite-mg	chlorite-mg:chlorite-mg-cliner	SWIR
101	Clay minerals	Chlorite	chlorite-mg	chlorite-mg:chlorite-mg-clinev	SWIR
102	Clay minerals	Chlorite	chlorite-mg	chlorite-mg:chlorite-mg-kamak	SWIR
103	Clay minerals	Chlorite	chlorite-mg	chlorite-mg:chlorite-mg-pennca	SWIR
104	Clay minerals	Chlorite	chlorite	chlorite:chamosite13	SWIR
105	Clay minerals	Chlorite	chlorite	chlorite:chlorite-	SWIR
106	Clay minerals	Chlorite	chlorite	chlorite:chlorite-fe-chlca1	SWIR
107	Clay minerals	Chlorite	chlorite	chlorite:chlorite-mg-chlpa2	SWIR
108	Clay minerals	Chlorite	chlorite	chlorite:chlorite-mg-clines	SWIR
109	Carbonates	Calcite	calcite	calcite:22	SWIR
110	Carbonates	Calcite	calcite	calcite:23	SWIR
111	Carbonates	Calcite	calcite	calcite:3-ogs-54-ijs	SWIR
112	Carbonates	Calcite	calcite	calcite:calcite2	SWIR
113	Carbonates	Calcite	calcite	calcite:calcks1	SWIR
114	Carbonates	Calcite	calcite	calcite:calcrv1	SWIR
115	Carbonates	Calcite	calcite	calcite:calenr1	SWIR
116	Carbonates	Dolomite	dolomite	dolomite:3-ogs-54-ijs	SWIR

No.	Mineral group	Target mineral	Library label	Selected endmember / source spectrum	Domain
117	Carbonates	Dolomite	dolomite	dolomite:44	SWIR
118	Carbonates	Dolomite	dolomite	dolomite:45	SWIR
119	Carbonates	Dolomite	dolomite	dolomite:dolca3	SWIR
120	Carbonates	Dolomite	dolomite	dolomite:doloco1	SWIR
121	Carbonates	Dolomite	dolomite	dolomite:doloco2	SWIR
122	Carbonates	Dolomite	dolomite	dolomite:doloco3	SWIR
123	Carbonates	Dolomite	dolomite	dolomite:doloid1	SWIR
124	Carbonates	Dolomite	dolomite	dolomite:dolom1	SWIR
125	Fe oxides / hydroxides	Goethite	goethite	goethite:344	VNIR
126	Fe oxides / hydroxides	Goethite	goethite	goethite:345	VNIR
127	Fe oxides / hydroxides	Goethite	goethite	goethite:346	VNIR
128	Fe oxides / hydroxides	Goethite	goethite	goethite:347	VNIR
129	Fe oxides / hydroxides	Goethite	goethite	goethite:348	VNIR
130	Fe oxides / hydroxides	Goethite	goethite	goethite:349	VNIR
131	Fe oxides / hydroxides	Goethite	goethite	goethite:350	VNIR
132	Fe oxides / hydroxides	Goethite	goethite	goethite:55	VNIR
133	Fe oxides / hydroxides	Goethite	goethite	goethite:modfosc-fibfo-600026-147_001466500	VNIR
134	Fe oxides / hydroxides	Goethite	goethite	goethite:fbo-fd00025-85.200000	VNIR
135	Fe oxides / hydroxides	Goethite	goethite	goethite:fbo-fd00026-38.400000	VNIR
136	Fe oxides / hydroxides	Goethite	goethite	goethite:fbo-fd00026-90.000000	VNIR
137	Fe oxides / hydroxides	Hematite	hematite	hematite:383	VNIR
138	Fe oxides / hydroxides	Hematite	hematite	hematite:384	VNIR
139	Fe oxides / hydroxides	Hematite	hematite	hematite:385	VNIR
140	Fe oxides / hydroxides	Hematite	hematite	hematite:386	VNIR
141	Fe oxides / hydroxides	Hematite	hematite	hematite:387	VNIR
142	Fe oxides / hydroxides	Hematite	hematite	hematite:388	VNIR
143	Fe oxides / hydroxides	Hematite	hematite	hematite:389	VNIR

No.	Mineral group	Target mineral	Library label	Selected endmember / source spectrum	Domain
144	Fe oxides / hydroxides	Hematite	hematite	hematite:390	VNIR
145	Fe oxides / hydroxides	Hematite	hematite	hematite:393	VNIR
146	Fe oxides / hydroxides	Hematite	hematite	hematite:394	VNIR
147	Fe oxides / hydroxides	Hematite	hematite	hematite:60	VNIR
148	Fe oxides / hydroxides	Hematite	hematite	hematite:highfocxia-fd00043-370_003692500	VNIR
149	Fe oxides / hydroxides	Hematite	hematite	hematite:speccim-ita-fd00043-36918.000000	VNIR
150	Clay minerals	Smectite		montmorillonite:bentnv1	SWIR
151	Clay minerals	Smectite		montmorillonite:65	SWIR
152	Clay minerals	Smectite		montmorillonite:66	SWIR
153	Clay minerals	Smectite		montmorillonite:67	SWIR
154	Clay minerals	Smectite		montmorillonite:68	SWIR
155	Clay minerals	Smectite		montmorillonite:69	SWIR
156	Clay minerals	Smectite		montmorillonite:70	SWIR
157	Clay minerals	Smectite		montmorillonite:71	SWIR
158	Clay minerals	Smectite		montmorillonite:72	SWIR
159	Clay minerals	Smectite		montmorillonite:73	SWIR
160	Clay minerals	Smectite		montmorillonite:74	SWIR
161	Clay minerals	Smectite		montmorillonite:75	SWIR
162	Clay minerals	Smectite		montmorillonite:76	SWIR
163	Clay minerals	Smectite		montmorillonite:77	SWIR
164	Clay minerals	Smectite		montmorillonite:78	SWIR
165	Clay minerals	Smectite		montmorillonite:79	SWIR
166	Clay minerals	Smectite		montmorillonite:80	SWIR
167	Clay minerals	Smectite		montmorillonite:notpurefesmect	SWIR
168	Clay minerals	Smectite		montmorillonite:82	SWIR
169	Clay minerals	Smectite		montmorillonite:83	SWIR
170	Clay minerals	Smectite		montmorillonite:84	SWIR
171	Clay minerals	Smectite		montmorillonite:85	SWIR
172	Clay minerals	Smectite		montmorillonite:86	SWIR
173	Clay minerals	Smectite		montmorillonite:86	SWIR
174	Clay minerals	Smectite		montmorillonite:87	SWIR
175	Clay minerals	Smectite		montmorillonite:87	SWIR
176	Clay minerals	Smectite		montmorillonite:88	SWIR
177	Clay minerals	Smectite		montmorillonite:89	SWIR
178	Clay minerals	Smectite		montmorillonite:90	SWIR
179	Clay minerals	Smectite		montmorillonite:91	SWIR
180	Clay minerals	Smectite		montmorillonite:92	SWIR

No.	Mineral group	Target mineral	Library label	Selected endmember / source spectrum	Domain
181	Clay minerals	Smectite		montmorillonite:93	SWIR
182	Clay minerals	Smectite		montmorillonite:94	SWIR
183	Clay minerals	Smectite		montmorillonite:beidca1	SWIR
184	Clay minerals	Smectite		montmorillonite:beidca2	SWIR
185	Clay minerals	Smectite		montmorillonite:beidcms1	SWIR
186	Clay minerals	Smectite		montmorillonite:beidid1	SWIR
187	Clay minerals	Smectite		montmorillonite:beidid2	SWIR
188	Clay minerals	Smectite		montmorillonite:beidid3	SWIR
189	Clay minerals	Smectite		montmorillonite:beidid4	SWIR
190	Clay minerals	Smectite		montmorillonite:beidid5	SWIR
191	Clay minerals	Smectite		montmorillonite:beidid6	SWIR
192	Clay minerals	Smectite		montmorillonite:beidid7	SWIR
193	Clay minerals	Smectite		montmorillonite:bentca1	SWIR
194	Clay minerals	Smectite		montmorillonite:bentmt1	SWIR
195	Clay minerals	Smectite		montmorillonite:bentmx1	SWIR
196	Clay minerals	Smectite		montmorillonite:bentsd1	SWIR
197	Clay minerals	Smectite		montmorillonite:bentor1	SWIR
198	Clay minerals	Smectite		montmorillonite:64	SWIR
199	Clay minerals	Smectite		montmorillonite:81	SWIR
200	Clay minerals	Smectite		montmorillonite:bentwy1	SWIR
201	Clay minerals	Smectite		montmorillonite:63	SWIR

Table A.1. *Full study-specific spectral library used for MINSPEC unmixing, selected from the USGS Spectral Library Version 7 (Kokaly et al., 2017) and grouped by target mineral. All spectra are drawn from the USGS Spectral Library / asdspelibdata reference collection; the domain column indicates whether the endmember was used in the SWIR clay/carbonate analysis or the VNIR Fe analysis.*

Figure A.1. *Final Mineral Abundance Feature (MAF) configuration file used for spectral unmixing. The file contains the selected wavelength intervals defining the diagnostic absorption features for each mineral included in the MAF approach. The windows were based on established VNIR–SWIR absorption regions and refined through visual inspection of the selected USGS Version 7 reference spectra (Hunt, 1977; van der Meer et al., 2012; Kokaly et al., 2017). They represent workflow-specific configuration intervals rather than unique mineral-identification criteria in isolation.*